Title
Multiscale Constitutive Modeling and Numerical Simulations of the Thermomechanical Response of Polycrystalline NiTi Shape Memory Alloy

Author
Sengupta, Arkaprabha

Publication Date
2010

Peer reviewed|Thesis/dissertation

Multiscale Constitutive Modeling and Numerical Simulations of the Thermomechanical Response of Polycrystalline NiTi Shape Memory Alloy

by

Arkaprabha Sengupta

A dissertation submitted in partial satisfaction of the
requirements for the degree of
Doctor of Philosophy

in

Engineering - Mechanical Engineering

in the

Graduate Division

of the

University of California, Berkeley

Committee in charge:

Professor Panayiotis Papadopoulos, Chair
Professor David Steigmann
Professor Robert L. Taylor

Fall 2010

Multiscale Constitutive Modeling and Numerical Simulations of the Thermomechanical Response of Polycrystalline NiTi Shape Memory Alloy

Abstract

Multiscale Constitutive Modeling and Numerical Simulations of the Thermomechanical Response of Polycrystalline NiTi Shape Memory Alloy

by

Arkaprabha Sengupta

Doctor of Philosophy in Engineering - Mechanical Engineering

University of California, Berkeley

Professor Panayiotis Papadopoulos, Chair

Shape memory alloys have found diverse applications in several engineering systems including biomedical devices and thermal actuators. This is due to their superelastic and shape-memory behavior, which occur as a result of solid-solid transformations from a parent phase to several variants of the product phases. The most commonly used shape-memory alloy is a nearly equiatomic NiTi alloy known as Nitinol. Much research has been devoted to modeling polycrystalline Nitinol under various thermomechanical loading conditions. As a result, several phenomenological and micromechanics-based models have been proposed to characterize the complex behavior of Nitinol in both monocrystalline and textured polycrystalline form.

In this work, a multiscale thermomechanical model for Nitinol is developed that takes into account the temperature-dependent multivariant phase transformations at the single-crystal level and the interaction between various crystals in a textured polycrystalline aggregate. The single-crystal thermomechanical model is relevant to both thermal loading and mechanical loading at high strain-rates. The coupled thermomechanical problem is solved using a monolithic approach in a finite-element framework. Specializing this model to isothermal conditions leads to a temperature-independent mechanical response, which is suitable for quasistatic mechanical loading. Most models in literature account only for isothermal stress-induced phase transformations between the *austenite* and multivariant *martensite* phases in Nitinol. In this work, such a constitutive model is extended to include the formation of intermediate multivariant *rhombohedral* phase as well. In order to model the macroscopic response of polycrystalline Nitinol, first a statistics-based method is developed to determine the optimum size of Representative Volume Element (RVE) meant for solving the microscale problem. The macroscale constitutive response is then derived through computational homogenization of this RVE response. A finite element-on-finite element architecture is employed to solve this multiscale problem accurately. Representative numerical simulations are performed in order to validate the modeling approach with several experiments on thin-walled tubes.

To my parents.

Contents

List of Figures

List of Tables

Acknowledgments

I would like to express my sincere gratitude to Professor Panayiotis Papadopoulos for his invaluable guidance, advice and support during my graduate career at U.C. Berkeley. The discussions I had with him regarding my research, and on computational solid mechanics in general, vastly enhanced my understanding of the subject. His ability to scrutinize every detail of a technical matter not only led to deeper comprehension of the subtle aspects, but also opened up new directions for my research. Further, his emphasis on clarity and conciseness greatly influenced the presentation style of this work.

I am also grateful to Professor Robert L. Taylor for many interesting discussions on computational multiscale modeling and finite element method. It would not have been possible for me to implement the multiscale algorithms in FEAP without his help and guidance. I would also like to thank Professor David Steigmann, for the courses he taught on solid mechanics that updated me on the current state of research in various topics. Further, I am thankful to him and Professor Taylor for reviewing the manuscript and providing many constructive suggestions. I would also like to thank the other faculty members in mechanical engineering with Professor James Casey in particular, for learning so much through the courses they taught and the interactions I had with them.

Acknowledgements are due to Dr. Youngjean Jung and Mr. Arnaud Menjot de Champfleur for the discussions I had with them about their earlier work on Nitinol. I would like to specially thank Dr. Thomas W. Duerig, Dr. Alan Pelton and Dr. Aaron Kueck at Nitinol Devices and Components (NDC) for conducting the experiments on Nitinol tubes and many useful discussions on the behavior of Nitinol. My internship with NDC in summer 2008, under the mentorship of Mr. Craig Bonsignore and Dr. Alan Pelton, was a great learning experience.

My five years at Berkeley would not have been so enjoyable without the friendship and support of many friends. I had a wonderful time with my roommates Debopriyo and Madhur, which included several weekend trips around California. My colleagues Kranthi and Rahul were always there for discussions on various topics related to research or otherwise, over a cup of coffee. I would also like to thank my lab members - Chet, Neil, Jonathan, Nathan, Meriem and John, for their friendship and help.

Finally I acknowledge the support I received from my parents and my sister. Their love and affection were a constant source of encouragement during my graduate life. I dedicate this thesis to my parents, without whose sacrifice, it would not have been possible for me to pursue graduate studies.

Chapter 1

Introduction

Nitinol is a nearly equiatomic Ni-Ti alloy (49.5 at. % Ni, 50.5 at. % Ti) used in several engineering systems, including biomedical devices, such as endovascular stents, angioplasty guidewires, vena-cava filters, etc., see, *e.g.*, [65]. Nitinol is one of the most commonly used shape-memory alloys (SMA). SMAs are materials that exhibit superelastic behavior under mechanical loading at constant temperature and shape-memory behavior under temperature changes at fixed stresses. These two result from reversible, displacive solid-solid phase transformations that are also known as *martensitic transformations*. Among the two effects mentioned above, the superelastic effect is of practical importance, since biomedical devices made of SMAs undergo *in vivo* deformation at fixed temperature. The superelastic effect is illustrated in Figure 1.1, where tension tests have been conducted on thin-tube specimen made of Nitinol under isothermal conditions [60]. It is observed in this figure that when the stresses reach a critical value during loading, Nitinol transforms from its parent *austenite* phase to *martensite* phase. This transformation is accompanied by a transformation strain and a macroscopically observed plateau in the stress-strain response. During unloading, when the stresses reach another critical value, the martensite phase formed during loading starts to transform back to austenite. This causes a reversal of transformation strains until the martensite phase is either partially or completely converted back to austenite depending on the fixed temperature state at which the experiment is performed.

Constitutive theories of superelasticity have evolved from macroscopic phenomenological models suitable for proportional loading of isotropic polycrystals to micromechanics-based models suitable for single-crystal or textured polycrystals under general three-dimensional loading. The latter type of models account for the formation of microstructural regions that are comprised of *twinning* elements and *habit-planes*, which will be explained later. Further, additional effects due to the interaction between the habit-plane variants of martensite and the interaction between individual grains at the polycrystal level can be modeled, if adequate information is available on the morphology of martensite domains and the grain structure along with their orientations. With the help of modern experimental techniques, it has been possible to test specimens with different loading programs and use these tests to validate the

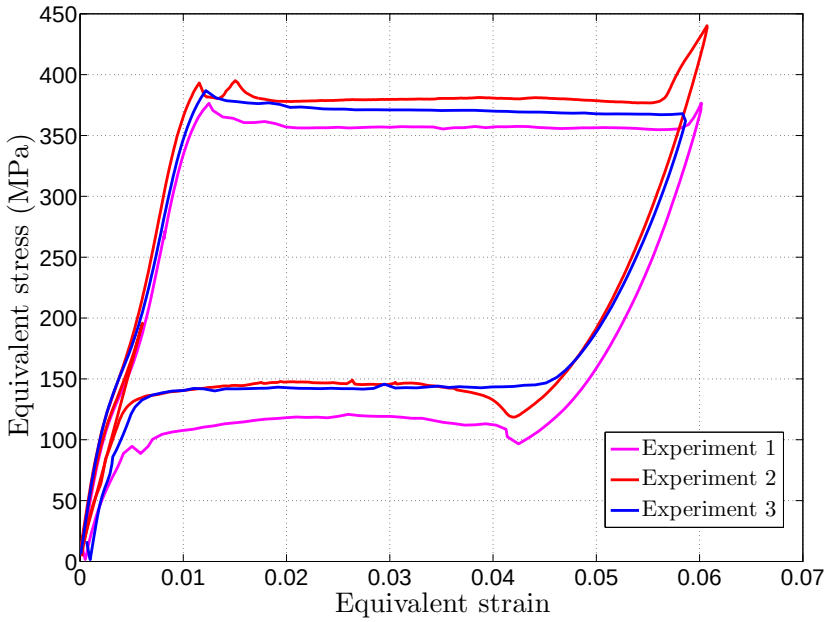

Figure 1.1: *Three cyclic tension tests on Nitinol specimen [60]*

micromechanics-based theories.

1.1 Single-crystal models

Early constitutive models developed for Nitinol single-crystals were phenomenological in nature that were suitable for isotropic polycrystals. In these models, the macroscopic strain due to phase transformation was incorporated as an internal variable and phenomenological laws were proposed for the evolution of this strain based on 1-D experiments done on wire specimens, see [54, 12, 6]. With further understanding of the formation of microstructure from an energy minimization aspect, it gradually became possible to obtain the continuum transformation strains from the deformation of the crystal lattice due to the growth of different variants of martensite, see [7, 9, 10]. Since then, several researchers have focussed on modeling the micromechanics of martensite transformation, and have proposed rate-dependent and rate-independent models for the evolution of transformation strain.

The micromechanics-based models developed over the past few years are vastly different in their areas of focus. Most of these models admit the formation of a set of martensite variants, but differ in the treatment of phase transformation kinetics. While some works propose rate-independent kinetic laws for phase transformation [82, 43], others consider rate-dependent kinetic laws similar to those used in viscoplasiticity theory [35], or based on

statistical mechanics [29], and molecular dynamics computations [2, 36]. See Chapter 8 of [1], for a detailed review on the different models that have been developed for the kinetics of phase transformation. Further, the scope of the models has ranged over infinitesimal, moderate and large deformations. Some of the works that are based on infinitesimal deformations propose an additive decomposition of the total Lagrangian strain into elastic and transformation counterparts [82, 27, 30, 73]. Other works have proposed a constitutive assumption for the transformation strain in the context of finite deformation without explicit use of any kinematic decomposition [29, 43]. On the other hand, recent works have suggested employing a multiplicative decomposition of the total deformation gradient into the elastic and transformational counterparts akin to finite plasticity [3, 91, 85]. In [78], the issues of existence and invariance with respect to the intermediate configuration used in such multiplicative decompositions for phase transformations are investigated. There, it is argued that, unlike plasticity, an intermediate configuration can be locally attained by thermomechanical (as opposed to purely mechanical) unloading and that, similarly to certain treatments of plasticity [57], an isoclinic configuration induced by the austenite lattice may be used to resolve the matter of invariance.

Some of the recent works have also incorporated the full coupling between mechanical and thermal effects [3, 16], which is important in dynamic loading cases. This is effected by modifying the free energy typically proposed for isothermal conditions, to include terms dependent on the temperature deviations from the reference state. The solution of boundary-value problems in this case requires simultaneous satisfaction of both the momentum and the energy equations. The strong thermomechanical coupling complicates the development of finite element algorithms for such problems.

The single-crystal models discussed in this dissertation have two separate areas of emphasis. The first is on extending the model developed in [43] to include the formation of an intermediate rhombohedral phase (R-phase) and its effects on the subsequent martensitic transformation. The presence of R-phase renders the transformation process history-dependent, a fact which needs to be taken into account while formulating the transformation conditions. The other area of emphasis is on developing a new thermomechanical model based on the multiplicative kinematic decomposition discussed above, and comparing it with a related model obtained by extending the isothermal model in [43]. Adequate validation with experiments has been done for all the models discussed in this dissertation.

1.2 Polycrystal models

In superelastic polycrystals, the interaction between the different grains may greatly affect the phase transformation of the material, see, *e.g.*, [81]. In particular, the transformation properties of superelastic polycrystals are very sensitive to the (generally non-uniform) distribution of individual crystal orientations, *i.e.*, to texture. Evidence of the effects of texture has been cited by Gall *et al.* [25], who attributed to it, the asymmetric behavior of Nitinol

in tension and compression.

Numerical modeling of SMA polycrystals taking into account the crystallographic orientations and the resulting crystal interactions has been pursued by several researchers, see, *e.g.* [41, 89, 50]. Typically, a set of Euler angles is allocated to the crystals of an aggregate either from a random distribution or based on the texture data obtained through X-ray diffractometry. Subsequently, the overall response of the polycrystal is determined by way of a homogenization technique. Specifically, a Taylor averaging scheme is used in [89] within a multiscale finite element setting, while [41, 50] employ a self-consistent approach. Although the self-consistent approach is capable of modeling intergranular interactions with accuracy, it requires precise knowledge of the microstructure in terms not only of the crystallographic distribution densities, but also of the shape of the individual grains. Notwithstanding this issue, a comprehensive procedure for determining the representative volume element (RVE) size in polycrystal models appears to be lacking. Furthermore, no direct comparison has been presented of the relative merits and demerits of different homogenization procedures applied to polycrystalline superelasticity.

The multiscale model discussed in this dissertation is developed in two phases. Initially a statistical method is developed for the selection of an RVE, such that its effective response canonically represents the local macroscopic behavior of the textured polycrystalline material. The effective response is obtained for quasistatic loading of Nitinol specimen so that the model developed in [43] could be used at single-crystal (fine-scale) level. The local coarse-scale response is determined by applying three homogenization techniques based on the Taylor assumption, displacement boundary condition and periodic boundary condition. The multiscale model is implemented in a two-scale finite element framework following recent work by Kouznetsova [47]. The proposed finite element implementation of this model is ideally suited for parallelization. A simple illustration of such parallelization is outlined in this work, whereby the coarse and fine-scale problems are assigned to separate processors which communicate with each other using classical message-passing protocols (*e.g.*, MPI). The second phase focusses on developing a multiscale thermomechanical model for phase transforming polycrystals. The strong thermomechanical coupling and the requirement to satisfy energy equation in addition to the momentum equation present several challenges to solving initial/boundary-value problems in both scales. Not only thermal quantities like heat flux, specific heat capacity and dissipative heat generated need to be homogenized in addition to the mechanical stress, but also all homogenized coupling tangents other than the effective elastic moduli and thermal conductivity need to be computed in order to solve the problem using a monolithic approach.

1.3 Summary of present work

This dissertation proposes constitutive models, that capture various aspects of phase transformation in Nitinol monocrystals and polycrystals, and pertain to physical phenom-

ena at both microscopic and macroscopic scales. The organization of this dissertation is as follows: the basic elements of continuum mechanics are introduced in Chapter 2. The physics of martensite phase transformation is explained in Chapter 3. In particular, the crystallography of rhombohedral and martensite phases that occur in Nitinol are elaborated therein. Also, the effect of texture on phase transformation is described. A new thermomechanical model for Nitinol single-crystal is introduced in Chapter 4 and compared with existing models. Algorithms for the solution of the transformation equations for these models are also presented in this chapter. In Chapter 5, a constitutive model is developed that explicitly accounts for R-phase formation in single-crystal. Chapter 6 discusses the development of finite element algorithms for the aforementioned models. Subsequently in Chapter 7, the various multiscale approaches used to obtain the polycrystal behavior through homogenization of constituent single-crystal responses are introduced in a finite element setting. In Chapter 8, numerical examples which illustrate the defining features of the discussed models are provided. The larger simulations are based on experimental results, where the model parameters are selected from the literature and from experimental work conducted earlier in this research program. Finally Chapter 9 provides concluding remarks on the models developed and their performance vis-a-vis the experiments, and outlines future scope of this work. Some supplementary material are presented in the appendices. Specifically, Appendix A includes derivations pertaining to solving the transformation equations subject to some constraints, while Appendix B contains a derivation of the rotation matrix used to model texture.

Chapter 2

Theoretical background

2.1 Continuum mechanics

2.1.1 Kinematics

In continuum mechanics, a body $\mathcal{B}$ is assumed to be a collection of material points. At any instant of time, assume that $\mathcal{B}$ occupies a bounded region $\mathcal{R}$ in three-dimensional Euclidean space $\mathbb{R}^3$. The mapping from $\mathcal{B}$ to the region $\mathcal{R}$ at time t, given by $\boldsymbol{\chi} : \mathcal{B} \times t \rightarrow \mathcal{R} \subset \mathbb{R}^3$, is known as the *configuration mapping*. The position vector of any material point, X at time t, with respect to a fixed origin is given by $\mathbf{x} = \boldsymbol{\chi}(X, t)$, and is referred to as the current position of X. The image $\mathcal{R}$ of $\mathcal{B}$ under the mapping $\boldsymbol{\chi}$ is referred to as the *current configuration* of the body. For convenience, the mapping $\boldsymbol{\chi}$ at some fixed time t_0, denoted by $\boldsymbol{\chi}\big|_{t_0} = \boldsymbol{\kappa} : \mathcal{B} \rightarrow \mathcal{R}_\kappa \subset \mathbb{R}^3$, is used to define a *reference configuration* $\mathcal{R}_\kappa$ of the body. The position vector of X in the reference configuration is given by $\mathbf{X} = \boldsymbol{\kappa}(X)$. Assuming that the mapping $\boldsymbol{\kappa}$ is invertible for any fixed time, the relation between the reference and current configurations is described by the deformation function $\boldsymbol{\chi}_\kappa : \mathcal{R}_\kappa \times t \rightarrow \mathcal{R}$, so that $\mathbf{x} = \boldsymbol{\chi}(\boldsymbol{\kappa}^{-1}(\mathbf{X}), t) = \boldsymbol{\chi}_\kappa(\mathbf{X}, t)$. The displacement of X at t relative to its position at time t_0 is given by

$$\mathbf{u} = \mathbf{x} - \mathbf{X} \ . \tag{2.1}$$

A fundamental measure of deformation is the deformation gradient which is defined at each material point X by $\mathbf{F} = \mathrm{Grad}\, \boldsymbol{\chi}_\kappa$, assuming the required differentiability of $\boldsymbol{\chi}_\kappa$. Here, "Grad" denotes the referential gradient operator. Physically, $\mathbf{F}$ maps an infinitesimal line element $d\mathbf{X}$ at $\mathbf{X}$ in the reference configuration linearly to an infinitesimal line element $d\mathbf{x}$ at $\mathbf{x}$ in the current configuration, *i.e.* $d\mathbf{x} = \mathbf{F}\ d\mathbf{X}$. The deformation gradient is assumed to be invertible at any time t. Furthermore it is assumed that $J = \mathrm{det}\mathbf{F} > 0$ at all times.

The right Cauchy-Green deformation tensor $\mathbf{C}$ is defined as

$$\mathbf{C} = \mathbf{F}^T\mathbf{F} \ , \tag{2.2}$$

and the Lagrangian strain tensor is defined as

$$\mathbf{E} = \frac{1}{2}(\mathbf{C} - \mathbf{I}) \ , \tag{2.3}$$

where $\mathbf{I}$ is the second-rank referential identity tensor. Since the deformation gradient $\mathbf{F}$ satisfies $\det\mathbf{F} > 0$, it is uniquely decomposed as

$$\mathbf{F} = \mathbf{RU} \ = \mathbf{VR}, \tag{2.4}$$

where $\mathbf{U}$, $\mathbf{V}$ are symmetric positive-definite tensors and $\mathbf{R}$ is a proper orthogonal tensor, namely $\mathbf{RR}^T = \mathbf{R}^T\mathbf{R} = \mathbf{I}$ and $\det\mathbf{R} = \mathbf{I}$.

2.1.2 Deformation of inelastic materials

By way of background, materials undergoing simultaneous elastic and inelastic deformations are discussed here in the context of finite deformations. In order to obtain a measure of these two parts of deformation, it is necessary to isolate the two parts by constructing a fictitious *intermediate configuration* between the reference and current configurations. The order of applying the elastic and inelastic deformations starting from the reference configuration governs the nature of the intermediate configuration. Therefore, to develop constitutive theories dependent on an intermediate configuration, it is necessary to prescribe the precise nature of this configuration. Typically, if the inelastic deformation is due to plasticity or displacive phase transformation, the intermediate configuration can be conceptually arrived at by releasing the elastic deformation at a given point in the current configuration. Hence, the intermediate configuration is assumed to be obtained through purely inelastic deformation of the body from the reference configuration. However, it should be noted that although an intermediate configuration may not exist globally, a local configuration may be arrived at by unloading infinitesimal neighborhoods of every point in the body to a state free of any elastic deformation, see [56, 48, 15]. The total deformation gradient can then be multiplicatively decomposed into elastic and inelastic counterparts $\mathbf{F}^e$ and $\mathbf{F}^i$, respectively, such that

$$\mathbf{F} \ = \ \mathbf{F}^e\mathbf{F}^i \ , \tag{2.5}$$

where both $\det\mathbf{F}^e > 0$ and $\det\mathbf{F}^i > 0$.

However additional invariance requirements are required to be met for such decomposition, so that arbitrary rotations superimposed on the intermediate configuration do not influence the state of a body undergoing inelastic deformation, see [32] for related discussion in the context of plasticity. As a result, constitutive theories have to depend on total Green-Lagrange strain $\mathbf{E}$ and inelastic Green-Lagrange strain $\mathbf{E}^i$, where $\mathbf{E}^i = \frac{1}{2}({\mathbf{F}^i}^T\mathbf{F}^i - \mathbf{I})$. This forms the basis of a constitutive model for phase transformation discussed later in Chapter 4.

Although invariance requirements dictate that constitutive theories be dependent on total and inelastic strains as discussed above, some theories have instead been developed in terms of the elastic strain $\mathbf{E}^e$, defined through the multiplicative decomposition (2.5) as,

$$\mathbf{E}^e = \frac{1}{2}[\mathbf{F}^{i-T}\mathbf{C}\mathbf{F}^{i-1} - \mathbf{I}] \ , \tag{2.6}$$

see [4] for such a theory in elastic-plastic materials. This formulation is valid in the context of plasticity and phase transformation in single-crystals or textured polycrystals. The invariance requirement in such cases is met by expressing the kinematics of inelastic deformation in the intermediate configuration with respect to a "director frame" attached to the crystal lattice and, therefore, subjected to the same rotation as the configuration itself, see [57]. Hence $\mathbf{F}^i$ is taken to act on material line elements aligned with this director frame. The details for the construction of such a multiplicative decomposition for displacive phase transformation are discussed in Section 3.4. A thermomechanically coupled model that employs this kinematical description is developed in Chapter 4.

2.1.3 Balance laws

In this section, "Div" and "div" will be used to denote the divergence operator with respect to referential and spatial coordinates, respectively. The mass contained in an arbitrary material region $\mathcal{P} \in \mathcal{R}$ is defined as

$$\mathcal{M}(\mathcal{P}) = \int_{\mathcal{P}} \rho \ dv \ , \tag{2.7}$$

where $\rho = \rho(\mathbf{x}, t)$ is the current mass density. The conservation of mass is then expressed as

$$\frac{d}{dt}\int_{\mathcal{P}} \rho \ dv = 0 \ . \tag{2.8}$$

The Reynolds' transport theorem is stated as

$$\frac{d}{dt}\int_{\mathcal{P}} \rho \ dv = \int_{\mathcal{P}} (\dot{\rho} + \rho \mathrm{div}\mathbf{v}) \ dv \ , \tag{2.9}$$

where superposed "dot" denotes material time derivative and $\mathbf{v} = \dot{\mathbf{x}}$ is the velocity field. Subsequently through the localization theorem, the local form of mass balance (2.8) is expressed as,

$$\dot{\rho} + \rho \ \mathrm{div}\mathbf{v} = 0 \ . \tag{2.10}$$

A referential statement of mass conservation can be obtained by noting that for an arbitrary material region in reference configuration $\mathcal{P}_\kappa \in \mathcal{R}_\kappa$, (2.8) implies

$$\int_{\mathcal{P}_\kappa} \rho_0 \ dV = \int_{\mathcal{P}} \rho \ dv \ , \tag{2.11}$$

where ρ_0 is the mass density per unit referential volume. Using $dv = JdV$ in (2.11), and subsequently localization theorem gives,

$$\rho_0 = \rho J \ . \tag{2.12}$$

The linear momentum balance in the current configuration for $\mathcal{P}$ with piecewise smooth boundary $\partial\mathcal{P}$ is given by

$$\frac{d}{dt}\int_{\mathcal{P}} \rho\mathbf{v}\ dv = \int_{\mathcal{P}} \rho\mathbf{b}\ dv + \int_{\partial\mathcal{P}} \mathbf{t}\ da\ , \tag{2.13}$$

where $\mathbf{b}$ is the body force per unit mass, and $\mathbf{t}$ is the traction vector per unit area on the orientable surface ∂P. Now, Cauchy's theorem states that the traction $\mathbf{t}$ is a linear function of the unit normal $\mathbf{n}$ to ∂P and can be expressed as $\mathbf{t} = \mathbf{T}\mathbf{n}$, where $\mathbf{T}$ is the second-order Cauchy stress tensor. Subsequently, applying the divergence theorem and localization theorem the local form of linear momentum balance (2.13) is given as

$$\mathrm{div}\mathbf{T} + \rho\mathbf{b} = \ \rho\mathbf{a}\ , \tag{2.14}$$

where $\mathbf{a} = \dot{\mathbf{v}}$ is the acceleration field. A referential form of the above equation is given as

$$\mathrm{Div}\,\mathbf{P}\ +\ \rho_0\mathbf{b}\ =\ \rho_0\mathbf{a}\ , \tag{2.15}$$

where

$$\mathbf{P} = J\mathbf{T}\mathbf{F}^{-T} \tag{2.16}$$

is the first Piola-Kirchhoff stress tensor.

In a similar manner, balance of angular momentum is first given in integral form as

$$\frac{d}{dt}\int_{\mathcal{P}} \mathbf{x}\times\rho\mathbf{v}\ dv = \int_{\mathcal{P}} \mathbf{x}\times\rho\mathbf{b}\ dv + \int_{\mathcal{P}} \mathbf{x}\times\mathbf{t}\ da\ . \tag{2.17}$$

Using mass conservation (2.8) and linear momentum balance (2.14), the local form of above equation reduces to a statement of symmetry for the stress tensor $\mathbf{T}$, *i.e.*,

$$\mathbf{T} = \mathbf{T}^T\ , \tag{2.18}$$

and using (2.16), provides the following identity in terms of referential quantities,

$$\mathbf{P}\mathbf{F}^T = \mathbf{F}\mathbf{P}^T\ . \tag{2.19}$$

The balance of mechanical energy in the current configuration is stated as

$$\frac{d}{dt}\int_{\mathcal{P}} (\frac{1}{2}\rho\mathbf{v}\cdot\mathbf{v} + \mathbf{T}\cdot\mathbf{D})\ dv = \int_{\mathcal{P}} \rho\mathbf{b}\cdot\mathbf{v}\ dv + \int_{\mathcal{P}} \mathbf{t}\cdot\mathbf{v}\ da\ , \tag{2.20}$$

and is a direct consequence of (2.12), (2.14) and (2.18).

In the presence of heat exchange with the environment, an energy balance is postulated as

$$\frac{d}{dt}\int_{\mathcal{P}} \rho(\epsilon + \frac{1}{2}\mathbf{v}\cdot\mathbf{v})\ dv = \int_{\mathcal{P}} \rho(\mathbf{b}\cdot\mathbf{v} + r)\ dv + \int_{\mathcal{P}} (\mathbf{t}\cdot\mathbf{v} - h)\ da\ . \tag{2.21}$$

In the above, ϵ is the internal energy per unit mass which includes all forms of energy except kinetic energy. Also, h is the outward heat flux per unit area across $\partial\mathcal{P}$ and r is the heat supply per unit mass. A heat flux vector $\mathbf{q}$ can be constructed by the relation $h = \mathbf{q}\cdot\mathbf{n}$ in a way similar to Cauchy's theorem for the stress tensor. Then, the local spatial and referential form of the above equation are derived as

$$\rho\dot{\epsilon} \ = \ \rho r - \mathrm{div}\mathbf{q} + \mathbf{T}\cdot\mathbf{D}\ , \tag{2.22}$$

and

$$\rho_0\dot{\epsilon} \ = \ \rho_0 r - \mathrm{Div}\mathbf{q}_0 + \mathbf{S}\cdot\dot{\mathbf{E}} \tag{2.23}$$

respectively, where $q_0 = \frac{1}{J}\mathbf{F}\mathbf{q}$ is the heat flux in reference configuration, and $\mathbf{S} = \mathbf{F}^{-1}\mathbf{P}$ is the symmetric second Piola-Kirchhoff stress. The energy balance is also referred to as the First Law of Thermodynamics.

2.2 Second Law of Thermodynamics

For any type of material whose constitutive description contains internal variables (denoted here by $\mathcal{W}$), first an entropy function may be constructed by a procedure proposed by Rivlin, [75, 14]. The body is assumed to be able to undergo a process that is *homothermal*, defined as one in which the temperature gradient is kept at zero. Further, during this process the internal variables are kept fixed. Then, the energy equation (2.23) reduces to

$$\rho_0\dot{\epsilon} \ = \ \rho_0 r + \mathbf{S}\cdot\dot{\mathbf{E}}\ , \tag{2.24}$$

since the heat flux term vanishes under homothermal conditions. In this case, the Second Law of Thermodynamics asserts path-independence of the Clausius integral

$$\int_{t_0}^{t} \frac{r}{\theta}\ d\tau = \int_{t_0}^{t} \frac{1}{\theta}\left\{\dot{\epsilon} - \frac{\mathbf{S}\cdot\dot{\mathbf{E}}}{\rho_0}\right\}\ d\tau\ , \tag{2.25}$$

where θ is the absolute temperature. This allows for the definition of a family of specific entropy functions parameterized by $\mathcal{W}$ as $\eta = \hat{\eta}(\mathbf{E}, \theta, \mathcal{W})$, whose evolution is given by

$$\dot{\eta} = \frac{r}{\theta} = \frac{1}{\theta}\left\{\dot{\epsilon} - \frac{\mathbf{S}\cdot\dot{\mathbf{E}}}{\rho_0}\right\}\ . \tag{2.26}$$

Moreover, a Helmholtz free energy can be introduced as

$$\psi = \hat{\psi}(\mathbf{E}, \theta, \mathcal{W}) = \rho_0(\epsilon - \eta\theta) \ . \tag{2.27}$$

Taking the material time derivative of the above equation and using it in (2.26) leads to

$$\dot{\psi} = \mathbf{S} \cdot \dot{\mathbf{E}} - \rho_0 \eta \dot{\theta} \ . \tag{2.28}$$

Hence during a homothermal process with fixed internal variables, $(2.27)_1$ and (2.28) implies

$$\left(\frac{\partial \hat{\psi}}{\partial \theta} + \rho_0 \eta \right) \dot{\theta} + \left(\frac{\partial \hat{\psi}}{\partial \theta} - \mathbf{S} \right) \cdot \dot{\mathbf{E}} = 0 \ . \tag{2.29}$$

Since the above holds for all values of $\dot{\theta}$ and $\dot{\mathbf{E}}$ and their coefficients are independent of rates, the Gibbs relations can be derived as [14]

$$\begin{aligned} \rho_0 \eta = \rho_0 \hat{\eta}(\mathbf{E}, \theta, \mathcal{W}) = \ - \frac{\partial \hat{\psi}}{\partial \theta}(\mathbf{E}, \theta, \mathcal{W}) \ , \\ \mathbf{S} = \hat{\mathbf{S}}(\mathbf{E}, \theta, \mathcal{W}) = \frac{\partial \hat{\psi}}{\partial \mathbf{E}}(\mathbf{E}, \theta, \mathcal{W}) \ . \end{aligned} \tag{2.30}$$

Now it can be argued that the Gibbs relations (2.30) hold even when a temperature gradient is present (since they do not depend on it), and a change in $\mathcal{W}$ occurs (since they are independent of rate of $\mathcal{W}$ as well). In this case, the specific form of the energy equation in terms of rate of entropy can be constructed, as will be done later in the context of phase transforming materials. Now, given the above form of entropy, the Second Law of Thermodynamics in the form of Clausius-Duhem inequality can be postulated. This is given in integral form as

$$\frac{d}{dt} \int_{\mathcal{P}} \rho \eta \ dv \geq \int_{\mathcal{P}} \rho \frac{r}{\theta} \ dv - \int_{\mathcal{P}} \frac{h}{\theta} \ da \ . \tag{2.31}$$

By substituting $h = \mathbf{q} \cdot \mathbf{n}$ in above inequality, a local spatial form is derived as

$$\rho \dot{\eta} \theta \ \geq \ \rho r - \operatorname{div} \mathbf{q} + \frac{\mathbf{q} \cdot \operatorname{grad} \theta}{\theta} \ , \tag{2.32}$$

where "grad" is the spatial gradient operator. The local referential counterpart of (2.32) can be expressed as

$$\rho_0 \dot{\eta} \theta \ \geq \ \rho_0 r - \operatorname{Div} \mathbf{q}_0 + \frac{\mathbf{q}_0 \cdot \operatorname{Grad} \theta}{\theta} \ . \tag{2.33}$$

Chapter 3

Phase transformation in Nitinol polycrystals

In the present chapter, the micromechanics of martensitic transformation in a single crystal is elucidated. Further, the quantitative details related to this transformation are discussed specifically for Nitinol.

3.1 Martensitic transformation

Martensitic transformation is the process of conversion of an "ordered" phase of a crystalline solid to a "less-ordered" phase of the same in a displacive manner. This involves transition from the originally well-structured crystal lattice having a higher order of crystal symmetry, known as the "parent" phase, to one with a lesser order of crystal symmetry, called the "product" phase. In the case of martensitic phase transformation, the parent phase is generally referred to as *austenite* and the product phase as *martensite*. In a displacive phase transformation, the atoms move in a systematic coordinated manner with the resulting displacement being a fraction of one lattice spacing, see [13, Chapter 8].

3.2 Crystal lattice

A crystal lattice is usually described as a *Bravais lattice* which is an infinite set of points corresponding to atomic locations. The coordinates of atoms are generated by translation along the three linearly independent lattice basis vectors as

$$\mathbf{x} = n_i \, \mathbf{e}_i = n_1 \, \mathbf{e}_1 + n_2 \, \mathbf{e}_2 + n_3 \, \mathbf{e}_3 \ , \quad n_i \in \mathbb{Z} \ , \tag{3.1}$$

where $\mathbf{e}_i$, $i = 1, 2, 3$, are the lattice basis vectors and $\mathbb{Z}$ is the set of integers. The position vector of any atom can then be expressed as a triplet of integers $[n_1 \ n_2 \ n_3]$. However, in

practice, the integers n_i are taken to have positive values, and whenever necessary, $\bar{n}_i$ is used instead to denote negative values of n_i.

3.2.1 Deformation of lattices

A second-rank tensor is usually employed to describe the deformation from one set of lattice vectors to another. In the case of martensitic transformation, if $\bar{\mathbf{F}}$ is the tensor that transforms the austenite lattice represented by the basis vectors $\{\mathbf{e}_i^a\}$ to the martensite represented by $\{\mathbf{e}_i^m\}$, then one has, $\mathbf{e}_i^m = \bar{\mathbf{F}}\mathbf{e}_i^a$. Here, $\det\bar{\mathbf{F}} > 0$ is chosen to preserve the orientation of the basis vectors. The link between the lattice deformation and the continuum deformation is provided by the Cauchy-Born hypothesis [20]. This states that "Applying the macroscopic deformation gradient as a linear transformation to a reference set of lattice vectors gives a possible set of lattice vectors in the deformed crystal", see [21]. Hence, for a continuum local deformation gradient $\bar{\mathbf{F}}$, an underlying lattice in the undeformed configuration given by $\{\mathbf{e}_i^0\}$, is deformed to $\{\mathbf{e}_i\}$, according to the rule

$$\mathbf{e}_i = \bar{\mathbf{F}}\ \mathbf{e}_i^0\ , \quad i = 1, 2, 3\ . \tag{3.2}$$

The rule can also be employed in the reverse direction where the continuum deformation gradient is computed from the lattice deformation. This allows the definition of strain due to phase transformation at continuum level, knowing the transformation from one lattice structure to another.

The stored energy associated with a thermoelastic crystalline solid at constant temperature, can be expressed as a function of the deformation gradient in the form $\phi(\bar{\mathbf{F}})$. Since the stored energy is invariant under superposed rigid body rotations represented by a tensor $\mathbf{Q}$, the following relation holds:

$$\phi(\mathbf{Q}\bar{\mathbf{F}}) = \phi(\bar{\mathbf{F}})\ . \tag{3.3}$$

3.2.2 Lattice symmetry

Certain transformations map a crystal lattice, in some chosen reference configuration, back to itself. These transformations could be rigid-body rotations, reflections or shear and form a group called the *symmetry group* of the lattice, see [10, Section 3.2]. Thus, if a transformation, $\bar{\mathbf{T}}$, lies in the symmetry group of the lattice, its stored energy with respect to the reference configuration, should satisfy the following relation for any deformation $\mathbf{F}$:

$$\phi(\bar{\mathbf{F}}\bar{\mathbf{T}}) = \phi(\bar{\mathbf{F}})\ . \tag{3.4}$$

However, we exclude the shear transformations in symmetry group, when considering martensitic phase transformations, since they are associated with slip of the lattice. Further, reflections are not associated with any physical deformation of the lattice. The subset of the

symmetry group comprising rotations, is called the *Laue group*($\mathcal{L}$) of the lattice. As a result of (3.3) and (3.4) the following identity holds:

$$\phi(\bar{\mathbf{Q}}^T\bar{\mathbf{F}}\bar{\mathbf{Q}}) = \phi(\bar{\mathbf{F}}) \ , \qquad \bar{\mathbf{Q}} \in \mathcal{L} \ . \tag{3.5}$$

3.3 Crystallography of martensitic phase transformation

In phase transformation, a unit cell of the product lattice is generated by a distortion of a suitably oriented unit cell of the parent lattice. This relation between the original unit cell and the oriented unit cell of the parent lattice that transforms to the unit cell of the product lattice is called a *lattice correspondence*. In the case of Nitinol where transformation takes place from B2 (cubic) austenite phase to B19′ (monoclinic) martensite phase, this correspondence can be expressed as

$$[100]_{B19'} \rightarrow [100]_{B2} \ , \quad [010]_{B19'} \rightarrow [011]_{B2} \ , \quad [001]_{B19'} \rightarrow [0\bar{1}1]_{B2} \ , \tag{3.6}$$

as shown in Figure 3.1, where the lattice vectors of the austenite unit cell given by $\hat{\mathbf{I}}_i$, $i = 1, 2, 3$, transform to those of the oriented unit cell $\hat{\mathbf{I}}'_i$, $i = 1, 2, 3$ [33]. The subsequent deformation to the martensite lattice is given by a stretch along all three unit vectors and a simple shear on the plane with normal $\hat{\mathbf{I}}'_2$, along the $\hat{\mathbf{I}}'_1$ vector. Note that although $\hat{\mathbf{I}}_i$ are the basis vectors defined earlier as $\mathbf{e}^a_i$, $\hat{\mathbf{I}}'_i$ are the basis vectors of the oriented unit cell before phase transformation, hence are not identical to the basis vectors, $\mathbf{e}^m_i$, of the martensite unit cell. Thus, there is a necessity to use a different set of basis vectors for lattice correspondence and phase transformation. The original lattice is shown in dashed lines while the deformed one is shown in solid lines in Figure 3.1, see [33] for details.

3.3.1 Lattice correspondence variants

The distortion associated with phase transformation usually results in lowering of the number of symmetry-based rotations of the product lattice. In particular, for displacive phase transformations, the product phase is obtained by a slight distortion of the parent phase, resulting in the Laue group of the product phase being a subset of that of parent phase. The lattice vector of the product phase in this case, is said to be in the *Ericksen-Pitteri neighborhood* of that of the parent phase, see [10, Chapter 3]. Let the Laue groups of the parent (austenite) and product (martensite) phases be denoted by $\mathcal{L}^a$ and $\mathcal{L}^m$, respectively. Now the distortion from a unit cell of parent to that of product phase is given by a deformation gradient $\bar{\mathbf{F}}$, which after polar decomposition (2.4), can be expressed through the the stretch tensor $\bar{\mathbf{U}}$. This symmetric positive-definite second-rank tensor is called the *Bain strain* or *transformation stretch*. Now, if one such stretch tensor $\bar{\mathbf{U}}_1$ is derived, one can

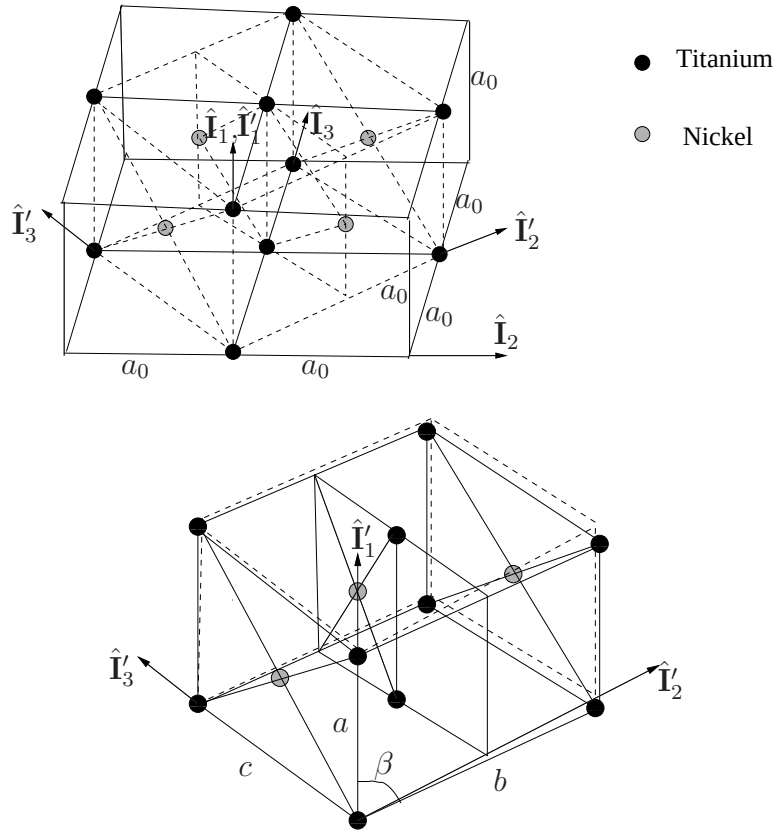

Figure 3.1: *Crystallography for B2-B19′ transformation*

derive $\mathcal{N}(\mathcal{L}^a)$ of such symmetry-related stretch tensors by applying the transformation

$$\bar{\mathbf{U}}' = \bar{\mathbf{Q}}^T \bar{\mathbf{U}}_1 \bar{\mathbf{Q}} \ , \qquad \bar{\mathbf{Q}} \in \mathcal{L}^a \ . \tag{3.7}$$

By (3.5), all these transformations are associated with the same energy, hence the stretches associated with these symmetry-related transformations are said to correspond to the different *energy wells* of the product phase. Since $\mathcal{L}^m \subset \mathcal{L}^a$, not all of the stretches generated through (3.7) produce distinct lattice structures or variants of the martensite phase. The distinct lattice structures generated through (3.7) are called the *lattice correspondence variants* (LCVs) associated with the martensite phase transformation. The number of such variants is given by

$$\mathcal{N}_{lcv} = \frac{\mathcal{N}(\mathcal{L}^a)}{\mathcal{N}(\mathcal{L}^m)} \ , \tag{3.8}$$

where $\mathcal{N}(\mathcal{L}^m)$ is the number of rotations in $\mathcal{L}^m$. See [10, Chapter 3] for related explanation. Nitinol undergoes a B2-B19′ transformation, for which $\mathcal{N}(\mathcal{L}^a) = 24$ and $\mathcal{N}(\mathcal{L}^m) = 2$, hence the number of lattice correspondence variants is $\mathcal{N}_{lcv} = 12$.

3.3.2 Habit-plane variants

Frequently during phase transformation, the lattice correspondence variants of martensite phase form twins and a compatible interface is generated between twinned martensite and austenite to minimize energy. A procedure for obtaining this austenite-twinned martensite microstructure was originally derived in [7] for general crystal structures. The plane between undeformed austenite and twinned martensite that remains undeformed under phase transformation is called a *habit-plane*, and all possible habit-plane solutions that minimize the strain energy are called *habit-plane variants*.

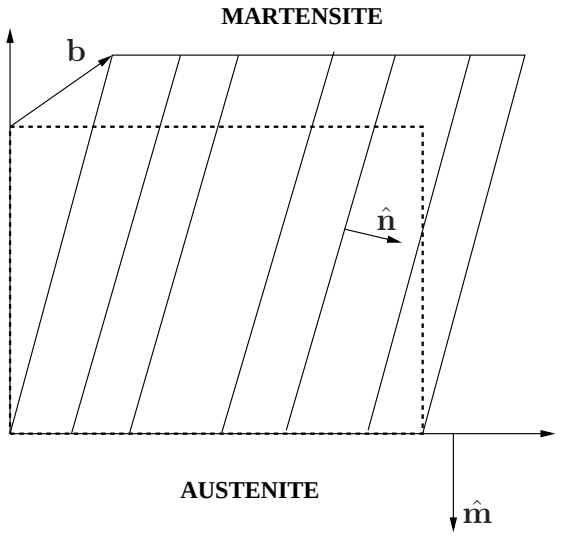

Figure 3.2: *Habit-plane formation for austenite-martensite transformation*

A procedure for obtaining the habit-plane solutions for the cubic-monoclinic (B2-B19′) phase transformation has been provided in [33, 34]. First, the stretches associated with the 12 lattice correspondence variants are obtained. Then, the twinning equation (a special form of the well-known Hadamard compatibility equation) is solved for every lattice correspondence variant (LCV) pair $(i : j)$. This equation takes the form

$$\mathbf{R}_{ij}\mathbf{U}_i - \mathbf{U}_j \;=\; \mathbf{a} \otimes \hat{\mathbf{n}} \;, \tag{3.9}$$

#	$\hat{\mathbf{m}}$			$\mathbf{b}$			#	$\hat{\mathbf{m}}$			$\mathbf{b}$		
1	m_1	$-m_3$	m_2	b_1	$-b_3$	b_2	13	$-m_2$	$-m_1$	$-m_3$	$-b_2$	$-b_1$	$-b_3$
2	$-m_3$	m_1	$-m_2$	$-b_3$	b_1	$-b_2$	14	$-m_2$	m_1	m_3	$-b_2$	b_1	b_3
3	$-m_1$	m_3	m_2	$-b_1$	b_3	b_2	15	m_2	m_3	m_1	b_2	b_3	b_1
4	m_3	$-m_1$	$-m_2$	b_3	$-b_1$	$-b_2$	16	m_2	$-m_3$	$-m_1$	b_2	$-b_2$	b_3
5	m_1	m_3	$-m_2$	b_1	b_3	$-b_2$	17	$-m_1$	$-m_2$	m_3	$-b_1$	$-b_2$	b_3
6	m_3	m_1	m_2	b_3	b_1	b_2	18	m_1	$-m_2$	$-m_3$	b_1	$-b_2$	$-b_3$
7	$-m_1$	$-m_3$	$-m_2$	$-b_1$	$-b_3$	$-b_2$	19	m_3	m_2	$-m_1$	b_3	b_2	$-b_1$
8	$-m_3$	$-m_1$	m_2	$-b_3$	$-b_1$	b_2	20	$-m_3$	m_2	m_1	$-b_3$	b_2	b_1
9	m_2	$-m_1$	m_3	b_2	$-b_1$	b_3	21	$-m_1$	m_2	$-m_3$	$-b_1$	b_2	$-b_3$
10	m_2	m_1	$-m_3$	b_2	b_1	$-b_3$	22	m_1	m_2	m_3	b_1	b_2	b_3
11	$-m_2$	$-m_3$	m_1	$-b_2$	$-b_3$	b_1	23	$-m_3$	$-m_2$	$-m_1$	$-b_3$	$-b_2$	$-b_1$
12	$-m_2$	m_3	$-m_1$	$-b_2$	$-b_3$	b_1	24	m_3	$-m_2$	m_1	b_3	$-b_2$	b_1

Table 3.1: Components of the twenty-four martensite habit-plane vector pairs $(\mathbf{m}_\alpha, \mathbf{b}_\alpha)$ for Nitinol

where $\mathbf{U}_i, \mathbf{U}_j$ are the LCV stretches with the twin rotation $\mathbf{R}_{ij}$, the twin shear $\mathbf{a}$, and the unit normal to the twin plane $\hat{\mathbf{n}}$ are to be determined. Necessary and sufficient conditions for the existence of solutions to (3.9) are given in [33]. Then, the habit-plane equation is solved for each twin pair in the form

$$\bar{\mathbf{R}}_{ij}(\lambda \mathbf{R}_{ij}\mathbf{U}_i + (1-\lambda)\mathbf{U}_j) \;=\; \mathbf{I} + \mathbf{b} \otimes \hat{\mathbf{m}} \;, \tag{3.10}$$

where the habit-plane rotation $\bar{\mathbf{R}}_{ij}$, the twin volume fraction λ, the shape strain $\mathbf{b}$ and the habit-plane unit normal $\hat{\mathbf{m}}$ are to be determined. Figure 3.2 depicts schematically this habit-plane deformation between austenite and martensite phases. The above equation gives the compatibility between average deformation of twinned martensite due to LCV pair $(i : j)$ and austenite. The right-hand side gives the transformation deformation gradient for the habit-plane variant denoted as $\mathbf{F}^t_{ij}$. Appealing to the twinning equation (3.9), equation (3.10) can be written as

$$\bar{\mathbf{R}}_{ij}(\mathbf{U}_i + \lambda \mathbf{a} \otimes \hat{\mathbf{n}}) \;=\; \mathbf{I} + \mathbf{b} \otimes \hat{\mathbf{m}} \;. \tag{3.11}$$

Note, that the above equation can be rewritten as

$$\bar{\mathbf{R}}_{ij}\left(\mathbf{I} + \lambda \mathbf{a} \otimes \hat{\mathbf{n}}\mathbf{U}_i^{-1}\right)\mathbf{U}_i \;=\; \mathbf{I} + \mathbf{b} \otimes \hat{\mathbf{m}} \;, \tag{3.12}$$

where the term in parentheses is called the lattice-invariant shear. Thus the various parts of habit-plane deformation are the Bain strain for lattice deformation, lattice-invariant shear for twinning and the habit-plane rotation necessary to form a compatible habit-plane with austenite. An algorithm for obtaining solution to (3.11) is outlined in [33]. Applying this procedure for the cubic-monoclinic (B2-B19′) phase transformation in Nitinol gives up to

528 habit-plane solutions. However, many of these habit-plane solutions involve Type-I or Compound martensite twins (see [33] for definitions of different twin types), which do not occur in Nitinol under working conditions of thermomechanical loading. So theoretically it can be argued that Nitinol can have up to 192 habit-plane solutions [33]. But in experiments, it is found that Nitinol exhibits only up to 24 habit-plane variants that correspond to Type-II twins [58]. These are obtained for Nitinol with composition Ti-49.8 at.% Ni that has the following lattice parameters: $a_0 = 3.015$Å for austenite, and $a = 2.889$Å, $b = 4.120$Å, $c = 4.622$Å and monoclinic angle $\beta = 96.8^\circ$ for martensite. Hence, only these habit-plane variants have been considered in this work. They are given in Table 3.1, where the components of $\hat{\mathbf{m}}$ and $\mathbf{b}$ are given in terms of the following vectors with respect to the austenite basis,

$$\begin{aligned} [m_1, m_2, m_3] &= [-0.88888, 0.21523, 0.40443] \ , \\ [b_1, b_2, b_3] &= [0.05682, 0.09906, 0.06374] \ . \end{aligned} \tag{3.13}$$

3.3.3 Formation of intermediate R-phase

Depending on composition and heat treatment of the Nitinol specimen, an intermediate rhombohedral phase (or R-phase) has been observed to form before martensitic transformation, during quasistatic mechanical loading. The lattice geometry of this phase is critically dependent on specimen temperature, see [63, 80, 70]. The transformation strains associated with austenite-R-phase (B2-R) transformation are quite small, and further, it occurs at low stress levels under room temperature. See Figure 1.1, where this transformation is observed at stress levels of 150-200 MPa. However, presence of R-phase affects the transformation path for R-phase-martensite (R-B19′) transformation.

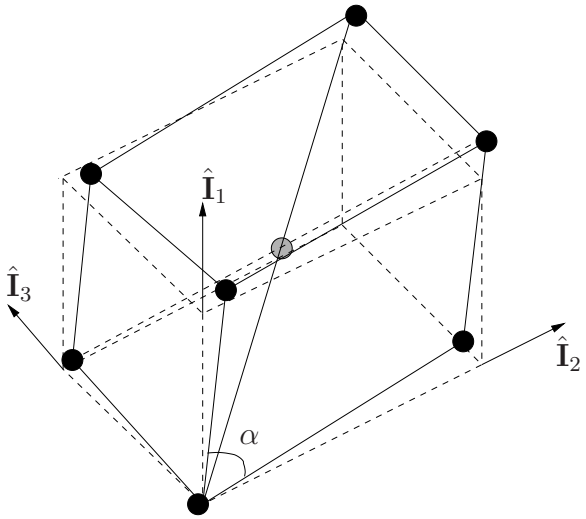

Figure 3.3: *Crystallography for B2-R-B19′ transformation*

The rhombohedral unit cell is obtained by stretching the austenite unit cell along the [111] direction. The corresponding Bain strain depends on the rhombohedral angle α, which is defined as the angle between the deformed [100] and [010] axes of the austenite unit cell in the R-phase. Figure 3.3 shows the deformation of austenite unit cell into the R-phase unit cell. It has been found that α varies continuously with temperature and usually decreasing with decreasing temperature [62, 84, 18]. It is known to be approximately equal to 89.5° at room temperature. There are 4 LCVs for R-phase and all 6 combinations of them form twins, hence satisfy the twinning equation (3.9), see [34]. There are 12 solutions to the habit-plane equation (3.11), which are generated from the following vectors by appropriate orthogonal transformations: $[b_1, b_2, b_3] = [0.00000, 0.00865, 0.00008]$ and $[m_1, m_2, m_3] = [0.00000, -0.00440, -0.99999]$. These habit-plane variants were computed based on the procedure outlined in Section 3.3.2 and are listed in Table 3.2. The number of these B2-R habit-plane variants is in agreement with the crystallography of B2-R-B19′ transformations in [94], where twelve R-phase variants with compound twins were found to form for $\alpha < 90°$. See [33] for definition of compound twins.

In contrast to the B2-R case, the variants of R-B19′ transformation are not well characterized, since they strongly depend on the microstructure of R-phase. Applying the analytical approach discussed earlier, the possibility of formation of compound and Type-I martensitic twins has been explored in [94] for certain values of rhombohedral angles. At the same time, experimental observation for Nitinol under superelastic loading appears to be limited to only Type-II martensite twins. Further, it is possible that even though other martensitic variants are initially formed to preserve compatibility with the R-phase variants, they are eventually reoriented to the well-known B19′ variants with continued loading. In the absence of sufficient experimental evidence of occurrence of the martensitic variants dictated by aforementioned

#	$\mathbf{b}$			$\hat{\mathbf{m}}$		
1	b_2	b_1	$-b_3$	m_2	m_1	$-m_3$
2	b_3	b_1	$-b_2$	m_3	m_1	$-m_2$
3	b_3	$-b_2$	b_1	m_3	$-m_2$	m_1
4	b_2	$-b_3$	b_1	m_2	$-m_3$	m_1
5	b_1	b_2	$-b_3$	m_1	m_2	$-m_3$
6	b_1	b_3	$-b_2$	m_1	m_3	$-m_2$
7	b_1	b_3	b_2	m_1	m_3	m_2
8	b_1	b_2	b_3	m_1	m_2	m_3
9	b_2	b_3	b_1	m_2	m_3	m_1
10	b_3	b_2	b_1	m_3	m_2	m_1
11	b_3	b_1	b_2	m_3	m_1	m_2
12	b_2	b_1	b_3	m_2	m_1	m_3

Table 3.2: Components of the twelve R-phase habit-plane vector pairs $(\mathbf{b}_\alpha, \hat{\mathbf{m}}_\alpha)$ for Nitinol

algorithm, the 24 habit-plane variants that are usually observed in B2-B19′ transformation (Table 3.1) are also used in this work. This choice of martensitic variants implies that there is no one-to-one correspondence between the R-phase variants and the B19′ variants formed along the R-B19′ path. The implications of this important assumption will be examined in the constitutive development in Chapter 5.

3.4 Use of multiplicative decomposition kinematics for phase transformation

Displacive phase transformations include infinitesimal to moderate elastic stretching (1-3% strain) of the crystal lattice and moderate to large deformation (3-10% strain) due to the austenite-martensite transformation [59]. Due to the latter, finite-deformation theory is employed to describe the kinematics of the underlying continuum-mechanical problem. In recent years, several authors have adopted a multiplicative decomposition of the total deformation gradient $\mathbf{F}$ in the crystal grain into elastic and transformation counterparts $\mathbf{F}^e$ and $\mathbf{F}^t$, respectively, such that

$$\mathbf{F} \;=\; \mathbf{F}^e\mathbf{F}^t \;, \tag{3.14}$$

see, *e.g.*, [90, 3, 85]. The multiplicative decomposition (3.14) originates in the differential-geometric continuum theory of Kröner [48] and has been since employed with success in the context of inelastic deformations, see earlier discussion in Section 2.1.2.

In crystal plasticity, the inelastic deformation is equal to the total deformation in a local intermediate configuration obtained by elastically unloading to a state of zero stress or, if

such state is unattainable, to a state of maximal unloading (i.e., unloading up to the onset of inelastic deformation) [15]. The argument of local unloading to a state of zero elastic strain applied in that case does not readily apply to displacive phase transformation. This is because purely mechanical unloading at temperatures where the material exhibits superelastic behavior causes reverse transformation before the elastic deformation is fully released. On the other hand, unloading to zero stress at constant temperature results in complete vanishing of all strain. This material behavior poses a conceptual difficulty in the definition of an intermediate configuration which is intended to reflect the undisturbed martensitic microstructure, yet be devoid of elastic deformation. Indeed, no attempt appears to have been made in earlier works to justify the existence of such an intermediate configuration in the context of displacive phase transformations. Further, arbitrary superposed rotations result in a non-unique intermediate configuration and may lead to problems with invariance, which was discussed earlier for inelastic deformation in single crystals in Section 2.1.2. These issues have not been raised (let alone resolved) when employing a multiplicative decomposition of the deformation gradient for displacive phase transformation. A prescription for the intermediate configuration and a way to satisfy the invariance requirements is discussed below.

3.4.1 Clausius-Clapeyron equation for shape-memory alloys

It is well-known that the stress in SMAs depends non-linearly on both strain and temperature. Figures 3.4 and 3.5 show typical stress-strain and stress-strain-temperature curves along with the corresponding austenite-martensite transformation regimes. The slopes of the boundary lines between different phases in the stress-temperature plots are obtained by applying the Clausius-Clapeyron equation for two-phase media in equilibrium. This equation has been applied to shape-memory alloys for uniaxial stress and small deformations, see [70]. In this section, the Clausius-Clapeyron equation is derived for a general stress state and finite deformation. This equation will be subsequently employed to construct a configuration which is free of elastic deformation.

For a crystal grain of SMA, the specific Gibbs free energy takes the form $\hat{G}(\mathbf{P}, \theta, \boldsymbol{\xi})$, where $\mathbf{P}$ is the 1st Piola-Kirchhoff stress, θ is the absolute temperature, and $\boldsymbol{\xi}$ is the nv-dimensional vector of the martensite habit-plane variant volume fractions, expressed in component form as $\xi_\alpha = \frac{V_0^{(\alpha)}}{V_0}$, $\alpha = 1, 2, \ldots, nv$. The driving force vector for phase transformation at a given thermodynamic state is then defined as $-\dfrac{\partial \hat{G}}{\partial \boldsymbol{\xi}}$, see, e.g., [86, 82]. It follows that, given two states of an SMA with unequal volume fractions of martensite variants at the same stress and temperature, the total driving force f of transformation from the state with the higher Gibbs free energy and volume fraction vector $\boldsymbol{\xi}_h$ to the state with the lower Gibbs free energy

and volume fraction vector $\boldsymbol{\xi}_l$ is

$$f \;=\; -\int_{\boldsymbol{\xi}_h}^{\boldsymbol{\xi}_l} \left.\frac{\partial \hat{G}}{\partial \boldsymbol{\xi}}\right|_{\mathbf{P},\theta \text{ fixed}} \cdot d\boldsymbol{\xi} \;=\; \hat{G}(\mathbf{P},\theta,\boldsymbol{\xi}_h) - \hat{G}(\mathbf{P},\theta,\boldsymbol{\xi}_l)\ . \tag{3.15}$$

Note that the driving force f is calculated in (3.15) as an integral of a partial derivative with respect to the volume fraction vector, hence is independent of the path from the one thermodynamic state to the other as long as stress and temperature remain constant. Phase transformation occurs between the preceding two states when the driving force reaches a critical value. The lines in Figures 3.4 and 3.5 associated with zero-stress temperatures M_s (Martensite-start) and A_s (Austenite-start) correspond to the driving forces reaching such a critical value for forward and reverse transformation, respectively.

Consider two thermodynamic states, referred to as states (I) and (II) with the same stress and temperature corresponding to point (d) in Figures 3.4 and 3.5, but different volume fraction vectors $\boldsymbol{\xi}_1$ and $\boldsymbol{\xi}_2$. Further, assume that the total driving force of transformation from one state to another is equal to a critical value f_{cr}, namely, with reference to (3.15),

$$\hat{G}(\mathbf{P},\theta\,\boldsymbol{\xi}_1) - \hat{G}(\mathbf{P},\theta\,\boldsymbol{\xi}_2) \;=\; f_{cr}\ . \tag{3.16}$$

This implies that the two states are at the onset of transformation from state $\boldsymbol{\xi}_1$ to state $\boldsymbol{\xi}_2$. For state (I) to remain at the onset of transformation to state (II) under infinitesimal changes to stress and temperature, it is necessary and sufficient that $df = 0$, hence

$$d\hat{G}(\mathbf{P},\theta,\boldsymbol{\xi}_1) \;=\; d\hat{G}(\mathbf{P},\theta,\boldsymbol{\xi}_2) \tag{3.17}$$

or

$$\left.\frac{\partial \hat{G}}{\partial \mathbf{P}}\right|_{\boldsymbol{\xi}=\boldsymbol{\xi}_1} \cdot d\mathbf{P} + \left.\frac{\partial \hat{G}}{\partial \theta}\right|_{\boldsymbol{\xi}=\boldsymbol{\xi}_1} d\theta \;=\; \left.\frac{\partial \hat{G}}{\partial \mathbf{P}}\right|_{\boldsymbol{\xi}=\boldsymbol{\xi}_2} \cdot d\mathbf{P} + \left.\frac{\partial \hat{G}}{\partial \theta}\right|_{\boldsymbol{\xi}=\boldsymbol{\xi}_2} d\theta\ . \tag{3.18}$$

Taking into account the well-known relations $\dfrac{\partial G}{\partial \mathbf{P}} = -\mathbf{F}$, where $\mathbf{F}$ is the deformation gradient, and $\dfrac{\partial G}{\partial \theta} = -\eta$, where η is the specific entropy, equation (3.18) becomes

$$\mathbf{F}_1 \cdot d\mathbf{P} + \eta_1\ d\theta \;=\; \mathbf{F}_2 \cdot d\mathbf{P} + \eta_2\ d\theta\ , \tag{3.19}$$

where $\mathbf{F}_i$, η_i denote the deformation gradient and entropy associated with state $(\mathbf{P},\theta,\boldsymbol{\xi}_i)$. Equation (3.19) can be restated as

$$\Delta\mathbf{F} \cdot \frac{d\mathbf{P}}{d\theta} \;=\; -\Delta\eta \;=\; -\frac{\Delta H}{\theta}\ , \tag{3.20}$$

where H is the enthalpy and Δ denotes difference between quantities evaluated for the two states. It is noted that the difference of enthalpy ΔH is the latent heat due to a change of

deformation $\Delta\mathbf{F}$. It is also important to emphasize that, in general, $\Delta\mathbf{F}$ involves changes to both the elastic and the transformation deformation.

In conclusion, the thermoelastic unloading to zero stress in the ten-dimensional stress-temperature space is subject to the scalar equation (3.20). Since $\Delta\mathbf{F}$ and $\Delta\eta$ (or equivalently, ΔH) are prescribed in terms of partial derivatives of the Gibbs free energy, equation (3.20) constrains the stress-temperature space to a nine-parameter family of paths that may take an initial state $(\mathbf{P}\ , \theta)$ to the final stress-free state $(\mathbf{0}\ , A_s)$.

3.4.2 The nature of the intermediate configuration

In the case of SMAs, purely mechanical unloading from any partially transformed state leads to a partial or complete reverse transformation to austenite depending on whether the temperature is lower or higher than A_f, respectively, as shown in Figures 3.4 and 3.5. Therefore, the only way for a partially transformed material to locally reach a state of zero stress while leaving the transformation undisturbed is to unload mechanically from point (c) to (d), followed by a coupled thermomechanical unloading from point (d) to (f), see Figures 3.4(b) and 3.5(b). This means that a neighborhood which is unloaded to relieve all stresses needs to be simultaneously cooled along any path defined by (3.20) in order to leave the state of transformation unaltered. The transformation state remains unaltered because the driving force for any changes to the transformation never exceeds the critical value f_{cr} defined in Section 3.4.1.

Note that the preceding thermoelastic unloading results in thermal strains, which are generally small and can be deduced from the thermal expansion coefficient of the material. Indeed, at constant $\boldsymbol{\xi}$, assume that the SMA behaves as a thermoelastic solid, for which $\mathbf{P} = \hat{\mathbf{P}}(\mathbf{F}^e, \theta)$. This, in turn, implies that, after unloading to zero stress, the elastic deformation due to thermal effect is obtained from the equation

$$\hat{\mathbf{P}}(\mathbf{F}^e, \theta)\Big|_{\theta=A_s} \;=\; \mathbf{0}\ . \tag{3.21}$$

If $\dfrac{\partial\hat{\mathbf{P}}}{\partial\mathbf{F}^e}$ is invertible, then the residual deformation due to cooling can be determined directly from (3.21). This deformation can be removed completely by applying the stress

$$\mathbf{P}_{th} \;=\; \hat{\mathbf{P}}(\mathbf{I}, A_s)\ . \tag{3.22}$$

This additional stress does not effect any additional transformation, see path (f)-(g) in Figures 3.4(b) and 3.5(b). The deformation in the resulting state is now equal to the total transformation deformation $\mathbf{F}^t$.

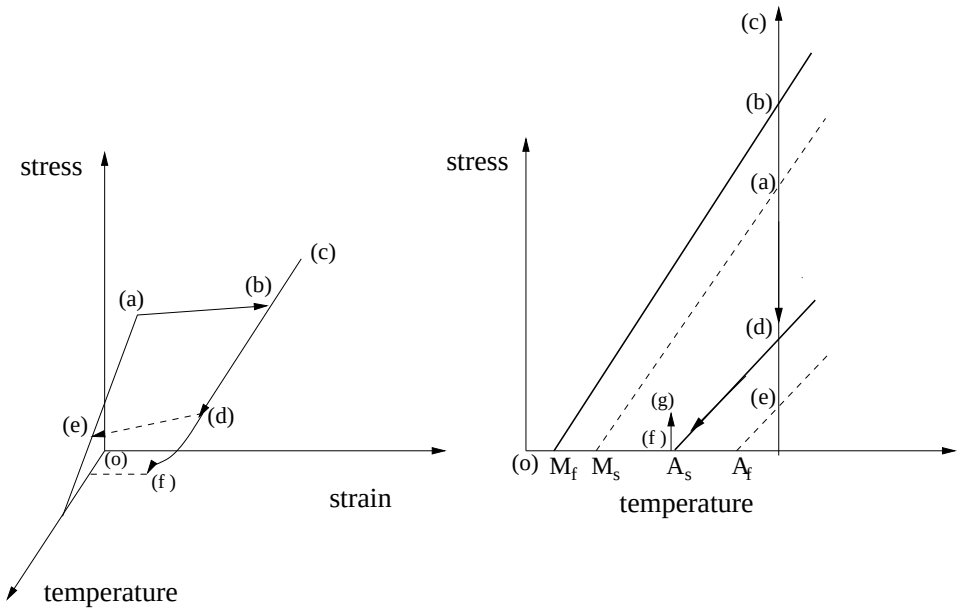

(a) stress−strain−temperature plot (b) stress−temperature phase diagram

Figure 3.4: *Stress-strain plot for superelasticity and corresponding stress-temperature diagram*

3.4.3 Construction of a multiplicative decomposition

In this section, the mesoscale kinematics of deformation is constructed for a crystal grain undergoing phase transformation. To this end, consider an infinitesimal material line element $d\mathbf{X}$ at a material point X in the reference configuration, and let it be mapped locally to the line element $d\mathbf{y}$ in intermediate configuration. If the intermediate configuration exists and is free of elastic deformation, then the change from $d\mathbf{x}$ to $d\mathbf{y}$ is due exclusively to phase transformation and

$$d\mathbf{y} \;=\; \mathbf{F}^t \; d\mathbf{x} \; . \tag{3.23}$$

The transformation gradient $\mathbf{F}^t$ may be taken to be the average transformation deformation gradient over an appropriately chosen microstructural Representative Volume Element (RVE) occupying a domain ω_0 with volume V_0, namely

$$\mathbf{F}^t \;=\; \frac{1}{V_0} \int_{\omega_0} \hat{\mathbf{F}}^t \; dV_0 \; , \tag{3.24}$$

where $\hat{\mathbf{F}}^t$ denotes the microscale transformation deformation gradient. If the domain ω_0 is decomposed into mutually disjoint sub-domains $\omega_0^{(\alpha)}$, $\alpha = 0, 1, \ldots, nv$, corresponding to the regions of austenite phase ($\alpha = 0$) and the nv martensitic variants, equation (3.24) may be

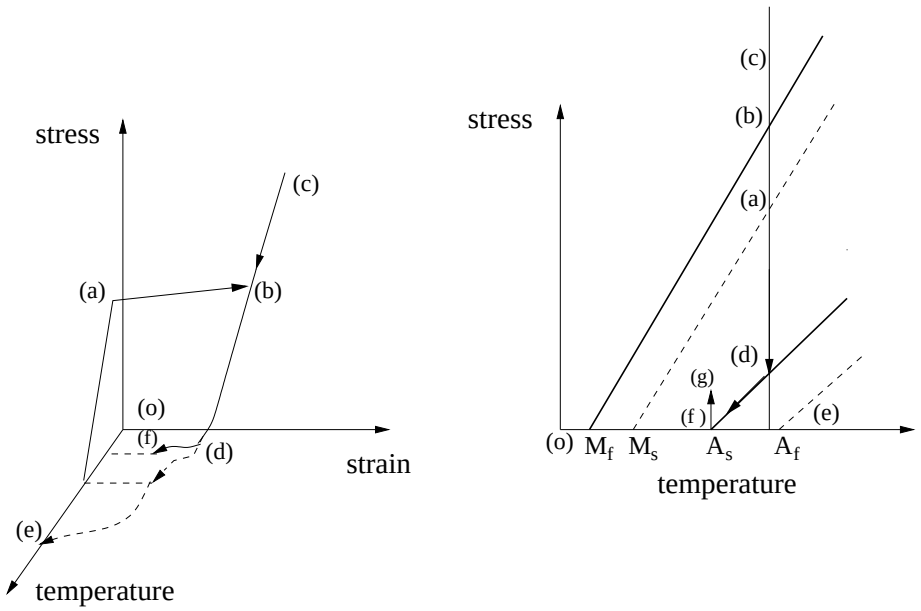

(a) stress−strain−temperature plot (b) stress−temperature phase diagram

Figure 3.5: *Stress-strain-temperature plot for partial superelastic and shape- memory behavior and corresponding stress-temperature diagram*

rewritten as

$$\mathbf{F}^t \;=\; \frac{1}{V_0}\sum_{\alpha=0}^{nv}\int_{\omega_0^{(\alpha)}} \hat{\mathbf{F}}^t_\alpha \; dV_0^{(\alpha)} \;, \tag{3.25}$$

where $\hat{\mathbf{F}}^t_0 = \mathbf{I}$ in the region $\omega_0^{(0)}$ of austenite. The variant habit-plane deformation $\hat{\mathbf{F}}^t_\alpha$ is assumed constant over each of the sub-domains $\omega_0^{(\alpha)}$ occupying volumes $V_0^{(\alpha)}$, respectively. Hence, the transformation deformation gradient can be expressed as

$$\mathbf{F}^t \;=\; \sum_{\alpha=0}^{nv} \xi_\alpha \hat{\mathbf{F}}^t_\alpha \;, \tag{3.26}$$

where $\xi_0 = 1 - \sum_{\alpha=1}^{nv} \xi_\alpha$ is the volume fraction of the austenite.

Once $\mathbf{F}^t$ is constructed according to (3.26), the elastic deformation gradient is given by

$$\mathbf{F}^e \;=\; \mathbf{F}\mathbf{F}^{t^{-1}} \;. \tag{3.27}$$

3.4.4 Invariance with respect to the intermediate configuration

The issue of invariance with respect to the intermediate configuration for inelastic deformation in single crystals was discussed in Section 2.1.1. In single-crystal SMAs, a "director

frame" required for invariance may be attached to the lattice vectors of the parent austenite phase. In this case, the habit-plane variant deformations $\hat{\mathbf{F}}^t_\alpha$ are acting on material line elements aligned with this director frame. Therefore, the mesoscale transformation deformation gradient $\mathbf{F}^t$ in (3.26) is invariant under arbitrary rotations of the intermediate configuration. The invariance of this model is naturally inherited by textured polycrystalline SMAs. This is explained further in the following section.

3.5 Influence of texture and measurement procedure

In a polycrystalline material, the crystal grains have different orientations with respect to global axes of the specimen. However, if the orientations of the crystals in a polycrystalline aggregate were totally random, then the overall behavior of the polycrystal would have been isotropic. But, depending on processing of the material, crystals are preferentially oriented along certain directions to within some statistical deviations. This gives rise to an overall anisotropic behavior of the polycrystal. It was argued in [81] that texture influences the recoverable strains under superelastic loading to a great extent in polycrystalline SMAs. Also, Gall et al. [25] showed that texture in SMAs leads to asymmetric behavior under tension and compression. Moreover, the loading conditions governing the onset of phase transformation is also dependent on the texture. From a micromechanics perspective, this can be understood to be due to transformation of different sets of martensite variants depending on the crystal orientation relative to the loading direction.

Texture is usually inferred from pole figures generated through X-ray diffraction analysis. The pole figures are stereographic projections of intersections of a crystal axes with the surface of a unit sphere , see [46]. This is post-processed to determine the orientation density function (ODF) which is a measure of the relative probabilities of occurrence of different crystal orientations. For the data used in this work based on experimental NiTi tubes, the ODF was obtained by the data analysis program BEARTEX [92]. This data can be used to create a data file for simulation purposes, which contains triplets of pole angles used to describe crystal orientations, relative to the sample coordinate system. The angles are usually given in the Roe/Matthies convention which is illustrated by Figure 3.6. In this figure, $\{\alpha, \beta, \gamma\}$ are the Euler angles in Roe/Matthies convention which rotate the specimen basis vectors $\{\mathbf{p}, \mathbf{q}, \mathbf{r}\}$ to basis vectors $\{\mathbf{p}''', \mathbf{q}''', \mathbf{r}''\}$ along the crystallographic axes (x, y, z). The probabilities of occurrence of the different crystal orientations can be suitably represented in simulations, by having the data file contain multiple occurrences of the angle triplets. The multiplicity of occurrence of each triplet is taken to be proportional to its probability deduced from the ODF. Thus, a random sampling of angle triplets from this data file to assign orientations to crystals, is sufficient to account for the experimental texture of the NiTi specimen. The procedure of using these orientations in determining the transformation strains of polycrystals, will be elaborated in Chapter 7.

In previous section the invariance issue related to kinematics of phase transformation

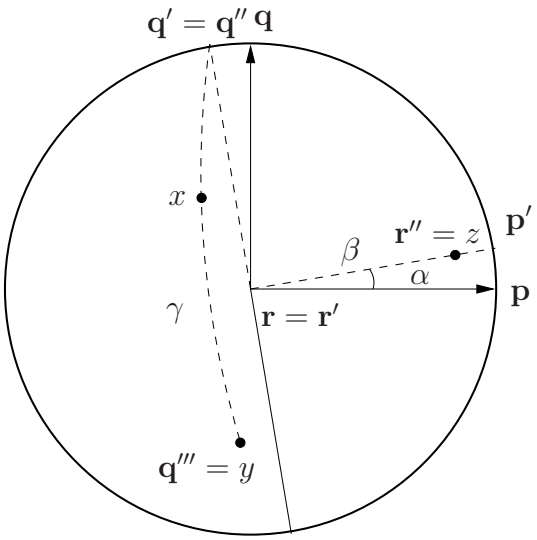

Figure 3.6: *Transformation from the sample coordinate system to the crystallographic axes*

was clarified for single crystal SMAs. With the above information on polycrystal texture, this issue can also be resolved for textured polycrystalline SMAs. Indeed, recall that the total deformation is always measured relative to the global (laboratory) frame of specimen. If the mapping between this global frame and the director frame in each crystal of the polycrystal aggregate is known by the aforementioned procedure, then the variant habit-plane deformations $\hat{\mathbf{F}}^t_\alpha$ can be readily resolved on this global frame. As a result, the transformation deformation of the polycrystalline aggregate (resulting from homogenization of its single-crystal counterparts) is also invariant under superposed rigid motions.

Chapter 4

Constitutive model of Nitinol

In this chapter, a new constitutive model is developed for the fuly-coupled thermomechanical response of Nitinol. If the loading on a Nitinol specimen allows temperature changes, phase transformations are affected as a result, which in turn influences the mechanical deformation of the specimen. On the other hand, stress-induced phase transformations are associated with latent heat exchange and dissipation that could influence the temperature if this heat generated is not dispersed to the surroundings. This fully-coupled response of Nitinol entails solving both deformation and temperature states, by satisfying the momentum and energy equations. Here, specific forms are derived for the stress and temperature evolution, after proposing a constitutive model in terms of the Helmholtz free energy. Later, this model is compared to two other models, one of which is proposed in [3]. Further, a novel algorithmic scheme is devised to solve the resulting transformation equations subject to all the necessary constraints on the martensite variants. This scheme starts by selecting a set of potentially active variants, but instead of enforcing the constraints *a posteriori* on the volume fractions as in [90], proceeds with a predictor-corrector approach that fully couples the transformation equations to the constraints.

Experiments done on Nitinol at different strain-rates support the inter-dependence between temperature and deformation, see [67, 31]. While this has been modeled in previous works [3, 16], the numerical results have not been quantitatively compared to experiments. In this work, experiments on thin-walled tubes at different strain rates are initially used to estimate some of the material parameters and the heat transfer coefficient due to convection between the specimen and air. Subsequently, the simulation results are compared to a wider set of experiments for validation purposes.

4.1 Constitutive models for phase transformation

4.1.1 Mesoscale kinematics of phase transformation

The microstructure of crystal grain in a material undergoing martensitic phase transition comprises sub-domains of untransformed austenite and habit-plane variants of martensite. The overall deformation of the grain may be characterized through homogenization of the deformation in these sub-domains. In the primary model presented here, the mesoscale total deformation gradient is decomposed multiplicatively into elastic and transformation counterparts (3.14). The theoretical underpinnings of the use of this decomposition in the context of martensitic phase transformations has been discussed at length in Section 3.4, also see [78]. This decomposition is restated here for sake of continuity as

$$\mathbf{F} = \mathbf{F}^e\mathbf{F}^t \ , \tag{4.1}$$

where $\mathbf{F}^e$ and $\mathbf{F}^t$ are the elastic and transformation deformation gradients. The total transformation deformation gradient is expressed in terms of the transformation gradients $\mathbf{F}^t_\alpha$, $\alpha = 1, 2, \ldots, nv$, associated with each of the nv martensitic variants as

$$\mathbf{F}^t \ = \ (1 - \sum_{\alpha=1}^{nv} \xi_\alpha)\mathbf{I} + \sum_{\alpha=1}^{nv} \xi_\alpha \mathbf{F}^t_\alpha \ . \tag{4.2}$$

Here, ξ_α is the volume fraction of the α-th martensitic variant and $\mathbf{I}$ is the second-order identity tensor corresponding to the transformation deformation gradient of the parent austenite phase [78]. The kinematics of the solid-solid phase transformation requires that

$$\mathbf{F}^t_\alpha \ = \ \mathbf{I} + \mathbf{H}^t_\alpha \ , \tag{4.3}$$

where the displacement gradient $\mathbf{H}^t_\alpha$ for the variant α is written in terms of the habit-plane displacement $\mathbf{b}_\alpha$ and the corresponding habit-plane normal $\mathbf{m}_\alpha$ as $\mathbf{H}^t_\alpha = \mathbf{b}_\alpha \otimes \mathbf{m}_\alpha$. It follows from (4.2) and (4.3) that

$$\mathbf{F}^t \ = \ \hat{\mathbf{F}}^t(\{\xi_\alpha\}) \ = \ \mathbf{I} + \sum_{\alpha=1}^{nv} \xi_\alpha \mathbf{H}^t_\alpha \ . \tag{4.4}$$

Hence, the rate of the transformation decomposition gradient is given by

$$\dot{\mathbf{F}}^t \ = \ \sum_{\alpha=1}^{nv} \dot{\xi}_\alpha \mathbf{H}^t_\alpha \ , \tag{4.5}$$

where it is assumed that the reference configuration of the underlying austenite lattice remains unchanged with respect to the laboratory frame of reference.

Given the elastic deformation gradient in (4.1), the elastic Green-Lagrange strain relative to the intermediate configuration induced by $\mathbf{F}^t$ is

$$\mathbf{E}^e \;=\; \frac{1}{2}(\mathbf{C}^e - \mathbf{I}) \;=\; \frac{1}{2}(\mathbf{F}^{eT}\mathbf{F}^e - \mathbf{I}) \;=\; \frac{1}{2}(\mathbf{F}^{t-T}\mathbf{C}\mathbf{F}^{t-1} - \mathbf{I}) \;, \tag{4.6}$$

where $\mathbf{C}(=\mathbf{F}^T\mathbf{F})$ is the right Cauchy-Green deformation tensor and $\mathbf{C}^e(=\mathbf{F}^{eT}\mathbf{F}^e)$ is its elastic counterpart. Therefore, the rate of change of the elastic Green-Lagrange strain becomes

$$\dot{\mathbf{E}}^e \;=\; \frac{1}{2}(\dot{\mathbf{F}}^{eT}\mathbf{F}^e + \mathbf{F}^{eT}\dot{\mathbf{F}}^e) \;. \tag{4.7}$$

4.1.2 Derivation of energy equation for phase transformation

The energy balance equation in reference configuration is stated here as

$$\rho_0\dot{\epsilon} \;=\; \rho_0 r - \mathrm{Div}\mathbf{q}_0 + \mathbf{P}\cdot\dot{\mathbf{F}} \;. \tag{4.8}$$

Note that this is equivalent to (2.23), through the power identity $\mathbf{S}\cdot\dot{\mathbf{E}} = \mathbf{P}\cdot\dot{\mathbf{F}}$. Appealing to the multiplicative decomposition in (4.1), the stress power term in (4.8) can be expanded to

$$\mathbf{P}\cdot\dot{\mathbf{F}} \;=\; \mathbf{P}\cdot(\dot{\mathbf{F}}^e\mathbf{F}^t + \mathbf{F}^e\dot{\mathbf{F}}^t) \;. \tag{4.9}$$

Taking into account (4.1) and (4.7), the term on the right-hand side of (4.9) that involves the rate of the elastic deformation gradient can be written as

$$\mathbf{P}\cdot(\dot{\mathbf{F}}^e\mathbf{F}^t) \;=\; \mathbf{S}^e\cdot\dot{\mathbf{E}}^e \;, \tag{4.10}$$

where $\mathbf{S}^e$ is a symmetric tensor given by

$$\mathbf{S}^e \;=\; \mathbf{F}^{e-1}\mathbf{P}\mathbf{F}^{tT} \;=\; \mathbf{F}^t\mathbf{S}\mathbf{F}^{tT} \tag{4.11}$$

and $\mathbf{S}$ $(=\mathbf{F}^{-1}\mathbf{P})$ is the second Piola-Kirchhoff stress. Hence, $\mathbf{S}^e$ is the push-forward of second Piola-Kirchhoff stress to the intermediate configuration. Therefore, the quantity in (4.10) is understood to be the elastic power. Furthermore, with the aid of (4.4) the second term on the right-hand side of (4.9) can be expressed as

$$\mathbf{P}\cdot(\mathbf{F}^e\dot{\mathbf{F}}^t) \;=\; \sum_\alpha(\mathbf{F}^{eT}\mathbf{P})\cdot(\dot{\xi}_\alpha\mathbf{H}^t_\alpha) \;=\; \sum_\alpha(\mathbf{F}^{eT}\mathbf{P}^e)\cdot(\mathbf{H}^t_\alpha\mathbf{F}^{t-1})\dot{\xi}_\alpha \;, \tag{4.12}$$

where, upon recalling (4.11),

$$\mathbf{P}^e \;=\; \mathbf{P}\mathbf{F}^{tT} \;=\; \mathbf{F}^e\mathbf{S}^e \tag{4.13}$$

is the push-forward of $\mathbf{P}$ to the intermediate configuration. Denoting by τ_α the work-conjugate kinetic quantity to ξ_α, namely setting $\tau_\alpha = (\mathbf{F}^{eT}\mathbf{P}^e)\cdot(\mathbf{H}^t_\alpha\mathbf{F}^{t-1}) = (\mathbf{C}^{eT}\mathbf{S}^e)\cdot(\mathbf{H}^t_\alpha\mathbf{F}^{t-1})$, it follows that

$$\mathbf{P}\cdot(\mathbf{F}^e\dot{\mathbf{F}}^t) \;=\; \sum_\alpha \tau_\alpha\dot{\xi}_\alpha \;. \tag{4.14}$$

It is clear that the term in (4.12) quantifies the inelastic power and contributes to dissipation, as will be seen in Section 4.1.3. Taking into account (4.9), (4.10), (4.14) and the definition of $\mathbf{S}$, the energy equation (4.8) may be rewritten as

$$\rho_0\dot{\epsilon} \;=\; \rho_0 r - \mathrm{Div}\mathbf{q}_0 + \mathbf{P}\cdot\dot{\mathbf{F}} \;=\; \rho_0 r - \mathrm{Div}\mathbf{q}_0 + \mathbf{S}^e\cdot\dot{\mathbf{E}}^e + \sum_\alpha \tau_\alpha\,\dot{\xi}_\alpha\;. \tag{4.15}$$

4.1.3 A thermomechanical phase transformation model

In this section, a Helmholtz free energy is proposed for the phase transformation of Nitinol by adding together all relevant entropic, thermomechanical, and chemical contributions. To this end, recall that the Helmholtz free energy is related to the internal the internal energy ϵ and the entropy η by

$$\Psi \;=\; \rho_0(\epsilon - \eta\theta)\;. \tag{4.16}$$

Next, assume that the internal energy and the entropy depend on the elastic Green-Lagrange strain $\mathbf{E}^e$, the volume fractions $\{\xi_\alpha\}$ of the martensite variants (which characterize the transformation state), and the absolute temperature θ. By virtue of (4.16), this means that the free energy is expressed as $\Psi = \bar{\Psi}(\mathbf{E}^e, \{\xi_\alpha\}, \theta)$. Appealing to $(4.15)_2$, (4.16) and the constitutive dependencies of $\bar{\Psi}$, the Clausius-Duhem inequality (2.33) results in

$$\left(\frac{\partial\bar{\Psi}}{\partial\mathbf{E}^e} - \mathbf{S}^e\right)\cdot\dot{\mathbf{E}}^e + \left(\frac{\partial\bar{\Psi}}{\partial\theta} + \rho_0\eta\right)\dot{\theta} + \sum_\alpha\left(\frac{\partial\bar{\Psi}}{\partial\xi_\alpha} - \tau_\alpha\right)\dot{\xi}_\alpha + \frac{\mathbf{q}_0\cdot\mathrm{Grad}\,\theta}{\theta} \;\leq\; 0\;. \tag{4.17}$$

Since there exist purely thermoelastic processes (i.e., such that $\dot{\xi}_\alpha = 0$) at any state $(\mathbf{E}^e, \{\xi_\alpha\}, \theta)$, the standard Coleman-Noll argument may be applied to the preceding equation and leads to

$$\mathbf{S}^e \;=\; \frac{\partial\bar{\Psi}}{\partial\mathbf{E}^e} \quad,\quad \rho_0\eta \;=\; -\frac{\partial\bar{\Psi}}{\partial\theta} \quad,\quad -\sum_\alpha\left(\frac{\partial\bar{\Psi}}{\partial\xi_\alpha} - \tau_\alpha\right)\dot{\xi}_\alpha \;\geq\; 0 \quad,\quad \frac{\mathbf{q}_0\cdot\mathrm{Grad}\,\theta}{\theta} \;\leq\; 0\;. \tag{4.18}$$

Note that the term $\tau_\alpha\dot{\xi}_\alpha$ in $(4.18)_3$ contributes to the dissipation due to the phase transformation.

Equations $(4.6)_3$ and (4.4) reveal that the elastic Green-Lagrange strain $\mathbf{E}^e$ can be written as a function of $\mathbf{E}$ and $\{\xi_\alpha\}$. Therefore, the Helmholtz free energy may be expressed as a function of $\mathbf{E}$, $\{\xi_\alpha\}$ and θ, namely

$$\Psi \;=\; \bar{\Psi}(\mathbf{E}^e(\mathbf{E}, \{\xi_\alpha\}), \{\xi_\alpha\}, \theta) \;=\; \hat{\Psi}(\mathbf{E}, \{\xi_\alpha\}, \theta)\;. \tag{4.19}$$

This demonstrates that, in the context of the proposed model, the phase-transforming material may be viewed as an nv-parameter family of thermoelastic materials induced by the set of martensite volume fractions $\{\xi_\alpha\}$.

The constitutive equations (4.18) can be alternatively derived from the Helmholtz free energy function $\hat{\Psi}(\mathbf{E}, \{\xi_\alpha\}, \theta)$. Indeed, using $(4.15)_1$ and (4.16) and recalling the constitutive dependencies of $\hat{\Psi}$, the Clausius-Duhem inequality (2.31) leads to

$$\left(\frac{\partial \hat{\Psi}}{\partial \mathbf{E}} - \mathbf{S}\right) \cdot \dot{\mathbf{E}} + \left(\frac{\partial \hat{\Psi}}{\partial \theta} + \rho_0 \eta\right)\dot{\theta} + \sum_\alpha \frac{\partial \hat{\Psi}}{\partial \xi_\alpha}\dot{\xi}_\alpha + \frac{\mathbf{q}_0 \cdot \operatorname{Grad}\theta}{\theta} \;\leq\; 0 \,. \tag{4.20}$$

The Coleman-Noll procedure now yields the constitutive relations

$$\mathbf{S} \;=\; \frac{\partial \hat{\Psi}}{\partial \mathbf{E}} \quad , \quad \rho_0 \eta \;=\; -\frac{\partial \hat{\Psi}}{\partial \theta} \quad , \quad -\sum_\alpha \frac{\partial \hat{\Psi}}{\partial \xi_\alpha}\,\dot{\xi}_\alpha \;\geq\; 0 \quad , \quad \frac{\mathbf{q}_0 \cdot \operatorname{Grad}\theta}{\theta} \;\leq\; 0 \,. \tag{4.21}$$

Note that $(4.21)_{1,2}$ are identical in structure to (2.30), with the internal variables $\mathcal{W}$ here being the volume fractions, $\{\xi_\alpha\}$. Also, the left-hand side of $(4.21)_3$ represents the dissipation generated during phase transformation by the driving forces $f_\alpha = -\dfrac{\partial \hat{\Psi}}{\partial \xi_\alpha}$. It can be now verified using (4.16), $(4.15)_1$ and $(4.21)_{1,2}$ that the rate of entropy satisfies the relation

$$\rho_0 \dot{\eta}\theta \;=\; \rho_0 r - \operatorname{Div}\mathbf{q}_0 + \sum_\alpha f_\alpha \dot{\xi}_\alpha \,. \tag{4.22}$$

A specific choice of the Helmholtz free energy functional is now proposed. The entropic part of the energy involves only thermal effects due to temperature changes with respect to a reference temperature θ_0, chosen here to be the ambient temperature. This contribution is typically ignored for quasi-static mechanical loading, where isothermal conditions are assumed. To define the entropic part, let the volumetric heat capacity c at a given elastic Green-Lagrange strain and transformation state be

$$c \;=\; \hat{c}(\mathbf{E}^e, \{\xi_\alpha\}, \theta) \;=\; \rho_0 \frac{\partial \epsilon(\mathbf{E}^e, \{\xi_\alpha\}, \theta)}{\partial \theta} \;=\; \rho_0 \theta \frac{\partial \eta(\mathbf{E}^e, \{\xi_\alpha\}, \theta)}{\partial \theta} \,, \tag{4.23}$$

where (4.16) and $(4.18)_2$ are used in deriving $(4.23)_2$. Integrating the equations in (4.23) from θ_0 to θ yields the thermal parts of the internal energy and entropy as

$$\rho_0 \big(\epsilon(\mathbf{E}^e, \{\xi_\alpha\}, \theta) - \epsilon(\mathbf{E}^e, \{\xi_\alpha\}, \theta_0)\big) \;=\; \int_{\theta_0}^{\theta} \hat{c}(\mathbf{E}^e, \{\xi_\alpha\}, \vartheta)\, d\vartheta \tag{4.24}$$

and

$$\rho_0 \big(\eta(\mathbf{E}^e, \{\xi_\alpha\}, \theta) - \eta(\mathbf{E}^e, \{\xi_\alpha\}, \theta_0)\big) \;=\; \int_{\theta_0}^{\theta} \frac{\hat{c}(\mathbf{E}^e, \{\xi_\alpha\}, \vartheta)}{\vartheta}\, d\vartheta \,. \tag{4.25}$$

The Helmholtz free energy is deduced from (4.16), (4.24) and (4.25) by assuming that the function $\hat{c}(\mathbf{E}^e, \{\xi_\alpha\}, \vartheta)$ is constant and equal to c. In this case, one may write

$$\bar{\Psi}(\mathbf{E}^e, \{\xi_\alpha\}, \theta) \;=\; \rho_0 \big(\epsilon(\mathbf{E}^e, \{\xi_\alpha\}, \theta_0) - \eta(\mathbf{E}^e, \{\xi_\alpha\}, \theta_0)\theta\big) + c\left(\theta - \theta_0 - \theta \log\left(\frac{\theta}{\theta_0}\right)\right) \,. \tag{4.26}$$

The thermomechanical part of the free energy is assumed to satisfy the two basic relations

$$\frac{\partial^2\bar{\Psi}}{\partial\mathbf{E}^e\partial\mathbf{E}^e} \;=\; \mathbb{C} \qquad , \qquad \frac{\partial^2\bar{\Psi}}{\partial\mathbf{E}^e\partial\theta} \;=\; -\mathbb{C}\mathbf{A} \; . \tag{4.27}$$

Here, $\mathbb{C}$ is the fourth-order elastic modulus tensor given by

$$\mathbb{C} \;=\; (1-\sum_{\alpha=1}^{nv}\xi_\alpha)\mathbb{C}_a + \sum_{\alpha=1}^{nv}\xi_\alpha\mathbb{C}_m \; , \tag{4.28}$$

in terms of the respective elastic moduli $\mathbb{C}_a$ and $\mathbb{C}_m$ of the austenite and martensite phases. Also, $\mathbf{A}$ is the second-order thermal expansion tensor, assumed here to be constant. Lastly, the chemical part of free energy is taken to be a linear function of both the deviation of temperature from a thermodynamic equilibrium temperature θ_T between the austenite and martensite phases and the total martensitic volume fraction. In summary, the Helmholtz free energy takes the form

$$\begin{aligned}\Psi \;=\; \bar{\Psi}(\mathbf{E}^e,\{\xi_\alpha\},\theta) \;=\; \frac{1}{2}\mathbf{E}^e\cdot\mathbb{C}\mathbf{E}^e - \mathbf{E}^e\cdot\mathbb{C}\mathbf{A}(\theta-\theta_0) + B(\theta-\theta_T)\sum_\alpha\xi_\alpha \\ + c\left(\theta-\theta_0-\theta\,\log\left(\frac{\theta}{\theta_0}\right)\right) \; ,\end{aligned} \tag{4.29}$$

where $B(>0)$ is the chemical energy coefficient. Note that the energy due to interaction between martensitic variants is neglected in this model. A Helmholtz free energy of the functional form (4.29) has been proposed in [3], albeit starting from a completely different definition of $\mathbf{F}^t$ (thus leading to a different definition of the state variable $\mathbf{E}^e$). The relation between the two models is discussed further in Section 4.1.4.

An expression for the stress $\mathbf{S}$ may be obtained from $(4.21)_1$ with the aid of $(4.18)_1$, (4.29), (4.19), $(4.6)_3$ and the chain rule, as

$$\mathbf{S} \;=\; \left(\frac{\partial\mathbf{E}^e}{\partial\mathbf{E}}\right)^T\frac{\partial\bar{\Psi}}{\partial\mathbf{E}^e} \;=\; \mathbf{F}^{t^{-1}}\mathbf{S}^e\mathbf{F}^{t^{-T}} \; , \tag{4.30}$$

where

$$\mathbf{S}^e \;=\; \mathbb{C}\big(\mathbf{E}^e-\mathbf{A}(\theta-\theta_0)\big) \; . \tag{4.31}$$

Likewise, the entropy η is obtained from $(4.18)_2$ and (4.29) as

$$\rho_0\eta \;=\; \mathbf{E}^e\cdot\mathbb{C}\mathbf{A} - B\sum_\alpha\xi_\alpha + c\,\log\left(\frac{\theta}{\theta_0}\right) \; . \tag{4.32}$$

Further, the rate of temperature change may be determined upon substituting (4.32) into (4.22) as

$$c\dot{\theta} \;=\; \rho_0 r + \mathrm{Div}(\mathbf{K}\,\mathrm{Grad}\,\theta) + \sum_\alpha(B\theta+f_\alpha)\dot{\xi}_\alpha - \overline{\dot{\mathbf{E}^e\cdot\mathbb{C}\mathbf{A}}}\,\theta \; , \tag{4.33}$$

where Fourier's law is applied by relating the referential flux $\mathbf{q}_0$ to the referential gradient of temperature $\operatorname{Grad}\theta$ according to $\mathbf{q}_0 = -\mathbf{K}\operatorname{Grad}\theta$, in terms of a positive-definite second-order conductivity tensor $\mathbf{K}$.

Forward or reverse transformation is assumed to occur when the thermodynamic driving force f_α conjugate to the martensitic variant with volume fraction ξ_α in the dissipation inequalities $(4.18)_3$ or $(4.21)_3$ reaches a critical value, namely

$$f_\alpha \;=\; \begin{cases} \mathcal{F}_c & \text{(forward transformation)} \\ -\mathcal{F}_c & \text{(reverse transformation)} \end{cases} \;, \tag{4.34}$$

where $\mathcal{F}_c$ is a positive constant, see also [53]. Also, due to the crystal symmetry of the variants, the critical value of thermodynamic driving force is independent of the particular variant. This is a rate-independent transformation law, since the critical value of the driving force is a constant during persistent forward or reverse transformation. It is noted that rate-dependent transformation laws have been proposed for Nitinol to model changes in the thermomechanical response observed at different loading rates, see, *e.g.*, [35, 3]. However, there exists experimental evidence that such changes are principally due to the different temperature evolutions realized in the specimen at different rates of loading, and their direct effect on the transformation of the specimen [31]. This obviates the need for rate-dependent modeling of the transformation laws.

For the proposed model, an expression for the thermodynamic driving force is derived in Appendix A.1 as

$$f_\alpha \;=\; (\mathbf{C}^e\mathbf{S}^e)\cdot\left(\mathbf{H}^t_\alpha\mathbf{F}^{t-1}\right) - B(\theta-\theta_T)\;. \tag{4.35}$$

The model proposed here will be referred to as the "FT" model, when comparing it with other models discussed in the following section.

4.1.4 Comparison to other models

Two alternative models of micromechanically-motivated continuum phase transformation are briefly introduced here and compared to the proposed model.

In the work of Anand and Gurtin [3], the Helmholtz free energy is defined as in (4.29). However, the evolution of the transformation deformation gradient is governed by a rate-type equation of the form

$$\dot{\mathbf{F}}^t \;=\; \left(\sum_\alpha \dot{\xi}_\alpha \mathbf{H}^t_\alpha\right)\mathbf{F}^t\;, \tag{4.36}$$

where the rate of change of the martensite volume fractions is determined by enforcing the conditions (4.34). This constitutive equation is motivated by the theory of crystallographic slip in metals and, unlike the proposed model, is not amenable to a reduction to a parameterized thermo-elastic solid as in (4.19). The stress $\mathbf{S}$ in this model is derived from an

equation identical in form to (4.30), albeit with the definition of the transformation deformation gradient as in (4.36). Also, the thermodynamic force f_α^{AG} for this model is given by

$$f_\alpha^{AG} \;=\; \tau_\alpha^{AG} - \frac{\partial \bar{\Psi}}{\partial \xi_\alpha} \;=\; (\mathbf{C}^e\mathbf{S}^e)\cdot\mathbf{H}_\alpha^t - B(\theta-\theta_T)\;. \tag{4.37}$$

Furthermore, the temperature evolution is governed by (4.33), where the thermodynamic force is given by (4.37).

Another model introduced here is obtained by adding the thermomechanical coupling and the entropic terms to the Helmholtz free energy proposed in Jung *et al.* [43]. This results in

$$\begin{aligned}\Psi \;=\; \hat{\Psi}^J(\mathbf{E},\{\xi_\alpha\},\theta) \;=\; &\frac{1}{2}(\mathbf{E}-\mathbf{E}^t)\cdot\mathbb{C}(\mathbf{E}-\mathbf{E}^t) + B(\theta-\theta_T)\sum_\alpha \xi_\alpha - \\ &(\mathbf{E}-\mathbf{E}^t)\cdot\mathbb{C}\mathbf{A}(\theta-\theta_0) + c\left(\theta-\theta_0-\theta\,\log\left(\frac{\theta}{\theta_0}\right)\right)\;,\end{aligned} \tag{4.38}$$

where the transformation Green-Lagrange strain $\mathbf{E}^t$ is defined as

$$\mathbf{E}^t \;=\; \sum_{\alpha=1}^{nv} \xi_\alpha \mathbf{E}_\alpha^t\;, \tag{4.39}$$

in terms of the respective strains $\mathbf{E}_\alpha^t$ of the habit-plane variants of martensite. The strains $\mathbf{E}_\alpha^t$ are derived from the transformation deformation gradients $\mathbf{F}_\alpha^t$ in (4.3). The stress $\mathbf{S}$ in this model is expressed as Hence the rate of $\mathbf{E}^t$ is given by

$$\dot{\mathbf{E}}^t \;=\; \sum_{\alpha=1}^{nv} \dot{\xi}_\alpha \mathbf{E}_\alpha^t\;. \tag{4.40}$$

$$\mathbf{S} \;=\; \mathbb{C}\left(\mathbf{E}-\mathbf{E}^t-\mathbf{A}(\theta-\theta_0)\right)\;. \tag{4.41}$$

In addition, the thermodynamic force f_α^J takes the form

$$f_\alpha^J \;=\; -\frac{\partial \hat{\Psi}^J}{\partial \xi_\alpha} \;=\; \mathbf{E}_\alpha^t\cdot\mathbf{S} - B(\theta-\theta_T)\;, \tag{4.42}$$

where (4.41) and (4.39) have been used. Now, in analogy to the derivation of (4.33), it can be shown that the evolution of temperature is governed by

$$c\dot{\theta} \;=\; \rho_0 r + \mathrm{Div}(\mathbf{K}\,\mathrm{Grad}\,\theta) + \sum_\alpha \left(B\theta + f_\alpha^J\right)\dot{\xi}_\alpha - \overline{(\mathbf{E}-\mathbf{E}^t)\cdot\mathbb{C}\mathbf{A}}\,\theta\;. \tag{4.43}$$

The second model presented in this section will be referred to as "ET" model for comparison purposes.

Isothermal case

The model proposed in [43], which works for the isothermal case, is presented here as a specialization of (4.38) with $\theta = \theta_0$. The Helmholtz free energy is given here as,

$$\Psi \;=\; \hat{\Psi}(\mathbf{E}, \{\xi_\alpha\}, \theta) \;=\; \frac{1}{2}(\mathbf{E} - \mathbf{E}^t) \cdot \mathbb{C}(\mathbf{E} - \mathbf{E}^t) + B(\theta - \theta_T) \sum_\alpha \xi_\alpha \; . \tag{4.44}$$

Thus the second Piola-Kirchhoff stress in (4.41) reduces here to

$$\mathbf{S} = \mathbb{C}\left(\mathbf{E} - \mathbf{E}^t\right) \; . \tag{4.45}$$

This model has been used to obtain the single-crystal and polycrystal response under quasistatic mechanical loading. Representative simulation results are shown in Chapter 8.

4.2 Incremental solution of the transformation equations

In this section, an incremental method is proposed for the solution of the transformation equations (4.34) subject to the constraint conditions

$$-\,\xi_\alpha \;\leq\; 0 \qquad , \qquad \sum_{\alpha=1}^{nv} \xi_\alpha \;\leq\; 1 \; . \tag{4.46}$$

In this method, all variant volume fractions are assumed to be known at time $t = t_n$ and the forward and reverse transformation equations are solved for the new values of the volume fractions at time $t = t_{n+1}$. The proposed solution method includes an active set component to determine and update the set of potentially active martensite variants in $(t_n, t_{n+1}]$ consistently with the transformation conditions (4.34) and the constraints (4.46). The algorithm developed here is motivated by the work in [90]. However in contrast to their work, the constraints on the volume fractions are satisfied exactly in this algorithm, and their effect on the transformation equations is taken into consideration.

The proposed algorithm is summarized as follows: First, a potentially active set $\mathcal{PA}$ of transforming variants is determined by calculating trial thermodynamic forces $f^{(0)}_{\alpha,n+1}$ from the present state of strain and temperature, and consists of the variants whose forces exceed the critical values in (4.34), namely satisfy $\mid f^{(0)}_{\alpha,n+1} \mid \geq \mathcal{F}_c$. Next, the volume fractions of the potentially active variants are determined from the transformation equations (4.34). These are solved for all variants $\alpha \in \mathcal{PA}$ in either forward transformation (if $f^{(0)}_{\alpha,n+1} \geq \mathcal{F}_c$) or reverse transformation ($f^{(0)}_{\alpha,n+1} \leq -\mathcal{F}_c$). Taking into account (4.35), the transformation equations take the form

$$\left(\mathbf{C}^e_{n+1}\mathbf{S}^e_{n+1}\right) \cdot \left(\mathbf{H}^t_\alpha \mathbf{F}^{t\,-1}_{n+1}\right) - B(\theta_{n+1} - \theta_T) \;=\; \pm\,\mathcal{F}_c \; , \tag{4.47}$$

and are clearly non-linear in $\{\xi_{\alpha,n+1}\}$. The volume fractions are determined iteratively by linearizing (4.47) to

$$\sum_{\beta\in\mathcal{PA}} A_{\alpha\beta}(\Delta\xi_\beta) \;=\; b_\alpha \qquad , \qquad \alpha\in\mathcal{PA}\;, \tag{4.48}$$

and using the Newton-Raphson method. Appendix A.1 contains derivations of explicit expressions for $A_{\alpha\beta}$ and b_α. Note that there is no guarantee that the algebraic system (4.48) possesses a unique solution, hence a solution based on the pseudo-inverse of the square matrix $[A_{\alpha\beta}]$ is generally required. The active set portion of the solution method is completed by verifying whether the changes of volume fractions in $(t_n, t_{n+1}]$ are in the same direction with the corresponding driving forces, namely whether the discrete counterpart of the dissipation in $(4.21)_3$ is variant-wise non-negative for all $\alpha\in\mathcal{PA}$. If not, any offending variants are dropped from $\mathcal{PA}$, and a new system of transformation equations is solved until all remaining variants in $\mathcal{PA}$ are consistent with the preceding discrete dissipation condition. The constraint $(4.46)_2$ is subsequently enforced by scaling the incremental changes of the active variants until it is satisfied. In contrast, violation of $(4.46)_1$ prompts, again, scaling of the preceding incremental changes until the most offending variant satisfies $(4.46)_1$ as an equality, followed by the removal of this variant and a new solution of (4.47). In this manner, the new active variants continue to satisfy the requisite transformation equations. The complete algorithm for the determination of the volume fractions is described in Appendix A.2.

Define next the functions $\hat\Phi^f = \hat\Psi + \sum_{\alpha\in\mathcal{J}^f}\mathcal{F}^c\xi_\alpha$ and $\hat\Phi^r = \hat\Psi - \sum_{\alpha\in\mathcal{J}^r}\mathcal{F}^c\xi_\alpha$, where $\mathcal{J}^f$ and $\mathcal{J}^r$ are the sets of variants in forward and reverse transformation that satisfy $(4.34)_{1,2}$, respectively. For the constitutive model in (4.38), the functions $\hat\Phi^f$ and $\hat\Phi^r$ attain non-unique global minima during forward or reverse transformation at a given strain and temperature. This conclusion can be readily deduced from (4.34) and holds true provided that the elastic modulus $\mathbb{C}$ is constant and the Hessian of $\hat\Phi^f$ and $\hat\Phi^r$ is positive-semidefinite. To ensure an unique solution, a set of six potentially active variants based on the values of their driving forces are pre-selected and $\mathbb{C}_{n+1}$ is chosen to be incrementally constant. The minimization of $\hat\Phi^f$ and $\hat\Phi^r$ is subject to the constraints conditions of the form

$$-\,\xi_\alpha \;\le\; 0 \qquad , \qquad \bar\xi_l - \sum_{\alpha=1}^{nv}\xi_\alpha \;\le\; 0 \qquad , \qquad \sum_{\alpha=1}^{nv}\xi_\alpha - \bar\xi_u \;\le\; 0\;. \tag{4.49}$$

In case of elastic loading/unloading or forward transformation from a state with initial total martensitic volume fraction ξ_{total}, it is clear that $\bar\xi_l = \xi_{total}$ and $\bar\xi_u = 1$. Likewise, in case of elastic loading/unloading or reverse transformation, $\bar\xi_l = 0$ and $\bar\xi_u = \xi_{total}$, The minimization of Φ^f and Φ^r, subject to the inequality constraints (4.49) requires that

$$\frac{\partial\hat\Phi^f}{\partial\xi_\alpha} + \lambda_\alpha + \lambda_l - \lambda_u \;=\; 0 \qquad , \qquad \frac{\partial\hat\Phi^r}{\partial\xi_\alpha} + \lambda_\alpha + \lambda_l - \lambda_u \;=\; 0\;. \tag{4.50}$$

Here, λ_α, $\alpha = 1, 2, \ldots, nv$, λ_l and λ_u are nonnegative-valued Lagrange multipliers intended

to enforce the constraints in (4.49), subject to the Kuhn-Tucker condition

$$\sum_{\alpha=1}^{nv} \lambda_\alpha(-\xi_\alpha) + \lambda_l(\bar{\xi}_l - \sum_{\alpha=1}^{nv} \xi_\alpha) + \lambda_u(\sum_{\alpha=1}^{nv} \xi_\alpha - \bar{\xi}_u) \;=\; 0 \;. \tag{4.51}$$

In particular, taking into account (4.42) and (4.45), the constrained minimization of Φ^f and Φ^r at time $t = t_{n+1}$ leads to the forward and reverse conditions

$$\begin{aligned} \mathbb{C}_{n+1}\big(\mathbf{E}_{n+1} - \mathbf{E}^t_{n+1}\big) \cdot \mathbf{E}^t_\alpha - \big(B(\theta - \theta_T) + \mathcal{F}^c\big) + \lambda_{\alpha,n+1} + \lambda_{l,n+1} - \lambda_{u,n+1} \;&= 0 \;, \\ \mathbb{C}_{n+1}\big(\mathbf{E}_{n+1} - \mathbf{E}^t_{n+1}\big) \cdot \mathbf{E}^t_\alpha - \big(B(\theta - \theta_T) - \mathcal{F}^c\big) + \lambda_{\alpha,n+1} + \lambda_{l,n+1} - \lambda_{u,n+1} \;&= 0 \;, \end{aligned} \tag{4.52}$$

subject to

$$\sum_{\alpha=1}^{nv} \lambda_{\alpha,n+1}(-\xi_{\alpha,n+1}) + \lambda_{l,n+1}(\bar{\xi}_{l,n+1} - \sum_{\alpha=1}^{nv} \xi_{\alpha,n+1}) + \lambda_{u,n+1}(\sum_{\alpha=1}^{nv} \xi_{\alpha,n+1} - \bar{\xi}_{u,n+1}) \;=\; 0 \;. \tag{4.53}$$

see [43] for further details of an algorithmic implementation using an active set strategy.

Chapter 5

Constitutive modeling of B2-R-B19′ phase transformation

Most constitutive models of phase transformations in Nitinol account only for the austenite-martensite transformation and neglect the formation of an intermediate rhombohedral phase (R-phase). Constitutive models of B2-B19′ phase transformation in Nitinol under quasistatic and dynamic mechanical loading conditions were discussed in Chapter 4. It was noted in Section 3.3.3 that the formation and properties of R-phase is critically dependent on the specimen temperature. Further, experiments indicate that R-phase can be stress-induced under room temperature and is responsible for the stress-strain non-linearity in the pre-martensitic zone. Although the plateau of the austenite-R-phase transformation is much narrower and exhibits much smaller hysteresis compared to the austenite-martensite transformation [60], the presence of R-phase influences the transformation along the R-phase-martensite path, thus rendering the formation of different martensite variants dependent on the load path. Further, experimental evidence in [80, 70] and discussions on R-phase in [18] suggest that formation of R-phase and martensite phases from austenite are two competing phase transformations. As a result, phase transformation during a load increment takes place along the path that is most energetically favorable at the current state.

An approach for the constitutive modeling of the combined austenite-R-phase-martensite transformation in single crystals is proposed here, in which the current transformation state is determined for a given history of the same and quasistatic loading conditions. This approach is based on an extension of the model (4.44) - (4.45), which was developed in [43]. Here, the transformation state is determined by minimization of appropriate functionals for forward or reverse transformation along each of the potential transformation paths, thus extending the procedure used in [43] for the (single) austenite-martensite path. However, given the history-dependence, the minimization here is taken to be incremental in nature, as in the case of plasticity and texture evolution in polycrystals, see [68] and [61]. On the implementation front, the algorithmic problem is rendered tractable by allowing phase transformation in each time step only along the single most feasible path.

5.1 Constitutive assumptions

Similar to the constitutive models for B2-B19′ transformation developed in [82, 43] and discussed in Chapter 4, the stress response is viewed as one of a parameterized thermoelastic material, for given values of the volume fractions of the transforming phases. However, here the model has to take into account the austenite-martensite, austenite-R-phase and R-phase-martensite volume fractions, which are denoted by, $\xi_\alpha^{AM_1}$, ξ_β^{AR} and $\xi_\gamma^{RM_2}$, with $\alpha = 1,\dots,nam$, $\beta = 1,\dots,nr$, and $\gamma = 1,\dots,nrm$, where nam, nr and nrm are the total numbers of potential M_1-martensite, R-phase and M_2-martensite variants. A distinction is made between martensite produced from austenite (M_1) and R-phase (M_2), because the two classes of martensites typically involve different variants with different constraints on their evolution.

The R-phase variant volume fractions ξ_α^R, $\alpha = 1,\dots,nr$, are determined by transformation along the austenite-R-phase and the R-phase-martensite paths. These can be additively decomposed into the volume fractions ξ_α^{AR}, $\alpha = 1,\dots,nr$, due to the forward austenite-R-phase transformation and the changes $\Xi_\alpha^{M_2R}$, $\alpha = 1,\dots,nr$, in the R-phase volume fractions due to forward and reverse transformations between the R-phase and the M_2-martensite phase. This decomposition is mathematically expressed as

$$\xi_\alpha^R \;=\; \xi_\alpha^{AR} + \Xi_\alpha^{M_2R} \;. \tag{5.1}$$

The R-phase formed along the austenite-R-phase path is obtained by time-integrating the corresponding rate, which can be defined as

$$\dot{\xi}_\alpha^{AR} = \dot{\xi}_\alpha^R\big|_{\{\xi_\beta^{RM_2}\}=const.} \;, \tag{5.2}$$

where ξ_α^R are assumed to depend continuously on time. While the volume fractions ξ_α^{AR} are always positive, note that $\Xi_\alpha^{M_2R}$ are positive only when the net variant-wise transformation between R-phase and M_2-martensite phase favors the former. Here, $\Xi_\alpha^{M_2R}$ are assumed to be functions of the history of the R-phase and RM_2 transformation and the current volume fraction of M_2-martensite, and can be generally expressed as

$$\Xi_\alpha^{M_2R}(t) \;=\; \hat{\Xi}_\alpha^{M_2R}\Big(\underset{\tau<t}{\mathcal{H}}\big(\{\xi_\beta^R(\tau)\},\{\xi_\gamma^{RM_2}(\tau)\}\big),\xi_\gamma^{RM_2}(t)\Big) \;, \tag{5.3}$$

where $\underset{\tau<t}{\mathcal{H}}(\cdot)$ denotes the history of the variable $(\cdot)$. The set $\mathcal{F}$ of volume fractions of all martensite- and austenite-induced R-phase variants is now defined as

$$\begin{aligned}\mathcal{F} \;&=\; \big\{\{\xi_\alpha^{AM_1}\},\{\xi_\beta^{AR}\},\{\xi_\gamma^{RM_2}\}\big\} \;= \\ &\Big\{(\xi_1^{AM_1},\xi_2^{AM_1},\cdots,\xi_{nam}^{AM_1},\xi_1^{AR},\xi_2^{AR},\cdots,\xi_{nr}^{AR},\xi_1^{RM_2},\xi_2^{RM_2},\cdots,\xi_{nrm}^{RM_2})\Big\} \;.\end{aligned} \tag{5.4}$$

These volume fractions are subject to the constraints

$$\xi_\alpha^{AM_1} \;\geq\; 0 \quad , \quad \xi_\beta^R \;\geq\; 0 \quad , \quad \xi_\gamma^{RM_2} \;\geq\; 0 \tag{5.5}$$

and

$$\sum_{\alpha=1}^{nam} \xi_\alpha^{AM_1} + \sum_{\beta=1}^{nr} \xi_\beta^{R} + \sum_{\gamma=1}^{nrm} \xi_\gamma^{RM_2} \leq 1 \ , \tag{5.6}$$

where ξ_β^R is given by (5.1).

The case of forward R-phase-martensite transformation requires special treatment, because it involves transformation between multiple variants of two phases, in contrast to the austenite-R-phase and the austenite-martensite transformations, where the parent phase is the same single variant phase. As discussed in Section 3.3.3, the R-phase variants do not have one-to-one correspondence with the M_2-martensitic variants formed from R-phase. The rates of change of volume fractions of R-phase and M_2-martensitic variants are subject to the conservation of volume fraction, namely

$$\sum_{\alpha=1}^{nr} \dot{\Xi}_\alpha^{M_2R} + \sum_{\beta=1}^{nrm} \dot{\xi}_\beta^{RM_2} \ = \ 0 \ . \tag{5.7}$$

An additional constraint stems from the fact that the net production of M_2-martensite cannot exceed the net supply of R-phase. This leads to the condition

$$\sum_{\beta=1}^{nrm} \dot{\xi}_\beta^{RM_2} dt \ \leq \ \sum_{\alpha=1}^{nr} \xi_\alpha^{R} + \sum_{\alpha=1}^{nr} \dot{\xi}_\alpha^{AR} dt \ . \tag{5.8}$$

A specific rate-type form of the constitutive law (5.3) is now stipulated to characterize the transformation between individual M_2-martensite variants and R-phase variants, consistently with the preceding constraints. In fact, separate rules are imposed on forward and reverse R-phase-martensite transformations. This is due to the different nature of these two classes of transformations within the proposed model. Indeed, in the forward R-phase-martensite transformation, the rate of $\Xi_\alpha^{M_2R}$ can be generally taken to depend on the rate of the state variables $\xi_\beta^{RM_2}$ and the current volume fractions of the R-phase, as suggested in (5.3). However, in the reverse R-phase-martensite transformation, the same rate can depend only on the rate of the state variables $\xi_\beta^{RM_2}$, since R-phase need not be present, at least at the onset of this transformation.

Based on the preceding observations, it is assumed that when forward R-phase-martensite transformation occurs, the volume fractions of R-phase variants are reduced in proportion to their existing volume fractions. Therefore, the rate of reduction in the volume fraction of R-phase variant α is

$$\dot{\Xi}_\alpha^{M_2R} \ = \ -\frac{\xi_\alpha^R}{\sum_{\alpha=1}^{nr} \xi_\alpha^R} \sum_{\beta=1}^{nrm} \dot{\xi}_\beta^{RM_2} \ . \tag{5.9}$$

Clearly, (5.9) is consistent with the constraint in (5.7). It is also consistent with $(5.5)_2$ in that, when only forward R-phase-martensite transformation occurs, then $\dot{\Xi}_\alpha^{M_2R} = \dot{\xi}_\alpha^R$ and

the R-phase volume fraction at time $t + dt$ is

$$\xi_\alpha^R + \dot{\xi}_\alpha^R dt \;=\; \xi_\alpha^R - \frac{\xi_\alpha^R}{\sum_{\alpha=1}^{nr} \xi_\alpha^R} \sum_{\beta=1}^{nrm} \dot{\xi}_\beta^{RM_2} dt \;\geq\; 0 \;, \tag{5.10}$$

where (5.8) is used.

The reverse R-phase-martensite transformation is only subject to the constraint condition (5.7), since (5.8) holds trivially. In the absence of variant correspondences, one needs to identify the R-phase variants produced from M_2-martensite using alternative means. The approach adopted here is to admit a limited set of nrv potentially active R-phase variants that are equally probable, hence would have equal rates of production. These variants may be chosen using history information (*e.g.*, they may coincide with the R-phase variants present in the latest stage of R-phase generation) or using a kinetics-based criterion (*e.g.*, the magnitude of the current thermodynamic force needed to generate them are equal). In either case, the rate of growth of R-phase variants takes the form

$$\dot{\Xi}_\alpha^{M_2 R} \;=\; -\frac{1}{nrv} \sum_{\beta=1}^{nrm} \dot{\xi}_\beta^{RM_2} \;. \tag{5.11}$$

The constitutive dependencies of the Helmholtz free energy (2.27) are expressed here as

$$\Psi = \hat{\Psi}(\mathbf{E}, \mathcal{F}, \theta; \mathcal{H}) \;. \tag{5.12}$$

While explicit representation of time dependencies is omitted in (5.12), Ψ is assumed to depend on the values of $\mathbf{E}$, $\mathcal{F}$ and θ at the current time t, as well as on the history term $\mathcal{H} = \underset{\tau<t}{\mathcal{H}}(\{\xi_\alpha^R\}, \{\xi_\gamma^{RM_2}\})$ of the R-phase and RM_2 transformation. The fact that the history of R-phase and RM_2 transformation does not affect the instantaneous rate $\dot{\Psi}$ of the Helmholtz free energy, is emphasized by setting $\mathcal{H}$ aside in the argument list of (5.12). The choice of independent variables in (5.12) underlines the fact that $\{\xi_\alpha^R\}$ cannot be viewed as a state variable in addition to $\mathcal{F}$, because its rate is uniquely determined from the rates of $\mathcal{F}$ and from $\mathcal{H}$, as seen from ((5.1)-(5.3)).

It follows from equations (4.8), (2.31) and (2.27) that, during a homothermal (Grad $\theta = 0$) and isothermal ($\dot{\theta} = 0$) superelastic process, the condition

$$\mathbf{S} \cdot \dot{\mathbf{E}} - \dot{\Psi} \;\geq\; 0 \tag{5.13}$$

holds true. Using (5.12) one finds that

$$\left(\mathbf{S} - \frac{\partial \hat{\Psi}}{\partial \mathbf{E}} \right) \cdot \dot{\mathbf{E}} - \sum_{\alpha=1}^{nam} \frac{\partial \hat{\Psi}}{\partial \xi_\alpha^{AM_1}} \dot{\xi}_\alpha^{AM_1} - \sum_{\beta=1}^{nr} \frac{\partial \hat{\Psi}}{\partial \xi_\beta^{AR}} \dot{\xi}_\beta^{AR} - \sum_{\gamma=1}^{nrm} \frac{\partial \hat{\Psi}}{\partial \xi_\gamma^{RM_2}} \dot{\xi}_\gamma^{RM_2} \;\geq\; 0 \;. \tag{5.14}$$

Given that $\mathbf{E}$ may be varied independently from $\xi_\alpha^{AM_1}$, ξ_β^{AR} and $\xi_\gamma^{RM_2}$ due to the existence of elastic processes at all transformation states, the standard Coleman and Noll argument can be applied to equation (5.14), leading to

$$\mathbf{S} \;=\; \frac{\partial \hat{\Psi}}{\partial \mathbf{E}} \tag{5.15}$$

and

$$\dot{D} \;=\; -\sum_{\alpha=1}^{nam} \frac{\partial \hat{\Psi}}{\partial \xi_\alpha^{AM_1}} \dot{\xi}_\alpha^{AM_1} \;-\; \sum_{\beta=1}^{nr} \frac{\partial \hat{\Psi}}{\partial \xi_\beta^{AR}} \dot{\xi}_\beta^{AR} \;-\; \sum_{\gamma=1}^{nrm} \frac{\partial \hat{\Psi}}{\partial \xi_\gamma^{RM_2}} \dot{\xi}_\gamma^{RM_2} \;\geq\; 0 \,. \tag{5.16}$$

Equation (5.16) shows that the dissipation rate $\dot{D}$, defined as the rate of work done by the thermodynamic forces $-\dfrac{\partial \hat{\Psi}}{\partial \xi_\alpha^{AM_1}}$, $-\dfrac{\partial \hat{\Psi}}{\partial \xi_\beta^{AR}}$, and $-\dfrac{\partial \hat{\Psi}}{\partial \xi_\gamma^{RM_2}}$, is non-negative.

Transformation can occur along any potential transformation path $\mathfrak{K}$, where $\mathfrak{K} \in \{AM_1, AR, RM_2\}$. Also $nv(\mathfrak{K})$ will be used to denote the total number of variants along $\mathfrak{K}$-transformation path, namely $nv(AM_1) = nam$, $nv(AR) = nr$ and $nv(RM_2) = nrm$. The transformation of a typical variant α along $\mathfrak{K}$-transformation path occurs when the thermodynamic force $-\dfrac{\partial \hat{\Psi}}{\partial \xi_\alpha^{\mathfrak{K}}}$ acting on the variant reaches a critical value $\mathcal{F}_\alpha^{c,\mathfrak{K}} > 0$, as explained in [53]. Due to the crystal symmetry of the variants, $\mathcal{F}_\alpha^{c,\mathfrak{K}}$ is the same for all variants undergoing transformation along a given transformation path $\mathfrak{K}$. Furthermore, the critical force for reverse transformation is assumed to be the negative of that for forward transformation. Under these assumptions, the forward and reverse transformation conditions are postulated as

$$\begin{aligned} -\frac{\partial \hat{\Psi}}{\partial \xi_\alpha^{\mathfrak{K}}} - \mathcal{F}_\alpha^{c,\mathfrak{K}} &= \; 0 \,, \\ -\frac{\partial \hat{\Psi}}{\partial \xi_\alpha^{\mathfrak{K}}} + \mathcal{F}_\alpha^{c,\mathfrak{K}} &= \; 0 \,. \end{aligned} \tag{5.17}$$

Equation (5.17) implies that along each of the three forward transformation paths, the functional

$$\Phi^{f,\mathfrak{K}} \;=\; \tilde{\Phi}^{f,\mathfrak{K}}(\{\xi_\alpha^{\mathfrak{K}}\}) \;=\; \tilde{\Psi}(\{\xi_\alpha^{\mathfrak{K}}\}) + \sum_{\alpha \in \mathcal{J}^{f,\mathfrak{K}}} \mathcal{F}^{c,\mathfrak{K}} \xi_\alpha^{\mathfrak{K}} \tag{5.18}$$

is minimized during forward transformation for given strain, temperature and transformation history, where $\xi_\alpha^{\mathfrak{K}}$ are the corresponding volume fractions of active variants and $\tilde{\Psi}(\{\xi_\alpha^{\mathfrak{K}}\}) = \hat{\Psi}\big|_{(\mathbf{E},\theta,\mathcal{F}\setminus\{\xi_\alpha^{\mathfrak{K}}\};\mathcal{H})=const}$. Here, $\mathcal{J}^{f,\mathfrak{K}}$ is the set of variants in the forward transformation path $\mathfrak{K}$ that satisfy $(5.17)_1$. A unique minimum exists provided that the Hessian matrix $\dfrac{\partial^2 \tilde{\Phi}^{f,\mathfrak{K}}}{\partial \xi_\alpha^{\mathfrak{K}} \partial \xi_\beta^{\mathfrak{K}}}$ is positive-definite. A general functional that is minimized along any given forward

transformation path can be constructed by including the dissipation potential for all three such paths, and takes the form

$$\Phi^f \;=\; \bar{\Phi}^f(\mathcal{F}) \;=\; \bar{\Psi}(\mathcal{F}) + \sum_{\alpha\in\mathcal{J}^{f,AM_1}} \mathcal{F}^{c,AM_1}\xi_\alpha^{AM_1} + \sum_{\beta\in\mathcal{J}^{f,AR}} \mathcal{F}^{c,AR}\xi_\beta^{AR} + \sum_{\gamma\in\mathcal{J}^{f,RM_2}} \mathcal{F}^{c,RM_2}\xi_\gamma^{RM_2}\,, \quad (5.19)$$

where $\bar{\Psi}(\mathcal{F}) = \hat{\Psi}\big|_{(\mathbf{E},\theta;\mathcal{H})=const}$. A minimum of the above functional may, in general, involve transformation along all three transformation paths.

An analogous procedure may be followed to construct a functional Φ^r for the case of reverse transformation as

$$\Phi^r \;=\; \bar{\Phi}^r(\mathcal{F}) \;=\; \bar{\Psi}(\mathcal{F}) - \sum_{\alpha\in\mathcal{J}^{r,AM_1}} \mathcal{F}^{c,AM_1}\xi_\alpha^{AM_1} - \sum_{\beta\in\mathcal{J}^{r,AR}} \mathcal{F}^{c,AR}\xi_\beta^{AR} - \sum_{\gamma\in\mathcal{J}^{r,RM_2}} \mathcal{F}^{c,RM_2}\xi_\gamma^{RM_2}\,. \quad (5.20)$$

Clearly, owing to the history-dependence of Ψ, the minimization properties of the functionals $\bar{\Phi}^f(\mathcal{F})$ and $\bar{\Phi}^r(\mathcal{F})$ in (5.19) and (5.20) are incremental in nature. This, in effect, implies that the minima of Φ^f and Φ^r at time t are determined for a given history $\mathcal{H} = \underset{\tau<t}{\mathcal{H}}(\{\xi_\alpha^R\},\{\xi_\gamma^{RM_2}\})$ of the R-phase transformation.

5.2 A simple constitutive model

In the case of pure B2-B19′ transformation (identified here as austenite-M_1 martensite transformation), the Helmholtz free energy was given as (4.44). Here, this free energy is restated, with some parameters renamed as,

$$\Psi \;=\; \hat{\Psi}(\mathbf{E},\{\xi_\alpha^{AM_1}\},\theta) \;=\; \frac{1}{2}(\mathbf{E}-\mathbf{E}^t)\cdot\mathbb{C}(\mathbf{E}-\mathbf{E}^t) + B_M(\theta-\theta_T^M)\sum_{\alpha=1}^{nam}\xi_\alpha^{AM_1}\,. \quad (5.21)$$

Here, B_M is a constant chemical energy coefficient and θ_T^M is the thermodynamic equilibrium temperature between the two phases. These constants generally attain a different value for austenite-R-phase pair. Hence, the Helmholtz free energy is generalized to

$$\Psi \;=\; \tilde{\Psi}(\mathbf{E},\mathcal{F},\theta;\mathcal{H}) \;=\; \frac{1}{2}(\mathbf{E}-\mathbf{E}^t)\cdot\mathbb{C}(\mathbf{E}-\mathbf{E}^t) + B_M(\theta-\theta_T^M)\left[\sum_{\alpha=1}^{nam}\xi_\alpha^{AM_1} + \sum_{\gamma=1}^{nrm}\xi_\gamma^{RM_2}\right] + B_R(\theta-\theta_T^R)\sum_{\beta=1}^{nr}\xi_\beta^R\,. \quad (5.22)$$

Here, $\{B_M,\theta_M\}$ and $\{B_R,\theta_R\}$ are the chemical energy coefficient and equilibrium temperature pairs of the martensite phases and the R-phase, respectively. Note that the AM_1 and RM_2 transformations are associated with the same chemical energy coefficient B_M and equilibrium temperature θ_T^M due to the earlier assumption that both transformations involve the

same set of martensite variants. Also, $\mathbf{E}^t$ is the total macroscopic Lagrangian transformation strain that is generalized from (4.39) to depend linearly on the martensitic and R-phase volume fractions, and is given by

$$\mathbf{E}^t \;=\; \sum_{\alpha=1}^{nam} \xi_\alpha^{AM_1}\mathbf{E}_\alpha^{t,AM_1} + \sum_{\beta=1}^{nr} \xi_\beta^{R}\mathbf{E}_\beta^{t,R} + \sum_{\gamma=1}^{nrm} \xi_\gamma^{RM_2}\mathbf{E}_\gamma^{t,RM_2} \;. \tag{5.23}$$

Setting $\mathfrak{L} \in \{AM_1, R, RM_2\}$, the variant transformation strains $\mathbf{E}_\alpha^{t,\mathfrak{L}}$ relative to the (common) austenite phase are defined as

$$\mathbf{E}_\alpha^{t,\mathfrak{L}} \;=\; \frac{1}{2}\left(\mathbf{b}_\alpha^{\mathfrak{L}} \otimes \mathbf{m}_\alpha^{\mathfrak{L}} + \mathbf{m}_\alpha^{\mathfrak{L}} \otimes \mathbf{b}_\alpha^{\mathfrak{L}} + (\mathbf{b}_\alpha^{\mathfrak{L}} \cdot \mathbf{b}_\alpha^{\mathfrak{L}})\mathbf{m}_\alpha^{\mathfrak{L}} \otimes \mathbf{m}_\alpha^{\mathfrak{L}}\right) \;, \tag{5.24}$$

in terms of the phase-dependent unit outward normal $\mathbf{m}_\alpha^{\mathfrak{L}}$ to the habit plane and the transformation displacement $\mathbf{b}_\alpha^{\mathfrak{L}}$. It should be noted that the R-phase variants generated from austenite or M_2-martensite have the same transformation strains, denoted by $\mathbf{E}_\alpha^{t,R}$. Also, given that the R-phase is obtained by a small distortion of cubic austenite lattice, the elastic constants of the R-phase are assumed to be coincident to those of the austenite phase. Adopting the rule of mixtures similar to the case of AM_1 transformation (4.28), this implies that the fourth-order elasticity modulus $\mathbb{C}$ in (5.22) can be approximately written as

$$\mathbb{C} \;=\; \left(1 - \sum_{\alpha=1}^{nam} \xi_\alpha^{AM_1} - \sum_{\beta=1}^{nrm} \xi_\beta^{RM_2}\right)\mathbb{C}_a + \left(\sum_{\alpha=1}^{nam} \xi_\alpha^{AM_1} + \sum_{\beta=1}^{nrm} \xi_\beta^{RM_2}\right)\mathbb{C}_m \;, \tag{5.25}$$

in terms of the respective elasticity moduli $\mathbb{C}_a$ and $\mathbb{C}_m$ of the austenite and martensite phases.

The interaction energy among the different martensite or R-phase variants is neglected in the Helmholtz free energy (5.22), since it was seen in our own experiments that it does not contribute substantially to the overall stress response [60]. Likewise, no pure thermal energy term is included, because interest is focused on slow loading processes, which result in small variations of the ambient temperature. Lastly, no thermomechanical coupling term is included, because its effect is secondary for the given temperature and deformation ranges.

Using equations (5.15) and (5.22), the second Piola-Kirchhoff stress for this model is given by

$$\mathbf{S} \;=\; \mathbb{C}\big(\mathbf{E} - \mathbf{E}^t\big) \;. \tag{5.26}$$

Likewise, equation (5.22) implies that equation $(5.17)_1$ for the forward austenite-martensite and austenite-R-phase transformations can be rewritten as

$$\mathbb{C}(\mathbf{E} - \mathbf{E}^t) \cdot \mathbf{E}_\alpha^{t,AM_1} - \big(B_M(\theta - \theta_T^M) + \mathcal{F}^{c,AM_1}\big) = 0 \;, \tag{5.27}$$

and

$$\mathbb{C}(\mathbf{E} - \mathbf{E}^t) \cdot \mathbf{E}_\beta^{t,R} - \big(B_R(\theta - \theta_T^R) + \mathcal{F}^{c,AR}\big) = 0 \;, \tag{5.28}$$

respectively. In the derivation of (5.28), use is also made of (5.1) and (5.3).

The critical driving force $\mathcal{F}^{c,RM_2}$ on the martensite variants during transformation along the RM_2 path is taken to be

$$\mathcal{F}^{c,RM_2} = \mathcal{F}^{c,AM_1} - \mathcal{F}^{c,AR} \ , \tag{5.29}$$

reflecting the relative magnitude of the resistance to RM_2 transformation, as compared to the AM_1 and AR transformations. Taking into account (5.22) and $(5.17)_1$ again, it follows that for forward R-phase-martensite transformation

$$\begin{aligned}\big[\mathbf{E}_\alpha^{t,RM_2} + \sum_{\beta=1}^{nr} \mathbf{E}_\beta^{t,R} \frac{\partial \hat{\Xi}_\beta^{M_2R}}{\partial \xi_\alpha^{RM_2}}\big] \cdot \mathbb{C}(\mathbf{E} - \mathbf{E}^t) \\ - \big(B_M(\theta - \theta_T^M) + \mathcal{F}^{c,AM_1} + B_R(\theta - \theta_T^R) \sum_{\beta=1}^{nr} \frac{\partial \Xi_\beta^{M_2R}}{\partial \xi_\alpha^{RM_2}} - \mathcal{F}^{c,AR}\big) = 0 \ ,\end{aligned} \tag{5.30}$$

where (5.29) has been used. Appealing to (5.7) and assuming continuity of the functions $\hat{\Xi}_\alpha^{M_2R}$ of equation (5.3) both in time and in the volume fractions $\xi_\alpha^{RM_2}$, it is immediately seen that

$$\sum_{\beta=1}^{nr} \frac{\partial \Xi_\beta^{M_2R}}{\partial \xi_\alpha^{RM_2}} \ = \ -1 \ , \tag{5.31}$$

therefore (5.30) reduces to

$$\begin{aligned}\big[\mathbf{E}_\alpha^{t,RM_2} + \sum_{\beta=1}^{nr} \mathbf{E}_\beta^{t,R} \frac{\partial \hat{\Xi}_\beta^{M_2R}}{\partial \xi_\alpha^{RM_2}}\big] \cdot \mathbb{C}(\mathbf{E} - \mathbf{E}^t) \\ - \Big(B_M(\theta - \theta_T^M) + \mathcal{F}^{c,AM_1} - B_R(\theta - \theta_T^R) - \mathcal{F}^{c,AR}\Big) \ = \ 0 \ .\end{aligned} \tag{5.32}$$

Analogous expressions hold for the reverse transformation conditions $(5.17)_2$, with $\mathcal{F}^{c,\mathfrak{K}}$ being replaced by $-\mathcal{F}^{c,\mathfrak{K}}$. For details of the algorithmic implementation, please see [77].

Chapter 6

Finite element framework

A body undergoing change of thermomechanical state under the application of thermal and mechanical boundary conditions follows the balance laws discussed in Section 2.1.3. These balance laws are usually in the form of non-linear partial differential equations in terms of displacement and temperature after applying the constitutive relations which relate stress and heat flux to the foregoing variables. Finite element method is usually employed to numerically solve this analytically intractable problem. This method involves integrating the equations in local form (also known as Euler-Lagrange equations or strong form), over either the referential or spatial domain of the body along with suitable chosen test functions. This domain is then discretized into sub-domains known as elements and the integral equations are evaluated piecewise over these elements. This results in a system of non-linear algebraic equations which could be dependent on or independent of time. Various numerical schemes may be subsequently employed to solve these algebraic equations.

6.1 Weak form for mechanical IBVP

Suppose, that the body occupies the region $\mathcal{R}_0$ in the reference configuration. Let its boundary $\partial\mathcal{R}_0$ be continuously differentiable and orientable with outward normal $\mathbf{N}$. It can further be decomposed into the sets $\Gamma^m_{u,0}$ and $\Gamma^m_{p,0}$ such that

$$\partial\mathcal{R}_0 = \overline{\Gamma^m_{u,0} \cup \Gamma^m_{p,0}} \,, \tag{6.1}$$

where the overbar denotes closure and the superscript "m" stands for the mechanical problem. The time interval of interest is given by $\mathcal{I} = (t_0,\ T]$. Consider an initial/boundary-value

problem (IBVP) for this body with unknown displacements given by

$$\begin{aligned} \operatorname{Div}\mathbf{P}(\mathbf{X},t) \;+\; \rho_0\mathbf{b}(\mathbf{X},t) &= \rho_0\mathbf{a}(\mathbf{X},t) && \text{in } \mathcal{R}_0 \;, \\ \mathbf{u}(\mathbf{X},t) &= \bar{\mathbf{u}}(\mathbf{X},t) && \text{on } \Gamma^m_{u,0} \;, \\ \mathbf{P}(\mathbf{X},t)\mathbf{N} &= \bar{\mathbf{p}}(\mathbf{X},t) && \text{on } \Gamma^m_{p,0} \;, \\ \mathbf{u}(\mathbf{X},t_0) &= \mathbf{0} && \text{in } \mathcal{R}_0 \;, \\ \dot{\mathbf{u}}(\mathbf{X},t_0) &= \bar{\mathbf{v}}_0(\mathbf{X}) && \text{in } \mathcal{R}_0 \;. \end{aligned} \tag{6.2}$$

Here, $\bar{\mathbf{u}}(\mathbf{X},t)$ is the prescribed displacement on $\Gamma^m_{u,0}$ also known as the Dirichlet boundary condition, $\bar{\mathbf{p}}(\mathbf{X},t)$ is the prescribed tractions on $\Gamma^m_{p,0}$ also known as the Neumann boundary condition, and $\bar{\mathbf{v}}_0(\mathbf{X})$ is the initial velocity of the body. For a Galerkin formulation, appropriate function spaces need to be defined. The space of admissible displacements is defined as

$$\begin{aligned} \mathcal{U} = \{\mathbf{u} \mid \mathbf{u} \in H^1(\mathcal{R}_0 \times \mathcal{I}) \;,\; \mathbf{u}(\mathbf{X},t) = \bar{\mathbf{u}}(\mathbf{X},t) \text{ on } \Gamma^m_{u,0} \times \mathcal{I} \;,\; \mathbf{u}(\mathbf{X},t_0) = \mathbf{0} \text{ in } \mathcal{R}_0 \;, \\ \dot{\mathbf{u}}(\mathbf{X},t_0) = \bar{\mathbf{v}}_0(\mathbf{X}) \text{ in } \mathcal{R}_0\} \;. \end{aligned} \tag{6.3}$$

The space of admissible test functions are given by

$$\mathcal{W} = \{\mathbf{w} \mid \mathbf{w} \in H^1(\mathcal{R}_0 \times \mathcal{I}) \;,\; \mathbf{w}(\mathbf{X},t) = \mathbf{0} \text{ on } \Gamma^m_{u,0} \times \mathcal{I} \;\} \;. \tag{6.4}$$

To construct the weak form, initially the weighted residual is written for $(6.2)_1$ as

$$\int_{\mathcal{R}_0} \mathbf{w} \cdot \rho_0 \ddot{\mathbf{u}} \; dV = \int_{\mathcal{R}_0} \mathbf{w} \cdot \operatorname{Div}\mathbf{P} \; dV + \int_{\mathcal{R}_0} \mathbf{w} \cdot \rho_0\mathbf{b} \; dV \;, \tag{6.5}$$

since $\mathbf{a} = \ddot{\mathbf{u}}$, where the superposed "double-dot" denotes second-derivative with respect to time.

Using integration by parts and the divergence theorem, the first term on right-hand side of above equation can be written as

$$\int_{\mathcal{R}_0} \mathbf{w} \cdot \operatorname{Div}\mathbf{P} \; dV = \int_{\Gamma^m_{p,0}} \mathbf{w} \cdot \bar{\mathbf{p}} \; dA - \int_{\mathcal{R}_0} \operatorname{Grad}(\mathbf{w}) \cdot \mathbf{P} \; dV \;, \tag{6.6}$$

where (6.4), (6.3) and $(6.2)_3$ have been used. Substituting the above relation in (6.5), the weak form for the problem (6.2) can be posed in the following form. Find displacement field $\mathbf{u} \in \mathcal{U}$, such that for all $\mathbf{w} \in \mathcal{W}$,

$$\int_{\mathcal{R}_0} \mathbf{w} \cdot \rho_0 \ddot{\mathbf{u}} \; dV + \int_{\mathcal{R}_0} \operatorname{Grad}(\mathbf{w}) \cdot \mathbf{P} \; dV = \int_{\Gamma^m_{p,0}} \mathbf{w} \cdot \bar{\mathbf{p}} \; dA + \int_{\mathcal{R}_0} \mathbf{w} \cdot \rho_0\mathbf{b} \; dV \;. \tag{6.7}$$

Since the Dirichlet boundary conditions do not explicitly appear in the weak form of the mechanical IBVP, these conditions are satisfied (strongly) *a priori* by choice of admissible displacements (6.3). On the other hand, the Neumann boundary conditions are enforced weakly through (6.7).

6.2 Finite element formulation for the mechanical IBVP

In the finite element method, the domain $\mathcal{R}_0$ is discretized into a set of element subregions, so that the mechanical displacement field $\mathbf{u}$ and the independent variations $\mathbf{w}$ are obtained over each element e through interpolation between the nodal values as

$$\begin{aligned} \mathbf{u}^e(\mathbf{X},t) &= \sum_{I=1}^{nen} \bar{N}^{I,e}(\mathbf{X})\mathbf{u}^{I,e}(t) \ , \\ \mathbf{w}^e(\mathbf{X},t) &= \sum_{I=1}^{nen} \bar{N}^{I,e}(\mathbf{X})\mathbf{w}^{I,e}(t) \ , \end{aligned} \tag{6.8}$$

where nen is the number of nodes of a typical element and $\bar{N}^{I,e}$ is the Lagrangian shape function at node I. The usual procedure is to formulate the interpolations in an isoparametric space given by $\square = [-1,1] \times \cdots^{ndim} \times [-1,1]$, which are then mapped to the physical space using the relation

$$\boldsymbol{\xi} \in \square \rightarrow \mathbf{X}^e = \sum_{I=1}^{nen} N^{I,e}(\boldsymbol{\xi})\mathbf{X}^{I,e} \ , \tag{6.9}$$

where $N^{I,e}$ are isoparametric Lagrangian shape functions at node I. Using the above mapping, the interpolations over each element can be done in isoparametric space instead as

$$\begin{aligned} \mathbf{u}^e(\boldsymbol{\xi},t) &= \sum_{I=1}^{nen} N^{I,e}(\boldsymbol{\xi})\mathbf{u}^{I,e}(t) \ , \\ \mathbf{w}^e(\boldsymbol{\xi},t) &= \sum_{I=1}^{nen} N^{I,e}(\boldsymbol{\xi})\mathbf{w}^{I,e}(t) \ . \end{aligned} \tag{6.10}$$

In equations that follow, the matrices $[N^e] = [N^{1,e}\mathbf{I} \quad N^{2,e}\mathbf{I} \quad \cdots \quad N^{nen,e}\mathbf{I}]$, $[u^e] = [\mathbf{u}^{1,e} \quad \mathbf{u}^{2,e} \quad \cdots \quad \mathbf{u}^{nen,e}]^T$ and $[w^e] = [\mathbf{w}^{1,e} \quad \mathbf{w}^{2,e} \quad \cdots \quad \mathbf{w}^{nen,e}]^T$ will be used. It may be noted that the gradient of quantities with respect of physical coordinates in the weak form, may be transformed to those with respect to isoparametric coordinates through the Jacobian of the mapping (6.9), see Chapter 3 in [42]. Subsequently, the weak form integral over each element can be expressed in matrix notation as

$$\begin{aligned} [w^e]^T \Bigg[\left(\int_{\mathcal{R}_0^e} \rho_0 [N^e]^T [N^e] \ dV \right) [\ddot{u}^e] + \int_{\mathcal{R}_0^e} [B^e]^T [P] \ dV \\ - \int_{\Gamma_{p,0}^{m,e}} [N^e]^T [\bar{p}] \ dA - \int_{\mathcal{R}_0^e} \rho_0 [N^e]^T [b] \ dV \Bigg] = 0 \ , \end{aligned} \tag{6.11}$$

where the matrix $[B^e]$ is derived from the expression

$$\text{Grad}(\mathbf{u}(\boldsymbol{\xi},t)) = \sum_{I=1}^{nen} \mathbf{u}^{I,e}(t) \otimes \text{Grad}(N^{I,e}(\boldsymbol{\xi})) = \sum_{I=1}^{nen} \mathbf{B}^{I,e}(\boldsymbol{\xi})\mathbf{u}^{I,e}(t) \ = [B^e][u^e]. \tag{6.12}$$

It can be shown for the three-dimensional case that $[B^e] = \begin{bmatrix}[B^{1,e}] & [B^{2,e}] & \cdots & [B^{nen,e}]\end{bmatrix}$ with

$$[B^{I,e}] = \begin{bmatrix} N^{I,e}_{,1} & 0 & 0 & N^{I,e}_{,2} & 0 & 0 & 0 & N^{I,e}_{,3} & 0 \\ 0 & N^{I,e}_{,2} & 0 & 0 & N^{I,e}_{,1} & N^{I,e}_{,3} & 0 & 0 & 0 \\ 0 & 0 & N^{I,e}_{,3} & 0 & 0 & 0 & N^{I,e}_{,2} & 0 & N^{I,e}_{,1} \end{bmatrix}^T$$

and $N^{I,e}_{,A} = \dfrac{\partial N^{I,e}}{\partial X_A}$. Appealing to the arbitrariness of $[w^e]$, the element residual vector is deduced as

$$[r^e] = [M^e][\ddot{u}^e] + [R^e] - [f^e] - [f^e_i] = [0] \ , \tag{6.13}$$

where $[f^e_i]$ is the internal traction over the element boundary whose contribution vanishes after assembling over all elements. In above,

$$\begin{aligned} [M^e] &= \int_{\mathcal{R}^e_0} \rho_0 [N^e]^T [N^e] \ dV \ , \\ [R^e] &= \int_{\mathcal{R}^e_0} [B^e]^T [P] \ dV \ , \\ [f^e] &= \int_{\Gamma^{m,e}_{p,0}} [N^e]^T [\bar{p}] \ dA + \int_{\mathcal{R}^e_0} \rho_0 [N^e]^T [b] \ dV \ . \end{aligned} \tag{6.14}$$

In above, $[M^e]$ is referred to as the element mass matrix, $[R^e]$ is the element stress-divergence vector and $[f^e]$ is the element force vector. The global residual is obtained by assembling the element residuals $[r^e]$ through application of the assembly operator $\mathbb{A}$, see Section 1.14 in [42]. This can be symbolically written as

$$[r] = \mathbb{A}_{e=1}^{numel}[r^e] = [M][\ddot{u}] + [R] - [f] = [0] \ , \tag{6.15}$$

where $\mathbb{A}_{e=1}^{numel}[f^e_i] = [0]$. Here, $[M]$, $[R]$ and $[f]$ are the global mass matrix, global stress-divergence vector and global force vector respectively. Further $\mathcal{R}_0$ is discretized into *numel* number of elements.

6.2.1 Solving the transient non-linear problem

Equations in (6.15) are a system of coupled ordinary differential equations with respect to time. The solution of these equations usually addressed by discretizing the time dimension

into finite intervals and solving the problem incrementally at the discrete time instances. Specifically, if the time instances are $t = t_0, t_1, \cdots, t_n, t_{n+1}, \cdots, t_N$, the residual at time t_{n+1} may be written as

$$[r_{n+1}] = [M][\ddot{u}_{n+1}] + [R(u_{n+1})] - [f_{n+1}] = [0] \ . \tag{6.16}$$

The non-linearity with respect to the displacement variable arises due to the stress-divergence term $[R(u_{n+1})]$. To solve the non-linear equation after resolving it in time, a Newton-Raphson iterative solution procedure is employed. In what follows, the subscript $(n+1)$ will be dropped for convenience. This procedure solves the residual equations

$$\mathcal{F}[u] = [M][\ddot{u}] + [R(u)] - [f] = [0] \ , \tag{6.17}$$

at an iteration k by Taylor expanding the functional up to its first order term, so that

$$\mathcal{F}[u^{(k)} + \Delta u^{(k)}] \approx \mathcal{F}[u^{(k)}] + D\mathcal{F}[u^{(k)}, \Delta u^{(k)}] \ = [0] \ . \tag{6.18}$$

In above $D\mathcal{F}[u^{(k)}, \Delta u^{(k)}]$ is the Gâteaux derivative of $\mathcal{F}[u]$ at $u^{(k)}$ in the direction $\Delta u^{(k)}$. It is also referred to as the linearization of $\mathcal{F}[u^{(k)}]$. The above iterative procedure is continued until the problem converges, i.e. (6.17) is satisfied to a required tolerance for a typical time instance t_{n+1} [8]. The stopping criterion could be set either in terms of an appropriate norm of the residual vector $\mathcal{F}[u^{(k)}]$, or in terms of an energy norm of the form $E^{(k)} = \left| \left[\Delta u^{(k)}\right]^T \left[\mathcal{F}[u^{(k)}]\right] \right|$. In the finite element program FEAP [87], the stopping criterion can be chosen to be either $\left|\left|\mathcal{F}[u^{(k)}]\right|\right|_\infty < tol$ or $\left|\dfrac{E^{(k)}}{E^{(0)}}\right| < tol$, where tol is a specified tolerance. The Gâteaux derivative of the inertia term in (6.7) is given by

$$D\left(\int_{\mathcal{R}_0} \mathbf{w} \cdot \rho_0 \ddot{\mathbf{u}} \ dV\right)[\mathbf{u}^{(k)}, \Delta\mathbf{u}^{(k)}] = \int_{\mathcal{R}_0} \mathbf{w} \cdot \rho_0 \Delta\ddot{\mathbf{u}}^{(k)} \ dV \ . \tag{6.19}$$

The Gâteaux derivative of the stress-divergence term in (6.7) is given by

$$D\left(\int_{\mathcal{R}_0} \text{Grad}\, \mathbf{w} \cdot \mathbf{P} \ dV\right)[\mathbf{u}^{(k)}, \Delta\mathbf{u}^{(k)}] = \int_{\mathcal{R}_0} \text{Grad}(\mathbf{w}) \cdot \frac{\partial \mathbf{P}}{\partial \mathbf{F}} \ \text{Grad}\, \Delta\mathbf{u}^{(k)} \ dV \ , \tag{6.20}$$

where $\mathbf{H} = \dfrac{\partial \mathbf{P}}{\partial \mathbf{F}}$ is the fourth-order tensor representing referential tangent modulus of the material and $\mathbf{F} = \mathbf{I} + \text{Grad}\, \mathbf{u}$ is used. This is usually decomposed into two parts, using the relation $\mathbf{P} = \mathbf{FS}$ as

$$\frac{\partial P_{iA}}{\partial F_{jB}} = F_{iC} \frac{\partial S_{CA}}{\partial E_{BD}} F_{jD} + \delta_{ij} S_{BA} \ . \tag{6.21}$$

In order to attain convergence, the Newton-Raphson method solves for (6.18) which can be written at iteration k in expanded form using (6.21) as

$$\int_{\mathcal{R}_0} \mathbf{w}\cdot\rho_0\ddot{\mathbf{u}}^{(k)}\,dV + \int_{\mathcal{R}_0} \operatorname{Grad}\mathbf{w}\cdot\mathbf{P}^{(k)}\,dV - \int_{\Gamma^m_{p,0}} \mathbf{w}\cdot\bar{\mathbf{p}}^{(k)}\,dA - \int_{\mathcal{R}_0} \mathbf{w}\cdot\rho_0\mathbf{b}\,dV + \int_{\mathcal{R}_0} \mathbf{w}\cdot\rho_0\Delta\ddot{\mathbf{u}}^{(k)}\,dV + \int_{\mathcal{R}_0} \left(\mathbf{F}^{(k),T}\operatorname{Grad}\mathbf{w}\right)\cdot\frac{\partial\mathbf{S}^{(k)}}{\partial\mathbf{E}^{(k)}}\left(\left(\operatorname{Grad}\Delta\mathbf{u}^{(k)}\right)^T\mathbf{F}^{(k)}\right)dV + \int_{\mathcal{R}_0} \operatorname{Grad}\mathbf{w}\cdot\left(\operatorname{Grad}\Delta\mathbf{u}^{(k)}\mathbf{S}^{(k)}\right) = 0\ , \quad (6.22)$$

where the last two terms give rise to the material stiffness and the geometric stiffness terms in the stiffness matrix respectively. A discrete time integration algorithm like the Newmark method is used to express the acceleration and velocity terms (if present) and their increments in terms of displacements and its increments respectively. The Newmark method involves the equations

$$\begin{aligned}\mathbf{u}_{n+1} &= \mathbf{u}_n + \dot{\mathbf{u}}_n\Delta t_n + \frac{1}{2}[(1-2\beta)\ddot{\mathbf{u}}_n + 2\beta\ddot{\mathbf{u}}_{n+1}]\Delta t_n^2\ , \qquad \text{and}\\ \dot{\mathbf{u}}_{n+1} &= \dot{\mathbf{u}}_n + [(1-\gamma)\ddot{\mathbf{u}}_n + \gamma\ddot{\mathbf{u}}_{n+1}]\Delta t_n\ ,\end{aligned} \quad (6.23)$$

where $\Delta t_n = t_{n+1} - t_n$ and $0 \le \beta \le \frac{1}{2}$ and $0 \le \gamma \le 1$ are numerical parameters that control the stability and numerical dissipation of the solution, respectively. Equation $(6.23)_1$ can be restated in the form

$$\ddot{\mathbf{u}}_{n+1} = \frac{1}{\beta\Delta t_n^2}[\mathbf{u}_{n+1} - \mathbf{u}_n - \dot{\mathbf{u}}_n\Delta t_n] - \frac{1-2\beta}{2\beta}\ddot{\mathbf{u}}_n\ . \quad (6.24)$$

At time t_{n+1} and iteration k of the Newton-Raphson method the required increments are obtained from (6.24) and $(6.23)_2$ as

$$\begin{aligned}\Delta\ddot{\mathbf{u}}^{(k)}_{n+1} &= \left(\frac{1}{\beta\Delta t_n^2}\right)\Delta\mathbf{u}^{(k)}_{n+1} = c_1\,\Delta\mathbf{u}^{(k)}_{n+1} \qquad \text{and}\\ \Delta\dot{\mathbf{u}}^{(k)}_{n+1} &= \left(\frac{\gamma}{\beta\Delta t_n}\right)\Delta\mathbf{u}^{(k)}_{n+1} = c_2\,\Delta\mathbf{u}^{(k)}_{n+1}\ .\end{aligned} \quad (6.25)$$

Substituting above relations in (6.22), and using the finite element interpolations (6.10) and (6.12), the incremental equation for solving $[\Delta u^{(k)}_{n+1}]$ in order to satisfy (6.18) is expressed as

$$[w^e]^T\Big[[M][\ddot{u}^{(k)}] + [R(u^{(k)})] - [f] + \big(c_1[M] + [K]\big)[\Delta u^{(k)}]\Big] = [0]\ , \quad (6.26)$$

where $[K] = \mathbb{A}_{e=1}^{numel}\left(\int_{\mathcal{R}_0^e}[B^e]^T[H][B^e]\,dV\right)$.

6.3 Weak form for thermomechanical IBVP

The finite element formulation of the coupled thermomechanical problem requires setting up the weak form for the energy equation in addition to the momentum equations discussed in Section 6.2. Suppose that for the thermal problem, the boundary $\partial\mathcal{R}^0$ can be decomposed into the disjoint sets $\Gamma^t_{u,0}$ and $\Gamma^t_{p,0}$ where the Dirichlet and Neumann boundary conditions are imposed respectively, such that

$$\partial\mathcal{R}_0 = \overline{\Gamma^t_{u,0} \cup \Gamma^t_{p,0}} \ . \tag{6.27}$$

where the superscript "t" stands for the thermal problem. THe IBVP can be stated based on the energy equation for the "FT" model (4.33) as follows:

$$\begin{aligned} \rho_0 r + \mathrm{Div}(\mathbf{K}\,\mathrm{Grad}\,\theta) + \textstyle\sum_\alpha (B\theta + f_\alpha)\dot{\xi}_\alpha - \overline{\dot{\mathbf{E}^e \cdot \mathbb{C}\mathbf{A}}}\,\theta &= c\dot{\theta} && \text{in } \mathcal{R}_0 \ , \\ \theta(\mathbf{X},t) &= \bar{\theta}(\mathbf{X},t) && \text{on } \Gamma^t_{u,0} \ , \\ \mathbf{q}(\mathbf{X},t)\cdot\mathbf{N} &= \bar{h}(\mathbf{X},t) && \text{on } \Gamma^t_{p,0} \ , \\ \theta(\mathbf{X},t_0) &= \theta_0 && \text{in } \mathcal{R}_0 \ . \end{aligned} \tag{6.28}$$

Here $\bar{\theta}(\mathbf{X},\ t)$ is the prescribed temperature on $\Gamma^t_{u,0}$, $\bar{h}$ is the prescribed normal heat flux on $\Gamma^t_{p,0}$ and θ_0 is the initial temperature of the body. The space of admissible temperatures is defined as

$$\mathcal{T} = \{\theta \mid \theta \in H^1(\mathcal{R}_0 \times \mathcal{I}) \ ,\ \theta(\mathbf{X},t) = \bar{\theta}(\mathbf{X},t) \text{ on } \Gamma^t_{u,0} \times \mathcal{I} \ ,\ \theta(\mathbf{X},t_0) = \theta_0 \text{ in } \mathcal{R}_0\} \ . \tag{6.29}$$

The space of admissible test functions are given by

$$\mathcal{W}_t = \{w \mid w \in H^1(\mathcal{R}_0 \times \mathcal{I}) \ ,\ w(\mathbf{X},t) = \mathbf{0} \text{ on } \Gamma^t_{u,0} \times \mathcal{I} \ \} \ . \tag{6.30}$$

Thus, the weak form for the "FT" model is posed in the following form. Find temperature field $\theta \in \mathcal{T}$, such that for all $w \in \mathcal{W}_t$,

$$\begin{aligned} \int_{\mathcal{R}_0} w\ c\ \dot{\theta}\, dV + \int_{\mathcal{R}_0} \mathrm{Grad}\, w \cdot \mathbf{K}\,\mathrm{Grad}\,\theta\, dV + \int_{\mathcal{R}_0} w\ \overline{\dot{\mathbf{E}^e \cdot \mathbb{C}\mathbf{A}}}\ \theta\, dV \\ - \int_{\mathcal{R}_0} w\ \sum_\alpha \left[\left(B\theta_T + (\mathbf{C}^e\mathbf{S}^e) \cdot \left(\mathbf{H}^t_\alpha \mathbf{F}^{t-1} \right) \right) \dot{\xi}_\alpha \right] dV \ = \\ \int_{\mathcal{R}_0} w\ \rho_0 r\, dV - \int_{\Gamma^t_{p,0}} w\bar{h}\, dA \ , \end{aligned} \tag{6.31}$$

where $\bar{h}$ is the prescribed heat flux on $\Gamma^t_{p,0}$. Also, the last term of the left-hand side is obtained by substituting the expression for the thermodynamic force f_α from (4.35).

Similarly, for the "ET" model, where the energy equation is given as (4.43) instead of (6.28), the weak form is stated as: Find temperature field $\theta \in \mathcal{T}$, such that for all $w \in \mathcal{W}_t$,

$$\int_{\mathcal{R}_0} wc\dot{\theta}\, dV + \int_{\mathcal{R}_0} \operatorname{Grad} w \cdot \mathbf{K} \operatorname{Grad} \theta\, dV + \int_{\mathcal{R}_0} w\overline{(\dot{\mathbf{E}} - \dot{\mathbf{E}}^t) \cdot \mathbb{C}\mathbf{A}}\theta\, dV - \int_{\mathcal{R}_0} w \sum_{\alpha} \left[\left(B\theta_T + \mathbf{E}^t_\alpha \cdot \mathbf{S} \right) \dot{\xi}_\alpha \right] dV = \int_{\mathcal{R}_0} w\, \rho_0 r\, dV - \int_{\Gamma^t_{p,0}} w\bar{h}\, dA\ , \quad (6.32)$$

where the last term of the left-hand side is obtained by substituting the expression for the thermodynamic force f_α (4.42).

The residual and tangent terms for the preceding equations are derived henceforth. Note that in order to simplify the computation of tangents, the transformation deformation gradient and the homogenized elastic modulus are evaluated approximately in terms of the volume fractions of previous time-step. Indeed, recalling (4.4) and (4.28), it is assumed that

$$\mathbf{F}^t_{n+1} \doteq \mathbf{I} + \sum_{\alpha=1}^{nv} \xi_{\alpha,n}\, \mathbf{H}^t_\alpha\ , \quad (6.33)$$

and

$$\mathbb{C}_{n+1} \doteq \left[(1 - \sum_{\alpha=1}^{nv} \xi_{\alpha,n})\mathbb{C}_a + \sum_{\alpha=1}^{nv} \xi_{\alpha,n}\mathbb{C}_m \right] . \quad (6.34)$$

These explicit approximations induce an error in the solution of the governing equations that can be controlled by the size of the time-step.

6.4 Finite element formulation for the thermomechanical IBVP

In this work, a monolithic finite element formulation is employed to solve the momentum and energy equations using a Newton-Raphson scheme, while selectively ignoring some of the weak couplings in the governing equations in order to simplify the consistent algorithmic tangents. The finite element interpolation for temperature and the variations w over each element are given in a way similar to the mechanical problem as,

$$\begin{aligned} \theta(\boldsymbol{\xi}, t) &= \sum_{I=1}^{nen} N^{I,e}(\boldsymbol{\xi})\theta^{I,e}(t) \\ w(\boldsymbol{\xi}, t) &= \sum_{I=1}^{nen} N^{I,e}(\boldsymbol{\xi})w^{I,e}(t)\ . \end{aligned} \quad (6.35)$$

In the remainder of this section, the coupling between the momentum and energy equation is delineated in detail. By convention, capital- and lower-case Roman indices are used for referential and spatial components of tensors, while lower-case Greek letters are used for components in the intermediate configuration.

6.4.1 Linearization of the momentum equations

The linearization of the stress-divergence term in (6.7) leads to an expression of the form

$$\sum_{I,J} w_a^I \left[(C_{uu})_{ab}^{IJ} \Delta u_b^J + (C_{u\theta})_a^{IJ} \Delta\theta^J \right] \ , \tag{6.36}$$

where Δu_a^I and $\Delta\theta^I$ denote the increments of the nodal displacements and temperatures, respectively.

Taking into account (6.8) and (6.20), it follows that

$$(C_{uu})_{ab}^{IJ} \ = \ \int_{\Omega_0} N_{,A}^I \frac{\partial P_{aA}}{\partial F_{bB}} N_{,B}^J \ dV \ . \tag{6.37}$$

Concentrating on the material stiffness in (6.21), note that the expression for $\mathbf{S}^e$ in (4.31) for the "FT" model implies that

$$\frac{\partial \mathbf{S}^e}{\partial \mathbf{E}^e} = \mathbb{C} \ . \tag{6.38}$$

It follows that

$$\frac{\partial S_{\alpha\beta}^e}{\partial E_{CD}} \ = \ \frac{\partial S_{\alpha\beta}^e}{\partial E_{\gamma\delta}^e} \frac{\partial E_{\gamma\delta}^e}{\partial E_{CD}} \ = \ \mathbb{C}_{\alpha\beta\gamma\delta} [(F^{t^{-1}})_{C\gamma} (F^{t^{-1}})_{D\delta}]^s \ , \tag{6.39}$$

where the term $[\cdot]^s$ is symmetric with respect to indices {C,D}, and (6.33) and (6.34) have been used to eliminate the contribution of the current deformation on $\mathbb{C}$ and $\mathbf{F}^t$. Hence, using (4.30) one obtains

$$\frac{\partial S_{AB}}{\partial E_{CD}} \ = \ \hat{\mathbb{C}}_{ABCD} \ = \ (F^{t^{-1}})_{A\alpha} (F^{t^{-1}})_{B\beta} \mathbb{C}_{\alpha\beta\gamma\delta} (F^{t^{-1}})_{C\gamma} (F^{t^{-1}})_{D\delta} \ , \tag{6.40}$$

which is the pull-back of the elasticity tensor $\mathbb{C}$ from the intermediate to the reference configuration.

For the "ET" model, the expression (4.41) leads to

$$\frac{\partial S_{AB}}{\partial E_{CD}} \ = \ \mathbb{C}_{ABCD} \ . \tag{6.41}$$

Turning now to the coupling between displacements and temperature, recall (4.31) for the "FT" model to conclude that

$$\frac{\partial \mathbf{S}^e}{\partial \theta} \ = \ -\mathbb{C}\mathbf{A} \ , \tag{6.42}$$

which implies that the tangent term in the momentum equations due to thermal coupling is

$$(C_{u\theta})_a^{IJ} \;=\; -\int_{\Omega_0} N^I_{,A} F^e_{a\alpha} \mathbb{C}_{\alpha\beta\gamma\delta} A_{\gamma\delta} F^{t\,-1}_{A\beta}\, N^J \, dV \;, \tag{6.43}$$

where (4.30), (6.42) and (6.35) are used.

On the other hand, for the "ET" model the expression for stress (4.41) leads to

$$\frac{\partial \mathbf{S}}{\partial \theta} \;=\; -\mathbb{C}\mathbf{A} \;, \tag{6.44}$$

therefore

$$(C_{u\theta})_a^{IJ} \;=\; -\int_{\Omega_0} N^I_{,A} F_{aB} \mathbb{C}_{BACD} A_{CD}\, N^J \, dV \;. \tag{6.45}$$

6.4.2 Linearization of the energy equation

The linearizations of the energy equations (6.31) and (6.32) lead to terms of the form

$$\sum_{I,J} w^I \left[(C_{\theta u})_a^{IJ} \Delta u_a^J + (C_{\theta\theta})^{IJ} \Delta\theta^J \right] \;. \tag{6.46}$$

Two terms in (6.31) and (6.32) contribute to $(C_{\theta u})_a^{IJ}$: the first, $(C^{(t)}_{\theta u})_a^{IJ}$ is due to the phase transformation, while the second, $(C^{(e)}_{\theta u})_a^{IJ}$, is due to the thermoelastic coupling. Writing the linearization of the components of the elastic right Cauchy-Green deformation tensor as

$$(DC^e)_{\alpha\beta} \;=\; \sum_J 2\big[F^e_{a\alpha} N^J_{,A} (F^{t\,-1})_{A\beta}\big]^s \Delta u_a^J \;=\; \sum_J G^J_{a\alpha\beta} \Delta u_a^J \;, \tag{6.47}$$

it follows that for the "FT" model

$$(C^{(t)}_{\theta u})_a^{IJ} \;=\; -\int_{\Omega_0} N^I \left[G^J_{a\alpha\beta} S^e_{\beta\gamma} + C^e_{\alpha\beta} \mathbb{C}_{\beta\gamma\delta\epsilon} G^J_{a\delta\epsilon} \right] \tilde{F}^t_{\alpha\gamma} \, dV \;, \tag{6.48}$$

where $\tilde{\mathbf{F}}^t = \dot{\mathbf{F}}^t \mathbf{F}^{t\,-1} = \sum_\alpha \mathbf{H}^t_\alpha \mathbf{F}^{t\,-1} \dot{\xi}_\alpha$.

For the "ET" model, using (4.40) and (6.41), the tangent can be derived as

$$(C^{(t)}_{\theta u})_a^{IJ} \;=\; -\int_{\Omega_0} N^I\, \mathbb{C}_{ABCD} F_{aC} N^J_{,D} \dot{E}^t_{AB} \, dV \;. \tag{6.49}$$

The second coupling term involves the linearization of $\dot{\mathbf{E}}^e$ in the thermoelastic term

$$\int_{\Omega_0} w\; \dot{\mathbf{E}}^e \cdot \mathbb{C}\mathbf{A}\theta \; dV = \int_{\Omega_0} w\; \dot{E}^e_{\alpha\beta} \mathbb{C}_{\alpha\beta\gamma\delta} A_{\gamma\delta} \theta \, dV \;, \tag{6.50}$$

where (6.34) is used and $\mathbf{A}$ is assumed constant. To obtain the linearization of $\dot{\mathbf{E}}^e$, start by noting that,

$$\dot{E}^e{}_{\alpha\beta} = \left[F^e_{a\alpha}\dot{F}^e_{a\beta}\right]^s = \left[F^e_{a\alpha}\left(\dot{F}_{aB}(F^{t\,-1})_{B\beta} + F_{aB}(\dot{F^t}^{-1})_{B\beta}\right)\right]^s \ . \tag{6.51}$$

Using the identity

$$\dot{\mathbf{F}}^{t\,-1} = -\mathbf{F}^{t\,-1}\dot{\mathbf{F}}^t\mathbf{F}^{t\,-1} \ , \tag{6.52}$$

one obtains

$$\dot{E}^e{}_{\alpha\beta} = \left[F^e_{a\alpha}\left(\dot{F}_{aB}(F^{t\,-1})_{B\beta} + F^e_{a\gamma}(\tilde{F}^t)_{\gamma\beta}\right)\right]^s \ . \tag{6.53}$$

Further, upon employing the Newmark time-integration scheme (6.23), the differential part of $\dot{F}_{aA}$ can be expressed in the form $\sum_J c_2\, N^J_{,A}\Delta u^J_a$, where $(6.25)_2$ is used. This leads to

$$(D\dot{E}^e)_{\alpha\beta} \ = \ \sum_J \left[N^J_{,A}(F^{t\,-1})_{A\alpha}\dot{F}^e_{a\beta} + F^e_{a\alpha}N^J_{,B}(F^{t\,-1})_{B\gamma}\left(c_2\delta_{\gamma\beta} - \tilde{F}^t_{\gamma\beta}\right)\right]^s \Delta u^J_a \ = \ \sum_J H^J_{a\alpha\beta}\Delta u^J_a \ . \tag{6.54}$$

It follows that,

$$(C^{(e)}_{\theta u})^{IJ}_a \ = \ -\int_{\Omega_0} N^I\, H^J_{a\alpha\beta}\mathbb{C}_{\alpha\beta\gamma\delta}A_{\gamma\delta}\theta\, dV \ . \tag{6.55}$$

For the "ET" model, the tangent involves linearizing $\dot{\mathbf{E}}$ since $\mathbf{E}^t$ can be approximated explicitly similar to (6.33). This leads to

$$(C^{(e)}_{\theta u})^{IJ}_a \ = \ \int_{\Omega_0} N^I\left[N^J_{,A}\dot{F}_{aB} + F_{aA}N^J_{,B}\,c_2\right]^s \mathbb{C}_{ABCD}A_{CD}\theta\, dV \ . \tag{6.56}$$

With reference to equation (6.31), the terms that contribute to the thermal stiffness in the energy equation for the "FT" model are

$$\int_{\Omega_0} w\ c\ \dot{\theta}\, dV - \int_{\Omega_0} \mathrm{Grad}\, w\cdot\mathbf{K}\,\mathrm{Grad}\,\theta\, dV + \int_{\Omega_0} w\dot{\mathbf{E}}^e\cdot\mathbb{C}\mathbf{A}\theta\ dV - \int_{\Omega_0} w\ \left[(\mathbf{C}^e\mathbf{S}^e)\cdot\tilde{\mathbf{F}}^t\right] dV \ . \tag{6.57}$$

Noting that the differential of $\dot{\theta}$ in the semi-discrete approximation gives $\sum_J c_2\, N^J\,\Delta\theta^J$, the corresponding tangent terms are obtained in the form

$$(C_{\theta\theta})^{IJ} = \int_{\Omega_0} N^I\ c\ N^J c_2\, dV + \int_{\Omega_0} N^I_{,A}K_{AB}N^J_{,B}\, dV + \int_{\Omega_0} N^I\left(\dot{E}^e_{\alpha\beta}\mathbb{C}_{\alpha\beta\gamma\delta}A_{\gamma\delta} + C^e_{\alpha\beta}\mathbb{C}_{\beta\gamma\delta\epsilon}A_{\delta\epsilon}\cdot\tilde{F}^t_{\alpha\gamma}\right)N^J\, dV \ , \tag{6.58}$$

where $(6.8)_2$ and (6.42) are used. For the "ET" model, the tangent terms are similarly obtained in the form

$$(C_{\theta\theta})^{IJ} = \int_{\Omega_0} N^I c N^J c_2 \, dV + \int_{\Omega_0} N^I_{,A} K_{AB} N^J_{,B} \, dV + \int_{\Omega_0} N^I \dot{E}_{AB} \mathbb{C}_{ABCD} A_{CD} \, N^J \, dV \ , \quad (6.59)$$

with the aid of $(6.8)_2$ and (6.44).

Chapter 7

Multiscale model for polycrystal response

Several materials used in engineering applications exhibit a heterogeneous microstructure. Such heterogeneities are often in the form of inclusions or dispersed fibers, whose thermomechanical properties are distinct from that of the underlying matrix material. Apart from such kinds of composite materials, various polycrystalline metals and alloys are intrinsically heterogeneous due to their individual grains having distinct orientations. In some of these cases, the material is homogeneous at the macroscopic scale since the same pattern of heterogeneous microstructure is repeated at regular intervals. An idealized model of the microstructure obtained by choosing a representative volume having the various heterogeneities is known as the RVE (Representative Volume Element). Several theories have been proposed to obtain the overall properties of a typical RVE by homogenizing its behavior under prescribed local macroscopic states. An assumption crucial to obtaining the macroscopic response through such homogenization techniques is the separation of macroscopic and microscopic length-scales. This entails that the maximum size of the heterogeneities be at least an order lesser than the minimum dimensions of the macroscopic specimen.

Starting from Eshelby's pioneering work [22] on determining the effective properties of a material with an ellipsoidal inclusion embedded in a homogeneous matrix, much research has been conducted to obtain the analytical form of the overall properties of heterogeneous elastic materials undergoing small deformations. Among these works, the self-consistent method has been widely used to obtain the macroscopic moduli of polycrystalline elasto-plastic materials. This is based on the assumption that each crystal in the polycrystalline aggregate is embedded in a material that has the same mechanical properties as the overall properties of the aggregate. An extension of this method with regard to non-linear deformations was provided by [38] and has been used since for applications in polycrystal plasticity and phase transformations, see [41, 50]. However, so far these analytical homogenization procedures could be applied only for heterogeneities with regular geometric shapes (*e.g.* ellipsoids) and where the contrast in microconstituent properties is not large, particularly

when the material undergoes inelastic deformations. A more general framework for obtaining the macro-constitution is provided by computational homogenization techniques. Here, the overall response of an RVE under a given local macroscopic state is obtained by solving a initial/boundary-value problem (IBVP) at microscale. Such computational techniques are effected by applying boundary conditions of the Dirichlet, Neumann or periodic type, through which the independent macroscale state variables are transferred to the microscopic RVE. Due to the general solution strategy adopted in these micro-macro approaches, they can incorporate any kind of non-linear material behavior or geometrical irregularities at the microscale. Some of these computational homogenization techniques employ the finite element method to discretize both the macroscopic and microscopic problems, and are known as the FE^2 techniques. These techniques have been used with success in the context of various composite and polycrystalline materials, see [23, 47].

However in the aforementioned works, the size of the microscale RVE seems to be chosen in an *ad-hoc* manner, and a scientific approach for determining the RVE size appears to be lacking. Some work in this direction has been done in [45, 28], where RVE sizes were determined for microstructured composites and materials with inclusions, using statistical methods based on performing numerical computations to obtain the overall response for randomly chosen RVE samples. Motivated by the work in [45], a statistics-based method is proposed here for determining the optimum RVE size for textured polycrystals [79]. Further, a comparison of the macroscopic response for three FE^2 computational homogenization approaches is performed here for polycrystalline Nitinol.

7.1 Determination of RVE size for textured polycrystals

As discussed above, in the multiscale approach employed here, the local deformation-related information is passed from the coarse (polycrystal) scale to the fine (single-crystal) scale, where it is treated as a mean deformation. The fine scale consists of single crystals, with individual crystallographic orientations distributed according to texture measurements, see Section 3.5 for related discussion. Each single crystal is represented by a finite element in the microscale mesh, as schematically depicted in Figure 7.1. Subsequently, mean stresses are computed at the fine scale and returned to the coarse scale. For such a model, the choice of homogenization procedure for the RVE is of paramount importance. Of the different types of boundary conditions mentioned earlier, the Taylor, fixed and periodic displacement conditions are developed and compared here.

The Taylor method assumes that the local deformation gradient of the coarse scale is applied homogeneously to the entire RVE. This method is computationally inexpensive as it does not require solving a full-scale BVP, due to the fact that equilibrium equations are not enforced in this procedure. Nevertheless, the Taylor method can be used to obtain an upper

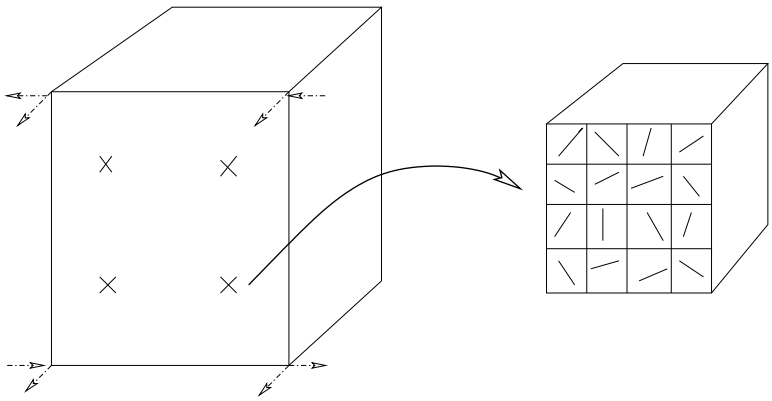

Figure 7.1: *RVE for textured polycrystal assigned to a macroscale continuum point*

bound estimate of the ensemble stiffness, see [39]. This method is employed here to numerically determine an RVE size that accurately resolves the polycrystalline structure. The comparison between this method and the other boundary conditions which requires solving a microscale BVP is deferred to later sections. It can be noted that Taylor averaging in a multiscale finite element setting has also been employed earlier for the study of martensitic phase transformation in [89]. However, here a formal procedure is proposed for determining the RVE size (*i.e.*, number of crystals) and composition (*i.e.*, represented crystal orientations), which takes into account the complete range and frequencies of crystallographic orientations describing the experimentally measured texture. Also, the resulting computational scheme yields local stress responses which are shown to converge with increasing RVE size and with statistical errors being within acceptable limits, even at relatively small RVE sizes.

Following the formal guidelines set in [17], an RVE is defined as the smallest unit of material that can accurately represent the mean macroscopic mechanical response of the textured polycrystals. Here, the crystal orientation and probability distribution data provided by the texture-data analysis program BEARTEX [92] are used to determine the RVE size and composition.

The proposed methodology for the determination of the RVE size and composition is developed along the lines of a general procedure proposed in [45]. It is outlined as follows: First, several potential RVEs are chosen, each having a total of $n = k^3$ crystals, where $k = 2, 3, \ldots$. Throughout this work, each RVE is chosen to contain a cubic power of crystals signifying the assumed lack of directional bias in the crystal formation. Also, given that the BEARTEX measurements do not contain direct information on crystal geometry, all crystals in the reference configuration of the RVE are assumed to be of cubic shape and identical size. For any given RVE size, Monte Carlo sampling is performed to generate several realizations of the RVE. This can be readily accomplished by assigning orientations to each crystal from the texture data using a random process weighted by the probability density of each representable orientation. Subsequently, a set $\mathcal{T}$ of simple deformation tests

is run using a single eight-node brick element to determine a corresponding set of apparent stress responses. In these simulations, different RVE realizations are used to characterize the microstructure at each of the eight integration points of the element. The accuracy of these stress responses is quantified by the relative error of different realizations within each RVE size, as in [45]. To this end, for any computable quantity of interest Z, with mean $\bar{Z}$ and standard deviation $\sigma(Z)$, the Central Limit Theorem [74] implies that the distribution of $\bar{Z}$ is approximately normal, as a function of the number of realizations. As a result, the 95.45% confidence interval (CI) of $\bar{Z}$ is approximately equal to $[\bar{Z} - 2\sigma(Z)/\sqrt{m}, \bar{Z} + 2\sigma(Z)/\sqrt{m}]$, where m is the number of realizations for a given RVE of size n. Said differently, there is a 95.45% probability that the maximum deviation in $\bar{Z}$ of a random RVE sample with n crystals from the mean is less than $2\sigma(Z)/\sqrt{m}$. Hence, reasonable absolute and relative error measures ϵ and ϵ_{rel} in the selection of an RVE with n crystals are given by

$$\epsilon(n) \;=\; \frac{2\sigma(Z(n))}{\sqrt{m}} \tag{7.1}$$

and

$$\epsilon_{rel}(n) \;=\; \frac{2\sigma(Z(n))}{\bar{Z}(n)\sqrt{m}}\;, \tag{7.2}$$

for m RVE samples.

The number of samples m for an RVE of size n can be obtained from

$$m \;=\; \frac{N}{n}\;, \tag{7.3}$$

where N is sufficiently large so that the mean and variance of the samples converge for all RVE sizes n. Equation (7.3) shows that the required number of samples m decreases with increasing n, since convergence is faster with larger RVE sizes due to their better representation of effective properties.

Here, it is stipulated that $N = 10^4$ and $n \in \mathcal{S} = \{k^3,\ k = 2, 3, \ldots, 10\}$. Also, the single element tests involving displacement controlled loading and the Taylor method are enumerated in the set $\mathcal{T}$ defined as,

$$\mathcal{T} \;=\; \{\text{tension, torsion, combined tension-torsion}\}\;. \tag{7.4}$$

As in [45], the optimal RVE size n is defined as the one for which a single realization is required to estimate the mean property $\bar{Z}$ within a maximum relative error of $tol = 2\%$. Hence, $m = 1$ is used in (7.1) for computing the relative error. The complete algorithm for determining the RVE size based on the preceding methodology is summarized in Box 7.1. The quantity Z is taken as the Mises equivalent stress, which is given in terms of the components of Cauchy stress tensor as

$$T_{\text{mises}} = \frac{1}{\sqrt{2}}\left[(T_{11}-T_{22})^2 + (T_{22}-T_{33})^2 + (T_{33}-T_{11})^2 + 6(T_{12}^2 + T_{23}^2 + T_{31}^2)\right]^{1/2}\;. \tag{7.5}$$

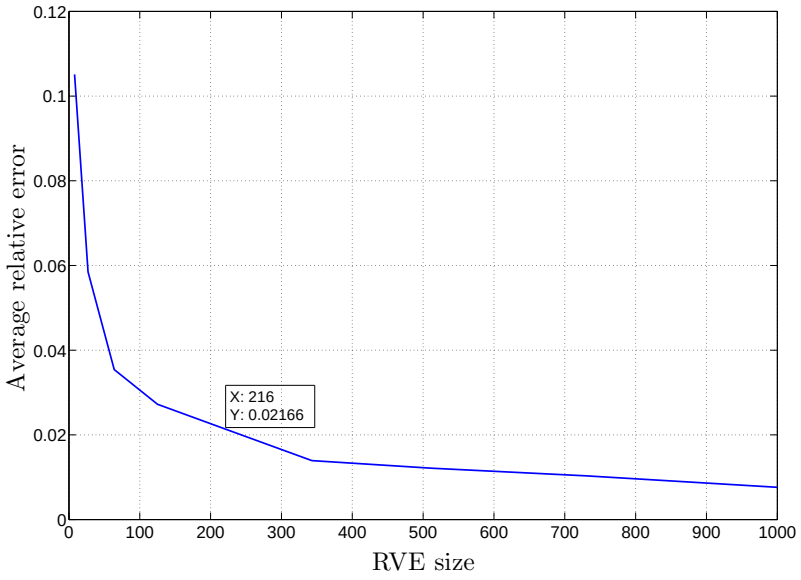

Figure 7.2: *Average relative error in equivalent stresses vs. RVE size for tension. The relative error is averaged at 6 points on L/UL curve.*

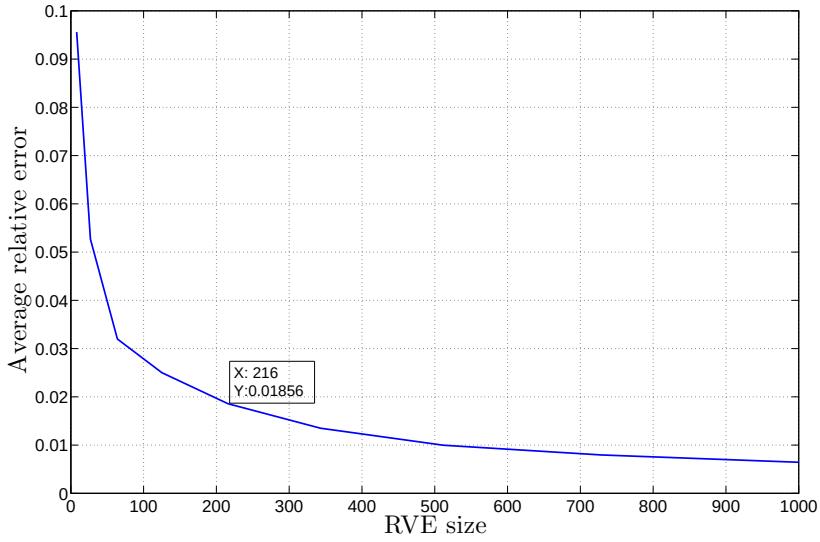

Figure 7.3: *Average relative error in equivalent stresses vs. RVE size for torsion. The relative error is averaged at 6 points on L/UL curve.*

Upon applying this algorithm it is found that the desired level of accuracy is reached for $n = 6^3 (= 216)$. The error plots in Figures 7.2, 7.3, and 7.4 confirm this finding. Note that only for the tension test the error slightly exceeded 2%, but when the simulations for tension were done with different RVE sizes it was found that the results converge with RVE size of 216. So a larger RVE size was not necessary.

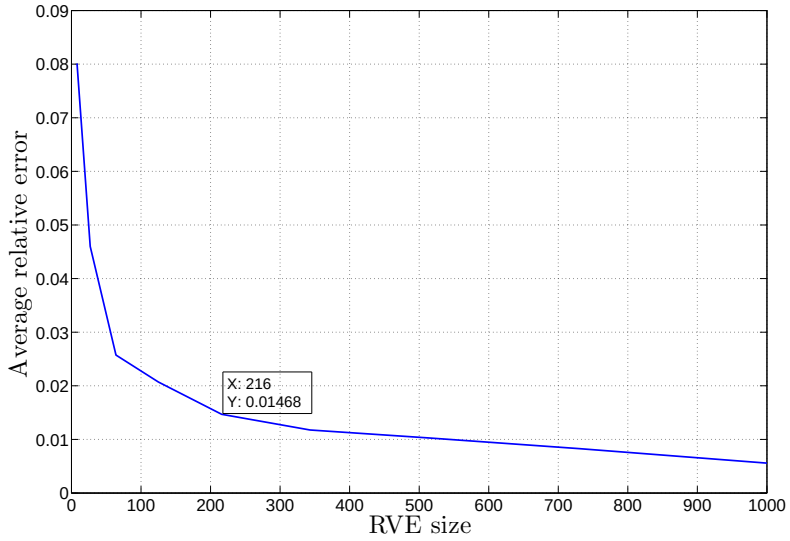

Figure 7.4: *Average relative error in equivalent stresses vs. RVE size for combined tension-torsion. The relative error is averaged at 6 points on L/UL curve.*

1. Input $N > 0$, RVE size set $\mathcal{S}$, test set $\mathcal{T}$, strain set $\mathcal{P}$, and error tolerance $tol > 0$
2. Loop over RVE sizes $n \in \mathcal{S}$
   - 2a. Compute the number of samples $m = N/n$
   - 2b. Generate a set $sp = \{sp_1, sp_2, ..., sp_m\}$ of m different random RVE samples of size n
   - 2c. Loop over $t \in \mathcal{T}$
     - i. Loop over $s \in sp$

       Perform complete loading/unloading test t for sample s and compute effective stresses $S_i(n,t)$ corresponding to the i-th strain in $\mathcal{P}$
     - ii. End loop for s
     - iii. Compute the mean $\bar{S}_i(n,t)$ and variance $\sigma_i(n,t)$ over all m samples for each $S_i(n,t)$ corresponding to the i-th strain in $\mathcal{P}$
     - iv. Compute the relative errors $\epsilon_{rel,i}(n,t) = \dfrac{2\sigma_i(n,t)}{\bar{S}_i(n,t)}$
     - v. Compute the overall relative error $\bar{\epsilon}_{rel}(n,t)$ as the mean of $\epsilon_{rel,i}(n,t)$ over all strains in $\mathcal{P}$
   - 2d. End loop for t
3. End loop for n
4. Determine $n = \max_{t\in\mathcal{T}}\big\{n(t) = \arg\min_{n\in\mathcal{S}}\{\bar{\epsilon}_{rel}(n,t) < tol\ ,\ t \in \mathcal{T}\}\big\}$

Box 7.1: A summary of the algorithm to determine the optimal RVE size

7.2 Mechanical BVP for RVE and computational approach

In this section, a procedure for obtaining the macroscopic quantities of interest for the mechanical BVP through homogenization principles is elaborated. In the following, a superscript "m" as in $(.)^m$ will be used to denote physical quantities at microscale, while superscript "M" as in $(.)^M$ will be used to denote physical quantities at macroscale. At microscale, local equilibrium is satisfied without body forces or inertia terms due to length-scale separation, *i.e.*

$$\text{Div } \mathbf{P}^m = \mathbf{0} \ . \tag{7.6}$$

This is because the length parameter enters the equilibrium equation only through the term in (7.6), and as this parameter approaches the length-scale of the RVE, body force and inertia terms become insignificant in comparison to this term. This can also be mathematically derived through the asymptotic expansion technique by introducing an order parameter, see [24]. However, note that the full equilibrium equation can be solved at macro-scale by averaging the body force and inertia terms over the RVE. The RVE is assumed to satisfy the Hill-Mandel macro-homogeneity condition [37, 47]. This states that the local stored energy at the macroscale is obtained as average of the stored energy over the microscale RVE. For the case of finite deformation, this may be expressed mathematically in the form

$$\frac{1}{V}\int_{\omega_0} \mathbf{P}^m \cdot \mathbf{F}^m \ dV = \mathbf{P}^M \cdot \mathbf{F}^M \ , \tag{7.7}$$

where ω_0 is the reference domain of the RVE with volume V. The microscale deformation gradient is defined as $\mathbf{F}^m = \text{Grad}\, \boldsymbol{\chi}^m(\mathbf{X}^m, t)$, where $\mathbf{x}^m = \boldsymbol{\chi}^m(\mathbf{X}^m \ , t)$ is the position vector of a microscale point in the current configuration. The relation between the micro-quantities and their RVE-averaged values, denoted by $\bar{(.)}$, is given as

$$\frac{1}{V}\int_{\omega_0} \mathbf{P}^m \cdot \mathbf{F}^m \ dV - \bar{\mathbf{P}} \cdot \bar{\mathbf{F}} = \frac{1}{V}\int_{\partial\omega_0} (\mathbf{p} - \bar{\mathbf{P}}\mathbf{N}) \cdot (\mathbf{x}^m - \bar{\mathbf{F}}\mathbf{X}^m) \ dA \ , \tag{7.8}$$

where $\partial\omega_0$ is the boundary of domain ω_0 and $\mathbf{p} = \mathbf{P}^m\mathbf{N}$ is the Piola traction. That (7.8) holds, can be verified by applying divergence theorem after writing out all the terms in the RHS. Thus, if the macroscopic first Piola-Kirchhoff stress and deformation gradients are taken to be the average of corresponding microscale quantities, then the energy criterion (7.7) is satisfied if the boundary conditions are set in terms of either displacements or tractions so that one of the following holds:

$$\begin{aligned} \mathbf{x}^m - \bar{\mathbf{F}}\mathbf{X}^m &= \mathbf{0} \quad \text{on } \partial\omega_0 \ , \\ \mathbf{p} - \bar{\mathbf{P}}\mathbf{N} &= \mathbf{0} \quad \text{on } \partial\omega_0 \ , \\ \int_{\partial\omega_0} (\mathbf{p} - \bar{\mathbf{P}}\mathbf{N}) \cdot (\mathbf{x}^m - \bar{\mathbf{F}}\mathbf{X}^m) \ dA &= 0 \ . \end{aligned} \tag{7.9}$$

Equations $(7.9)_1$ and $(7.9)_2$ correspond to what are known as displacement and traction boundary conditions respectively. Further, the periodic boundary conditions satisfy $(7.9)_3$.

The displacement boundary conditions are obtained by applying displacements on the RVE boundary in accordance with $(7.9)_1$, given by

$$\mathbf{u} \;=\; (\mathbf{F}^M - \mathbf{I}_1)\mathbf{X}^m \;, \tag{7.10}$$

where $\mathbf{I}_1$ stands for the second-order two-point identity tensor. This ensures that the average deformation gradient over the RVE is equal to $\mathbf{F}^M$ which can be proved as follows:

$$\frac{1}{V}\int_{\omega_0} \mathbf{F}^m \, dV = \frac{1}{V}\int_{\omega_0} \operatorname{Grad} \boldsymbol{\chi}^m \, dV = \frac{1}{V}\int_{\partial\omega_0} \mathbf{x}^m \otimes \mathbf{N} \, dA = \mathbf{F}^M \;, \tag{7.11}$$

where the last identity holds by using $(7.9)_1$ and divergence theorem. The traction boundary condition is obtained by applying the Piola traction on the RVE boundary given by

$$\mathbf{p} = \mathbf{P}^M \mathbf{N} \;. \tag{7.12}$$

In this case the average first Piola-Kirchhoff stress over the RVE is equal to its macroscopic counterpart which can be proved as follows:

$$\frac{1}{V}\int_{\omega_0} \mathbf{P}^m \, dV = \frac{1}{V}\int_{\omega_0} \operatorname{Div}(\mathbf{X}^m \otimes \mathbf{P}^m)^T \, dV = \frac{1}{V}\int_{\partial\omega_0} \mathbf{p} \otimes \mathbf{X}^m \, dA \;=\; \mathbf{P}^M \;, \tag{7.13}$$

where the first identity holds as a result of (7.6) and the last one holds by using (7.12) and applying the divergence theorem.

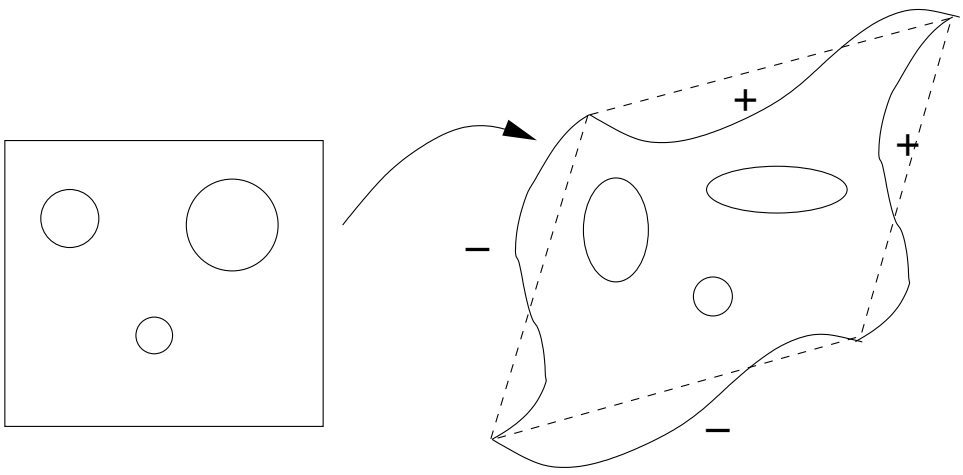

Figure 7.5: *Deformation of an RVE under periodic boundary conditions*

In the periodic case, the boundary displacements on an initially periodic (*e.g.*, cubic) RVE satisfy the condition

$$\mathbf{u}^+ \;=\; \mathbf{u}^- + (\mathbf{F}^M - \mathbf{I})(\mathbf{X}^+ - \mathbf{X}^-) \;, \tag{7.14}$$

where the superscripts "+" and "−" signify points which lie on opposite faces of the periodic RVE. Figure 7.5 illustrates the deformation of an RVE under periodic boundary conditions. This boundary condition also satisfies the deformation gradient identity proved in (7.11). Further, it satisfies $(7.9)_3$ due to the fact that the tractions and normals at two corresponding points on opposite faces are equal in magnitude and opposite of each other, i.e. $\mathbf{p}^+ = -\mathbf{p}^-$ and $\mathbf{N}^+ = -\mathbf{N}^-$.

In this work, the displacement and periodic boundary conditions are implemented to compare the macroscopic response in the context of phase transformations in polycrystals.

7.2.1 Average stresses and tangents in FE framework

In finite element framework, the above boundary conditions are applied to the boundary nodes of an RVE mesh and the averaged quantities are obtained in the form of a sum over the nodes of the RVE mesh. Thus, the following can be derived when (7.7) holds at microscale:

$$P^M_{aB} = \frac{1}{V}\int_{\omega_0} P^m_{aB}\, dV = \frac{1}{V}\int_{\partial\omega_0} X_B\, p_a dA = \frac{1}{V}\sum_{E\in\text{ext}} X^E_B\, f^E_a\ , \tag{7.15}$$

where "ext" stands for the set of boundary nodes of the RVE. Here, $\mathbf{f}^E$ are equivalent tractions at the boundary nodes and is obtained from the boundary residuals of the equilibrium equation and $\mathbf{X}^E$ is the position vector of node E in reference configuration. When the microscale problem converges for some imposed boundary conditions on the RVE, the variations of residuals for the free or internal nodes vanish. Thus, variations of the displacements at internal degrees of freedom (DOFs), denoted by $\delta\mathbf{d}^I$, can be expressed in terms of those of boundary DOF displacements denoted by $\delta\mathbf{d}^E$ as,

$$\begin{aligned} &[C^{JI}]\,[\delta d^I] + [C^{JE}]\,[\delta d^E] = [0]\ , \qquad I, J \in \text{int}\ , E \in \text{ext} \\ \text{or}\quad &[\delta d^I] = -[C^{JI}]^{-1}\,[C^{JE}]\,[\delta d^E]\ , \end{aligned} \tag{7.16}$$

where $[C^{JI}]$ is the submatrix of the tangent moduli computed for finite element solution corresponding to the J and I nodes and $[\delta d^I]$ stands for variation of I-th node displacement. Also, "int" stands for the set of internal nodes of RVE. Now, to get consistent tangent moduli of homogenized stresses, first note that variations of independent macroscale deformation gradient affect the mechanical displacement at boundary DOFs of the RVE through (7.10). Therefore, the variation in mechanical displacement at the boundary DOF F is given by

$$\delta u^F_a = \delta F^M_{aB}\, X^F_B\ , \qquad F \in \text{ext}\ . \tag{7.17}$$

Further, the variation of mechanical residual for external DOFs is given by

$$\delta f^E_a = C^{EF}_{ab}\,\delta u^F_b + C^{EI}_{ab}\,\delta u^I_b = \hat{C}^{EF}_{ab}\,\delta u^F_b; \quad E, F \in \text{ext}\ ,\ I \in \text{int}\ , \tag{7.18}$$

where $(7.16)_2$ has been used. In the above,

$$\hat{C}^{EF} = [C^{EF}] - [C^{EI}][C^{JI}]^{-1}[C^{JF}] \ , \qquad E,F \in \text{ext} \ , \ I,J \in \text{int} \tag{7.19}$$

are the statically condensed tangent moduli for the external DOFs. Therefore, using $(7.15)_3$, (7.17) and (7.18), one gets the elastic tangent modulus as

$$\bar{A}_{aBbC} = \frac{\partial P^M_{aB}}{\partial F^M_{bC}} = \frac{1}{V} \sum_{E\in\text{ext}} \sum_{F\in\text{ext}} X^E_B \ \hat{C}^{EF}_{ab} \ X^F_C \ , \tag{7.20}$$

[47]. A computationally inexpensive way of computing the above tangent is achieved by first computing the matrices

$$\begin{aligned} G^J_{a,bC} &= \sum_{F\in\text{ext}} C^{JF}_{ab} \ X^F_C \\ G^I_{Ba,b} &= \sum_{E\in\text{ext}} X^E_B \ C^{EI}_{ab} \\ H_{Ba,bC} &= \sum_{E\in\text{ext}} \sum_{F\in\text{ext}} X^E_B \ C^{EF}_{ab} \ X^F_C \ , \qquad E,F \in \text{ext} \ , \ I,J \in \text{int} \ , \end{aligned} \tag{7.21}$$

and then noting that (7.20) can be written as

$$[\bar{A}] = \frac{1}{V} \sum_{E\in\text{ext}} \sum_{F\in\text{ext}} \left([H] - [G^I] \, [C^{JI}]^{-1} \, [G^J] \right) \ . \tag{7.22}$$

In the case of periodic boundary conditions, the corner nodes are deformed according to the macroscopic deformation gradient as in (7.10), while the other boundary nodes are linked by the periodic condition (7.14). Since the tractions are antiperiodic in this case, equation (7.15) yields the the macroscale Piola-Kirchhoff stress as

$$P^M_{aB} = \frac{1}{V} \sum_{E\in\text{ext}} X^E_B \ f^E_a = \frac{1}{V} \left[\sum_{E\in\text{fix}} X^E_B \ f^E_a + \sum_{E\in p+} (X^E_B - X^{E-}_B) f^E_a \right] \ , \tag{7.23}$$

where "fix" and "p+" stand, respectively, for the corner (fixed) nodes, and the nodes on the "+" face linked through the periodicity condition (7.14), of the RVE. Denoting by $\hat{\mathbf{X}}^E$, both $(\mathbf{X}^E - \mathbf{X}^{E-})$ for the "p+" nodes and $\mathbf{X}^E$ for the fixed nodes, one obtains

$$P^M_{aB} = \frac{1}{V} \sum_{E\in\text{fix,p+}} \hat{X}^E_B \ f^E_a \ . \tag{7.24}$$

Further, using (7.14), the variation of boundary DOFs is given by

$$\delta u^F_b = \delta F^M_{bB} \hat{X}^F_B \qquad F \in \text{fix,p+} \ . \tag{7.25}$$

In analogy to (7.20), the tangent moduli for the periodic case is obtained as

$$\bar{A}_{aBbc} = \frac{\partial P^M_{aB}}{\partial F^M_{bC}} = \frac{1}{V} \sum_E \sum_F \hat{X}^E_B \, \hat{C}^{EF}_{ab} \, \hat{X}^F_C \qquad E,F \in \text{fix,p+} \ . \tag{7.26}$$

7.3 Thermomechanical IBVP for RVE and computational approach

Solving the thermomechanically coupled IBVP typically involves satisfying both the linear momentum balance equation and the energy equation, as discussed in Chapter 4. The multiscale thermomechanical problems that have been pursued in literature vary not only in application, but also in the precise nature of the coupling between the momentum and energy equations at two scales. In some works, a one-way coupled problem where only the momentum equations are coupled to the energy equation through temperature effects, is attempted [88, 93]. Also, the micro-macro transition is effected through a non-local asymptotic homogenization approach, with applications in problems like poro-elasticity [88] and thermal shock waves [93]. On the other hand, other works focus on solving the thermomechanical problem in an uncoupled (staggered) manner using first-order homogenization techniques within FE^2 framework, see [72]. This is computationally more feasible than the above asymptotic homogenization approach. Thus, the full two-way coupling between mechanical and thermal problems present in dissipative processes like phase transformations in shape-memory alloys and plastic deformation in metals, has not been addressed so far. In this work, a method of solving this fully coupled multiscale thermomechanical problem using first-order homogenization is proposed both in terms of theory and algorithmic implementation. A monolithic solution approach has been adopted at both scales, which entails computing all coupled terms in the stiffness matrix generated for each Newton iteration.

The referential macroscale balance of linear momentum and energy equations in reference configuration are stated as

$$\begin{aligned} \operatorname{Div} \mathbf{P}^M + \rho_0^M \mathbf{b}^M &= \rho_0^M \mathbf{a}^M \ , \\ -\operatorname{Div} \mathbf{q}^M + r^M &= c^M \dot{\theta}^M \ . \end{aligned} \tag{7.27}$$

In the above, r^M is the cumulative macroscopic heat supply per unit volume due to external heat source, mechanical dissipation and thermoelastic coupling. It is assumed here that the microscale is separated in length and time-scales from the macroscale. Hence, it can be argued that the microscale reaches a "steady state" within a fraction of the duration in which an incremental change of the macroscale thermomechanical state takes place. Precisely speaking, "steady state" at the microscale signifies the instantaneous thermomechanical state corresponding to the macroscale state at the end of an incremental change [72]. Further, the heating due to mechanical dissipation and thermoelastic coupling can be neglected in microscale due to the scale separation. Similar to the argument for the mechanical case, the $\operatorname{Div} \mathbf{q}^m$ term dominates at the microscale so that the heat supply is negligible in comparison. Although this heat generation does not affect the instantaneous microscale response, its effect is significant at the macroscopic length-scale. Hence it should be accounted for at the macroscale during each time-increment, by homogenizing over the RVE. The rate terms in the microscale heat supply, whose precise expression is given in (4.33), may be approximated

by the average rate over the macroscale time-increment. Thus the microscale equations corresponding to (7.27) are

$$\begin{aligned} \operatorname{Div} \mathbf{P}^m &= \mathbf{0} \ , \text{ and} \\ -\operatorname{Div} \mathbf{q}^m &= 0 \ . \end{aligned} \tag{7.28}$$

In the multiscale problem, $\mathbf{F}^M$, θ^M and $(\boldsymbol{\nabla}\theta)^M$ are passed from the macroscale to the microscale, while $\mathbf{P}^M$, $\mathbf{q}^M$, r^M, ρ_0^M and c^M are obtained through homogenization over the RVE and returned to the macroscale. Here, $\boldsymbol{\nabla}\theta$ denotes the referential gradient of temperature. The displacement-type mechanical boundary condition discussed in Section 7.2 is initially employed here. The displacement-type thermal boundary condition is supplied as

$$\theta = \theta^M + (\boldsymbol{\nabla}\theta)^M \cdot (\mathbf{X} - \mathbf{X}^c) \ , \tag{7.29}$$

over the boundary $\partial\omega_0$ of the RVE. Here, $\mathbf{X}^c$ is the referential position vector of the centroid of the RVE. The above boundary condition ensures that the temperatures at the boundary of the RVE are linearly distributed according to the macroscopic temperature gradient $(\boldsymbol{\nabla}\theta)^M$, and this linear field over the RVE has an average value equal to the macroscopic temperature θ^M occurring at the centroid of the RVE. Further, this boundary condition enforces that the average temperature gradient over the RVE be equal to its macroscopic counterpart.

7.3.1 Averaged thermomechanical quantities and coupled tangents in FE framework

Here, the degrees of freedom for the thermomechanical problem include both mechanical displacements and temperature which can be jointly expressed as

$$\mathbf{d} = \left\{ \begin{array}{c} \mathbf{u} \\ \theta \end{array} \right\} . \tag{7.30}$$

Hence, the variation of mechanical residual for external nodes is suitably modified from (7.18), for the thermomechanical problem as

$$\delta f_a^E = \hat{C}^{EF}_{uu,ab} \ \delta u_b^F + \hat{C}^{EF}_{u\theta,a} \ \delta\theta^F \ , \qquad E, F \in \text{ext} \ . \tag{7.31}$$

In the above, the subscript 'uu' is used to denote the pure displacement stiffness terms, and '$u\theta$' is used to denote the stiffness at displacement DOFs due to thermal coupling. Using (7.29), the variations in boundary temperatures can be expressed in terms of the independent variations of θ^M and $(\boldsymbol{\nabla}\theta)^M$ at macroscale as

$$\delta\theta^F = \delta\theta^M + (\delta\nabla\theta)^M_A \ (X_A^F - X_A^c) \ , \qquad F \in \text{ext} \ . \tag{7.32}$$

Therefore using $(7.15)_3$, (7.31) and (7.32) one finds the macroscopic thermal expansion tangent moduli to be

$$\frac{\partial P^M_{aB}}{\partial \theta^M} = \frac{1}{V} \sum_{E\in\text{ext}} \sum_{F\in\text{ext}} X^E_B \; \hat{C}^{EF}_{u\theta,a} \; . \tag{7.33}$$

Earlier research has used an averaging principle similar to the Hill-Mandel macro-homogeneity condition (7.7) to obtain the macroscopic heat flux from the microscopic one, through the consistency of an internal entropy like term $\mathbf{q}\cdot\boldsymbol{\nabla}\theta$, see [69, 71]. Although this provides a means for transferring the heat flux to the macroscale, the rationale for averaging an internal entropy term, instead of a term in the energy equation, is not well-founded. Further, the extension of this principle to the case of other irreversible problems appears tenuous, where the internal entropy involves effects of both heat conduction and mechanical dissipation. However, employing this principle one obtains the macroscopic heat flux as a volume average of heat flux over the RVE, with the displacement or periodic thermal boundary conditions. Using this result, it can be shown that

$$q^M_A = \frac{1}{V}\int_{\omega_0} q^m_A \; dV = \frac{1}{V}\int_{\partial\omega_0} X_A(q^m_B N_B) \; dA = \frac{1}{V}\sum_{E\in\text{ext}} X^E_A \; q^E_n \; , \tag{7.34}$$

where $(7.28)_2$ has been used. In the above, q^E_n is the equivalent normal heat flux on the boundary nodes that can be obtained from the boundary residual of the heat equation. Note that the macroscopic heat flux is obtained here in terms of the normal flux over the RVE boundary, where the macroscopic thermal gradient was applied, hence providing a physical ground for the above volume averaging procedure. Based on this physical motivation, the aforementioned homogenization approach is adopted here as a first assumption, and $(7.34)_3$ is used to computationally obtain the macroscopic heat flux. So the variation of the thermal residual at the boundary nodes can be written as

$$\delta q^E_n = \hat{C}^{EF}_{\theta\theta} \; \delta\theta^F \; . \tag{7.35}$$

Note that the term involving "θu" part of the stiffness matrix is not included. This is because, in the microscale BVP, the energy equation $(7.28)_2$ does not explicitly depend on the displacement DOFs. Therefore using (7.34), (7.35) and (7.32) the referential macro-conductivity $\mathbf{K}^M$ has components

$$K^M_{AB} \;=\; \frac{\partial q^M_A}{\partial(\nabla\theta)^M_B} \;=\; \frac{1}{V}\sum_{E\in\text{ext}} \sum_{F\in\text{ext}} X^E_A \; \hat{C}^{EF}_{\theta\theta} \; (X^F_B - X^c_B) \; . \tag{7.36}$$

Early work on obtaining variational bounds for macroscale heat capacity of thermoelastic composites undergoing small deformations is documented in [76]. These bounds were shown to coincide for isotropic composites, and be equal to the volume average of the microscale heat capacity when the microscale coefficient of thermal expansion is homogeneous. Such a

result has also been derived earlier, albeit without any condition on the coefficient of thermal expansion at microscale, in a work on effective thermal properties of periodic composites, by employing an asymptotic expansion method [5]. This result has also been adopted in [71]. In this work too, the macroscopic heat capacity c^M is taken to be the average of the microscopic heat capacity c^m over the RVE, where c^m is independent of either deformation or temperature. Further, the macroscopic reference mass density ρ_0^M is also assumed to be average of its microscopic counterpart. It was discussed earlier in Section 7.3 that the heat source, dissipation and thermoelastic heating can be captured in a single macro-scale heat supply term r^M, which may be obtained by homogenizing over the RVE its microscale counterpart, denoted here by r^m. Here the rate terms of microscale state quantities in r^m, are computed through finite difference approximation of the time derivatives, in an average sense over the macroscale time-step. Hence we have,

$$r^M = \frac{1}{V}\int_{\omega_0} r^m \, dV \ . \tag{7.37}$$

In order to determine the macroscale tangent moduli due to the heating r^M, one starts by noting that the variations of the microscale deformation gradient in finite element setting can be expressed through derivatives of the shape functions and the variations of nodal mechanical displacements as

$$\delta F^m_{aB} = \sum_{E\in\text{ext}} N^E_{,B}\ \delta u^E_a + \sum_{I\in\text{int}} N^I_{,B}\ \delta u^I_a \ . \tag{7.38}$$

Also, the variation of microscale temperature in the finite element setting, can be expressed through the shape functions and variations of nodal temperatures as

$$\delta\theta = \sum_{E\in\text{ext}} N^E\ \delta\theta^E + \sum_{I\in\text{int}} N^I\ \delta\theta^I \ . \tag{7.39}$$

The variation of r^M in terms of the microscale displacements is obtained with the aid of (7.37), (7.38) and (7.39) as

$$\begin{aligned}\delta r^M = \frac{1}{V}\sum_{E\in\text{ext}}\left[\left(\int_{\omega_0}\frac{\partial r^m}{\partial F^m_{aA}}\ N^E_{,A}\ dV\right)\delta u^E_a + \left(\int_{\omega_0}\frac{\partial r^m}{\partial\theta^m}\ N^E\ dV\right)\delta\theta^E\right] + \\ \frac{1}{V}\sum_{I\in\text{int}}\left[\left(\int_{\omega_0}\frac{\partial r^m}{\partial F^m_{aA}}\ N^I_{,A}\ dV\right)\delta u^I_a + \left(\int_{\omega_0}\frac{\partial r^m}{\partial\theta^m}\ N^I\ dV\right)\delta\theta^I\right] \ .\end{aligned} \tag{7.40}$$

Thus, the tangent moduli for r^M are given by

$$\begin{aligned}\frac{\partial r^M}{\partial F^M_{aB}} = \frac{1}{V}\sum_{E\in\text{ext}}\left[\int_{\omega_0}\frac{\partial r^m}{\partial F^m_{aA}}\ N^E_{,A}\ dV + \right. \\ \left.\sum_{I\in\text{int}}\left(\int_{\omega_0}\frac{\partial r^m}{\partial F^m_{bA}}\ N^I_{,A}\ dV\right)\sum_{J\in\text{int}}\left(-(C^{JI})^{-1}C^{JE}\right)_{uu,ba}\right] X^E_B \ ,\end{aligned} \tag{7.41}$$

and

$$\frac{\partial r^M}{\partial \theta^M} = \frac{1}{V} \sum_{E \in \text{ext}} \left[\int_{\omega_0} \frac{\partial r^m}{\partial \theta^m} \, N^E \, dV + \sum_{I \in \text{int}} \left(\int_{\omega_0} \frac{\partial r^m}{\partial \theta^m} \, N^I \, dV \right) \sum_{J \in \text{int}} \left(-(C^{JI})^{-1} C^{JE} \right)_{\theta\theta} \right.$$
$$\left. + \sum_{I \in \text{int}} \left(\int_{\omega_0} \frac{\partial r^m}{\partial F^m_{bA}} \, N^I_{,A} \, dV \right) \sum_{J \in \text{int}} \left(-(C^{JI})^{-1} C^{JE} \right)_{u\theta,b} \right] . \quad (7.42)$$

In the above, the variations (7.17) and (7.32), and appropriate submatrices of $(7.16)_2$ have been used.

The above computational approach can be applied to the case of periodic boundary condition as well, in a way similar to the derivation for the pure mechanical case. Here, the temperature boundary condition (7.29) is applied to the corner nodes, while the other boundary nodes are linked by the periodic condition

$$\theta^+ = \theta^- + (\boldsymbol{\nabla}\theta)^M \cdot (\mathbf{X} - \mathbf{X}^-) \, , \quad (7.43)$$

similar to (7.14) for mechanical displacements. Also, akin to the derivation of macroscopic first Piola-Kirchhoff stress in (7.24), the referential heat flux for the periodic case is obtained as

$$q^M_A = \frac{1}{V} \sum_{E \in \text{fix,p+}} \hat{X}^E_A \, q^E_n \, , \quad (7.44)$$

where q^E_n is antiperiodic over the RVE boundary.

7.4 Averaged thermomechanical quantities and coupled tangents in spatial configuration

The thermomechanical quantities and corresponding tangent moduli were derived in the reference configuration so far. However these derivations can also be done in the spatial configuration for higher computational efficiency. In fact, if macroscopic Kirchhoff stresses (6 independent components owing to symmetry), heat supply and corresponding tangent moduli (49 independent components owing to symmetry) are returned from microscale, then a buffer for 56 words is required. This greatly reduces the data transfer compared to the case of returning first Piola-Kirchhoff stresses (9 components), heat supply and corresponding tangent moduli (100 components), which requires a buffer for 110 words. Thus, these quantities will henceforth be derived in the current configuration.

Using $(7.13)_3$, the Kirchhoff stress tensor is given as

$$\boldsymbol{\tau}^M = \mathbf{P}^M \mathbf{F}^{M^T} = \frac{1}{V} \int_{\partial\omega_0} \mathbf{p} \otimes (\mathbf{F}^M \mathbf{X}^m) \, dV \, . \quad (7.45)$$

Substituting the boundary condition (7.10) in (7.15), one may obtain the components of the Kirchhoff stress and the Cauchy stress respectively as

$$\tau_{ab}^{M} = \frac{1}{V} \sum_{E \in \text{ext}} x_b^E \; f_a^E \; , \qquad \sigma_{ab}^{M} = \frac{\tau_{ab}^{M}}{J^M} = \frac{1}{v} \sum_{E \in \text{ext}} x_b^E \; f_a^E \; , \tag{7.46}$$

where $\mathbf{x}^E$ is the current position of the node E, and $v = J^M V$ is the current volume of the RVE. The tangent moduli for the Kirchhoff stresses due to deformation are obtained using the equation

$$\bar{c}_{abcd} = \left[\frac{\partial \tau_{ab}}{\partial F_{cB}} F_{dB} \right]^s = \bar{\hat{c}}_{abcd} + \frac{1}{2} (\delta_{ac} \tau_{bd}^M + \delta_{ad} \tau_{bc}^M) \; , \tag{7.47}$$

where the term $[\cdot]^s$ is symmetric with respect to indices {c,d} and $\bar{\hat{c}}_{abcd}$ is expressed as

$$\bar{\hat{c}}_{abcd} = F_{bB}^M \bar{A}_{aBcC} F_{Cd}^M \; . \tag{7.48}$$

An expression for stresses and tangents in current coordinates, similar to the displacement boundary condition, can also be derived for the periodic case. The Kirchhoff and Cauchy stresses in this case are respectively given as

$$\tau_{ab}^{M} = \frac{1}{V} \sum_{E \in \text{ext,p+}} \hat{x}_b^E \; f_a^E \; , \qquad \sigma_{ab}^{M} = \frac{\tau_{ab}^{M}}{J^M} = \frac{1}{v} \sum_{E \in \text{ext,p+}} \hat{x}_b^E \; f_a^E \; , \tag{7.49}$$

where $\hat{\mathbf{x}}^E$ denotes both $(\mathbf{x}^E - \mathbf{x}^{E-})$ for the "p+" nodes and $\mathbf{x}^E$ for the fixed nodes. The tangent moduli are obtained from (7.47) and (7.26). The tangent moduli for the Kirchhoff stresses due to temperature is expressed as

$$\frac{\partial \tau_{ab}^{M}}{\partial \theta^M} == \frac{1}{V} \sum_{E \in \text{ext}} \sum_{F \in \text{ext}} x_b^E \; \hat{C}_{u\theta,a}^{EF} \; , \tag{7.50}$$

where (7.45) and (7.33) are used.

In the current configuration with boundary condition (7.29), the macroscopic heat flux is given as

$$\tilde{\mathbf{q}}^M = \frac{1}{J^M} \mathbf{F}^M \mathbf{q}^M = \frac{1}{V} \sum_{E \in \text{ext}} x_a^E \; q_n^E \; , \tag{7.51}$$

where (7.34) is used. Hence the macro-conductivity in current configuration can be obtained as

$$K_{ab}^{M} = \frac{1}{v} \sum_{E \in \text{ext}} \sum_{F \in \text{ext}} x_a^E \; \hat{C}_{\theta\theta}^{EF} \; (x_b^F - x_b^c) \; . \tag{7.52}$$

The tangent (7.41) can also be pushed forward to the current configuration as

$$\frac{\partial r^M}{\partial e^M_{cd}} = \frac{1}{V} \sum_{E \in \text{ext}} \left[\int_{\omega_0} \left(\frac{\partial r^m}{\partial F^m_{cA}} F^m_{aA} \right)^s N^E_{,a} \, dV + \right.$$
$$\left. \sum_{I \in \text{int}} \left(\int_{\omega_0} \left(\frac{\partial r^m}{\partial F^m_{bA}} F^m_{aA} \right)^s N^I_{,a} \, dV \right) \sum_{J \in \text{int}} \left(-(C^{JI})^{-1} C^{JE} \right)_{uu,bc} \right] x^E_d \ . \quad (7.53)$$

Chapter 8

Numerical simulations

The purpose of this chapter is to demonstrate the predictive capacity of the proposed models for single-crystal and polycrystalline Nitinol, subjected to quasistatic or dynamic mechanical loading conditions. To this end, finite element method with displacement formulation is employed to perform numerical simulations. The Newton-Raphson iterative procedure is applied to solve the non-linear equations and $2 \times 2 \times 2$ integration is performed in each element unless stated otherwise. The proposed models are implemented in FEAP, a general-purpose non-linear finite element code partially documented in [87].

Initially some simulations are carried out on a single-element cube representing a single crystal, in order to exhibit the behavior predicted by the constitutive models under uniaxial loading conditions. The results of subsequent multiscale simulations are compared to experiments on polycrystalline thin-walled tube specimens at quasistatic and dynamic strain rates.

8.1 Texture implementation

The influence of texture, on the response of crystalline materials under mechanical loading, is discussed in Section 3.5. A method of assigning orientations to different crystals in a polycrystal RVE is also proposed. It was mentioned that the relation between the specimen axes and the crystal axes are described in terms of three rotations, by the triplet of angles (α, β, γ) in Roe/Matthies convention [46]. The corresponding rotation tensors $\mathbf{Q}_1$, $\mathbf{Q}_2$ and $\mathbf{Q}_3$ can be used to define the complete rotation tensor $\mathbf{Q}$, whose components relative to the basis $\{\mathbf{p}, \mathbf{q}, \mathbf{r}\}$ are derived in Appendix B.

Upon obtaining the complete rotation $\mathbf{Q}$, the habit plane vectors $\mathbf{b}$ and $\hat{\mathbf{m}}$ defined in Section 3.3.2 are transformed as

$$\mathbf{b}' = \mathbf{Q}\mathbf{b} \quad , \quad \hat{\mathbf{m}}' = \mathbf{Q}\hat{\mathbf{m}} \, , \tag{8.1}$$

where $\mathbf{b}'$ and $\hat{\mathbf{m}}'$ are the habit-plane vectors with respect to the sample basis. These transformed habit plane vectors can be used to compute the transformation deformation gradients,

$\mathbf{F}^t_\alpha$, for each variant α, according to (3.10). Thus, the total transformation deformation of each crystal can be given with respect to the sample basis through (4.2) with the individual $\mathbf{F}^t_\alpha$ appropriately modified.

In the following sections, simulations on cubes and the experimental tube are initially performed for the sheet-texture case, wherein the $<111>$ austenite lattice vector is aligned with the $\mathbf{E}_3$ direction, which coincides with the longitudinal direction of the tube. Since this case involves a single-crystal aligned in a particular direction, these simulations can be done in single-scale. On the other hand, in order to simulate the experimental texture discussed in Section 3.5, multiscale simulations need to be performed according to the procedure elaborated in Chapter 7.

8.2 B2-B19′ phase transformation under quasistatic loading

The simulations below are for boundary-value problems corresponding to a Nitinol specimen undergoing B2-B19′ phase transformation, subject to quasistatic loading. Since under such loading essentially isothermal conditions exist, the simulations in this section are based on the model (4.44).

8.2.1 Single-crystal cube under uniaxial loading

A 10 mm cubic block is fixed along the X_1-, X_2- and X_3-directions on faces with outward normals $-\mathbf{E}_1$, $-\mathbf{E}_2$ and $-\mathbf{E}_3$, respectively, and subjected to a homogeneous normal displacement of up to 0.70 mm at the face with outward normal $\mathbf{E}_1$, see Figure 8.1. The cube is meshed with a single finite-element which represents a Nitinol single-crystal. The single-crystal is chosen to be aligned according to the sheet-texture defined in Section 8.1.

For the austenite-martensite (A-M) phase transformation model, the austenite Young's modulus is chosen to match the experimental stress-strain response in the linear-elastic regime. Thus, the austenite Young's modulus is chosen to be E_a=38.0 GPa. Also, the martensite Young's modulus is taken to be E_m=30.0 GPa and the Poisson's ratio is $\nu = 0.3$ for both phases. In addition, B=0.607 MPa/^{0}C, θ= 22.0 ^{0}C and θ^M_T= -0.5 ^{0}C are used in the simulations. The values of these parameters are chosen based on thin-walled tube experiments on Nitinol in [60]. Further for the single-crystal case, the critical driving forces are set to $\mathcal{F}^c_n = \mathcal{F}^c_r$ =6.5 MPa. The response of the cube undergoing austenite-martensite transformations under tension is depicted by the equivalent stress-strain curves in Figure 8.2. Here, the Mises equivalent stress (7.5) is plotted against the equivalent Lagrange strain

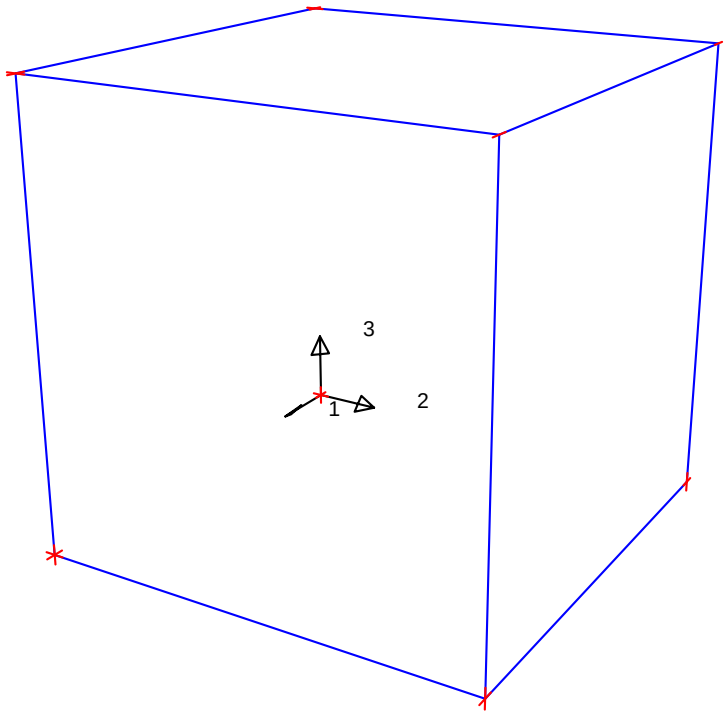

Figure 8.1: *Boundary conditions for the single crystal cube*

given in terms of the components of Green-Lagrange strain as

$$E_{\text{equiv}} = \frac{1}{\sqrt{2}}\left[(E_{11}-E_{22})^2+(E_{22}-E_{33})^2+(E_{33}-E_{11})^2+\frac{3}{2}(E_{12}^2+E_{23}^2+E_{31}^2)\right]^{1/2}. \tag{8.2}$$

The corresponding curve for compression is shown in Figure 8.3. It can be noted that the response hardens for tension while it softens for compression. This texture induced tension-compression asymmetry is known to occur in experiments, see the results in [26, 25].

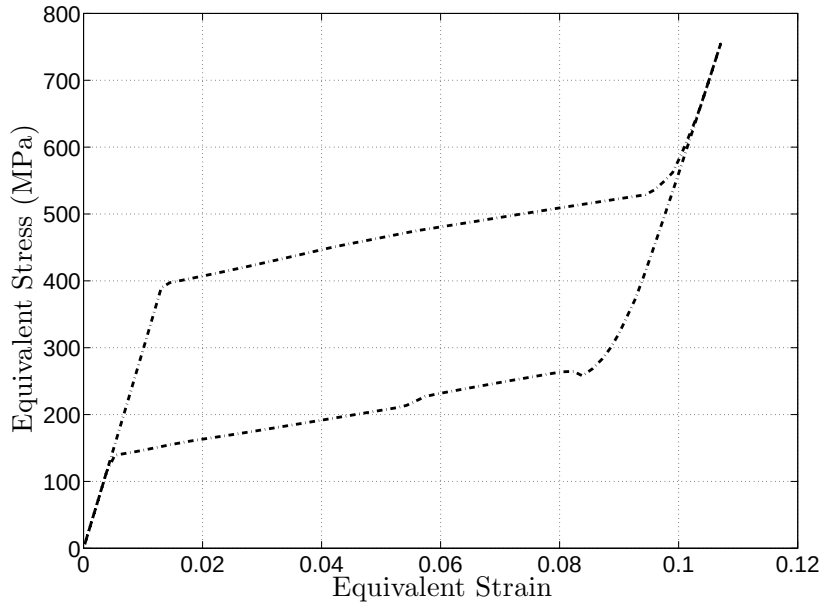

Figure 8.2: *Equivalent stress-strain of cubic block in tension undergoing A-M transformation*

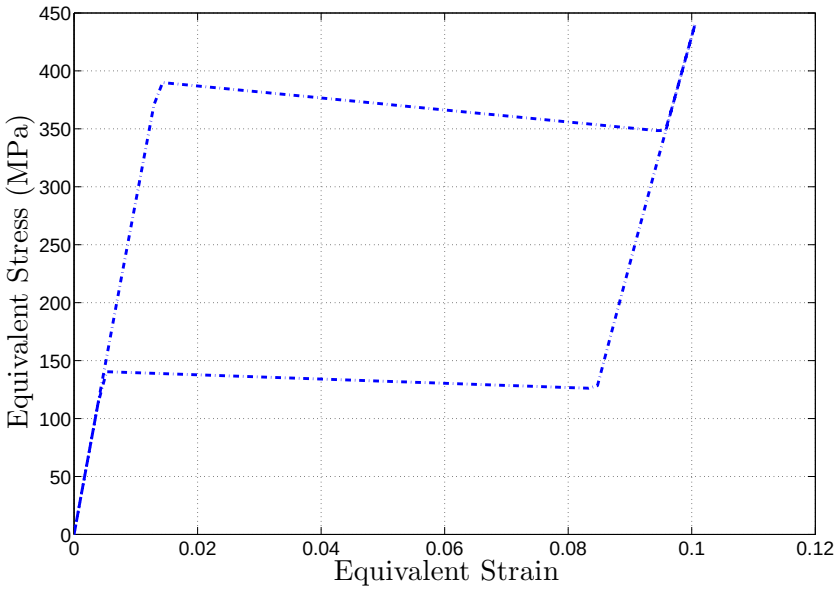

Figure 8.3: *Equivalent stress-strain of cubic block in compression undergoing A-M transformation*

8.2.2 Polycrystalline cube under uniaxial loading

The principal purpose of this simulation is to highlight the asymmetry of the tension/compression response in NiTi polycrystals due to the experimental texture described in 3.5. A 10 *mm* cubic block is fixed along the normal direction at one end and subjected to uniaxial tension/compression by imposing homogeneous normal displacement of up to 0.5 *mm* at the opposite end. In the fine scale, Taylor averaging is used to determine the overall RVE response.

The coarse-scale problem is uniformly discretized into a 7×7×7-element mesh. Figure 8.4 shows the constitutive response of an element at the center of the mesh. Equivalent Cauchy stress (T_{mises}) and equivalent Lagrangian strain (E_{equiv}) at this element, are computed as the average of the respective quantities over the eight Gauss points. The plot depicts the asymmetry of material response in tension and compression due to experimental texture. However, it should be noted that the difference in tension and compression response is less pronounced compared to the single-crystal response in previous section since there is more anisotropy in the sheet-texture.

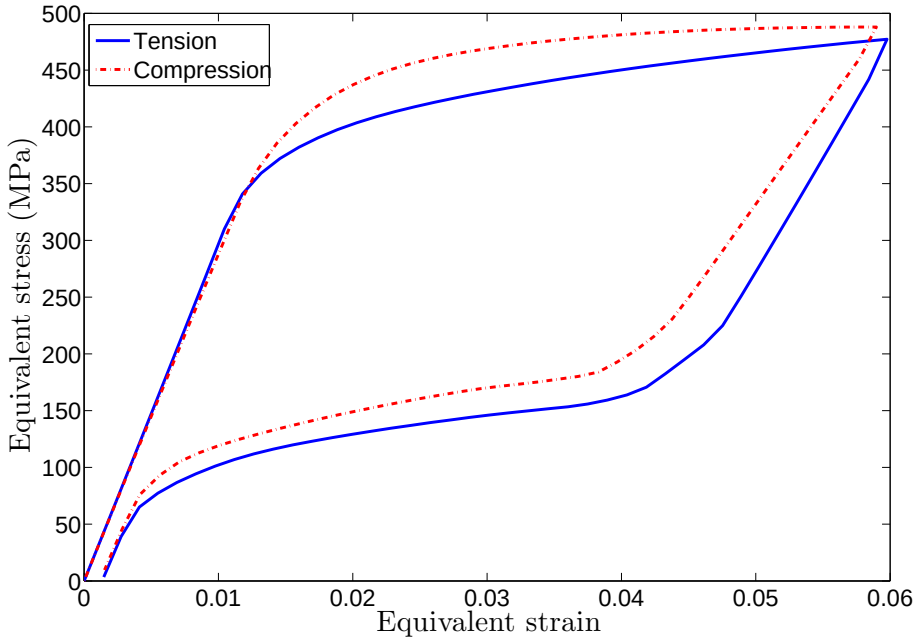

Figure 8.4: *Equivalent stress-strain response of the cubic block in tension and compression*

8.2.3 Thin-walled tube under longitudinal tension

The multiscale model discussed in Chapter 7 is now employed to simulate the response of a thin-walled tube under quasistatic loading in tension up to 6% longitudinal strain. The tube is 75 mm long with inner diameter of 3.9 mm and has a 25 mm gage (middle) section. The thickness of the tube is 0.375 mm in the grip sections while it was reduced to 0.20 mm in the gage section. This reduction of thickness in the gage section is meant to localize failure of the tube within this zone. Details of the experimental procedure can be found in [60] and comparisons to a single crystal-based model are contained in [43]. The orientation of the crystal in that work was chosen based on the sheet-texture discussed in Section 8.1. Here, the experimental results are compared to multiscale simulations based on the actual texture. The geometry and loading of the tube are fully described in [43]. Quasi-static loading at a rate of 10^{-4}/sec is employed to ensure nearly isothermal conditions. As discussed in [79], to account for the higher stresses observed to initiate transformation under quasi-static conditions, a higher value of critical driving force is chosen for the nucleation regime as opposed to the propagation regime. Specifically, the critical driving forces are given by $\mathcal{F}_n^c$ =10.0 MPa for the nucleation regime when the martensite volume fraction is less or equal to 0.05 (assumed to be the martensitic nucleus size), and $\mathcal{F}_r^c$=6.5 MPa for the propagation regime. All other parameters are chosen as in Section 8.2.1.

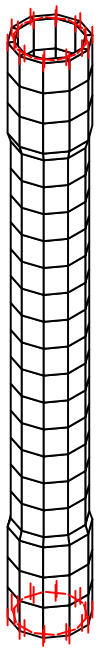

Figure 8.5: *Finite element mesh and boundary conditions for a thin-walled tube in tension*

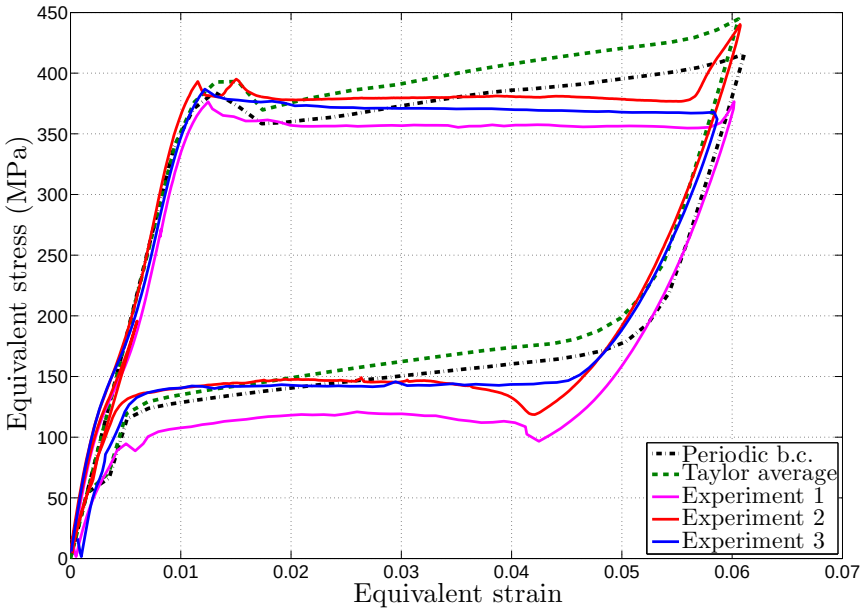

Figure 8.6: *Comparison of TA and PBC stress response of thin-walled tube in tension*

Since the proposed multiscale approaches are computationally intensive, a relatively small mesh with 220 eight-node brick elements is employed to model the tube in the coarse scale, see Figure 8.5. It is fixed in the longitudinal and circumferential directions at both ends to simulate the effect of the grips. To further reduce the computational complexity, a one-point integration method with stabilization is adopted, following the work in [11]. Appealing to the statistical approach for the determination of the RVE in Section 7.1, each Gauss point (hence, in this case, each element) is comprised of 6^3 crystals (each crystal represented by an element) for the cases of Taylor averaging and displacement boundary conditions. In contrast, the RVE size for periodic boundary conditions is only $4^3(=64)$ crystals. This difference is justified by the fact that periodic boundary conditions generally emulate the polycrystal behavior more accurately than the Taylor averaging and periodic boundary conditions. Each crystal in the RVE is taken to have dimension of $25\mu m$, consistently with the experimental observations. In the gauge (middle) area, there are approximately 8-15 crystals through the thickness, which justifies the use of a single coarse-mesh element through the thickness of the tube.

The equivalent stress vs. equivalent strain response obtained by Taylor averaging (TA) and periodic boundary condition (PBC) simulations are compared to the experimental measurements in Figure 8.6. Likewise, the response obtained by Taylor averaging and displacement boundary condition (DBC) are compared to experiments in Figure 8.7. Clearly, the stresses and strains are inhomogeneous owing both to the form of the boundary conditions

and the texture. Therefore, the stresses and strains reported in the preceding figures are

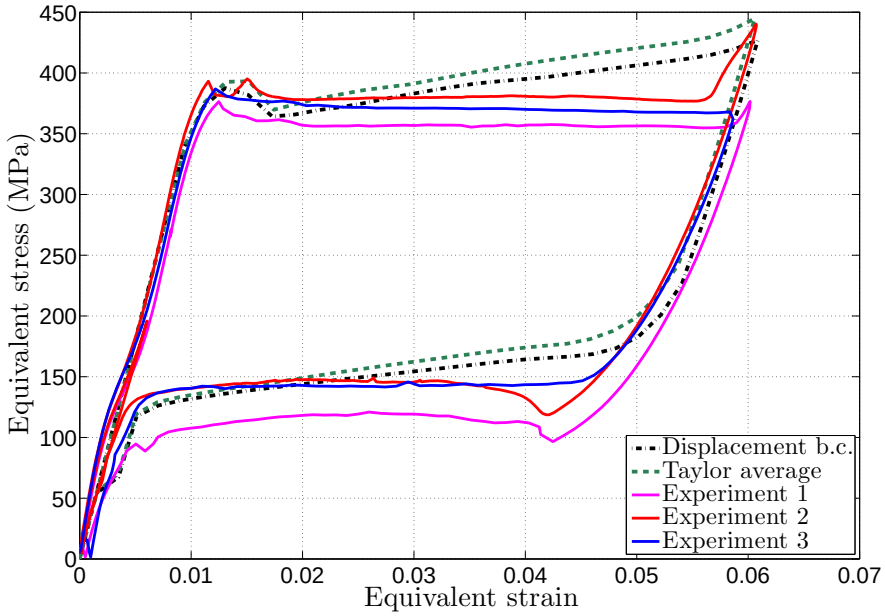

Figure 8.7: *Comparison of TA and DBC stress response of thin-walled tube in tension*

determined in an average sense consistently with the experimental procedure described in [60] and elaborated upon in [43]. In particular, the average equivalent Cauchy stress T_{eq} and equivalent Lagrangian strain E_{eq} are determined as

$$T_{eq} = \sqrt{\bar{T}_t^2 + 3\bar{T}_s^2}\ , \qquad E_{eq} = \sqrt{\bar{E}_t^2 + \frac{4}{3}\bar{E}_s^2}\ , \tag{8.3}$$

where $\bar{T}_t$ and $\bar{T}_s$ denote the average tensile and shearing Cauchy stress, while $\bar{E}_t$ and $\bar{E}_s$ the average tensile and shearing Lagrangian strain. Considerable hardening behavior can be noted in the constitutive response predicted using Taylor averaging, when compared to both experiments and simulations with the other two sets of boundary conditions. As expected, Taylor averaging yields an upper bound of stress response, while the periodic boundary conditions lead to answers which appear to be closest to the experiments. The normal stress along the longitudinal axis of the tube and the martensite volume fraction are shown at maximum tension in Figures 8.8 and 8.9, respectively, for periodic boundary conditions.

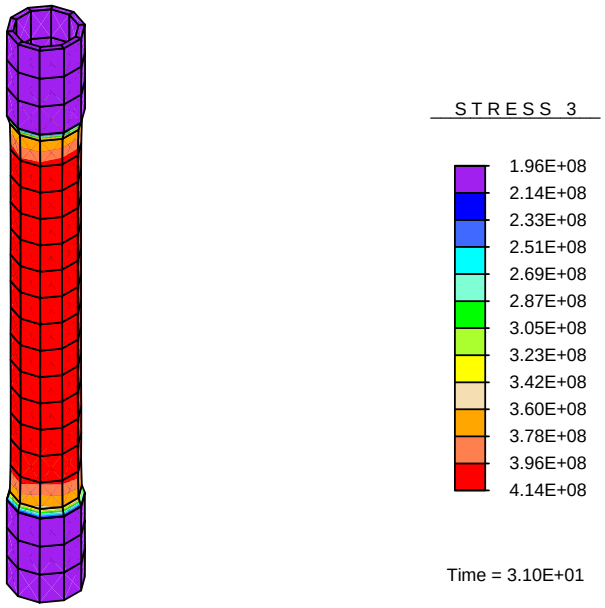

Figure 8.8: *Normal stress component at 6% equivalent strain for RVE with PBC*

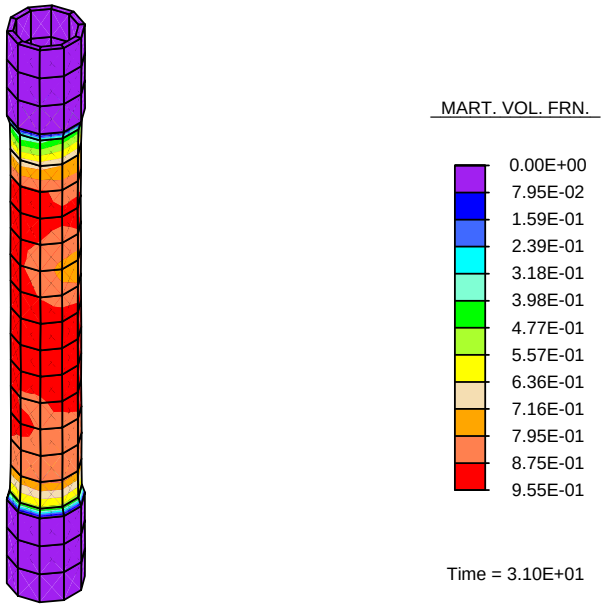

Figure 8.9: *Transformed martensitic volume fraction at 6% equivalent strain for RVE with PBC*

8.3 B2-R-B19′ phase transformation under quasistatic loading

The simulations below are for boundary-value problems corresponding to Nitinol specimen undergoing B2-R-B19′ phase transformation, due to quasistatic loading. The model (5.22) in Chapter 5 is employed for the simulations in this section.

8.3.1 Single-crystal cube under uniaxial loading

A cube with the same dimensions and boundary conditions as in Section 8.2.1, and subjected to the same loading, is simulated here to show the predictive capacity of the model for B2-R-B19′ phase transformation. In this case, the austenite and martensite moduli are chosen to be E_a=55.0 GPa and E_m=20.0 GPa respectively. These values are different from the values used in the model for B2-B19′ phase transformation, since the model for B2-R-B19′ transformation takes into account R-phase transformation in the apparent linear-elastic region. However the Poisson's ratio is kept same as above. In addition, B_R=0.35 MPa/^{0}C, B_M=0.607 MPa/^{0}C, θ_T^R= 20.85 ^{0}C, θ_T^M= -0.5 ^{0}C and θ = 22.0^{0}C are used in the simulations. Finally, the critical driving forces are set to $\mathcal{F}^{c,R}$ =0.11 MPa and $\mathcal{F}^{c,M}$ =6.5 MPa.

The response of the cube undergoing AR, AM_1 and RM_2 transformations under tension is depicted by the equivalent stress-strain curves in Figure 8.10. The corresponding curves for compression are shown in Figure 8.11. The plot shows how the plateau for AR transformation occurs at relatively low stress and is substantially narrower than the one for RM_2 transformation. Also, the hysteresis of AR transformation is shown to be much smaller than that of the RM_2 transformation. The model is able to capture both the hystereses due to the AR and RM_2 transformation as demonstrated in the plots for the two displacements of 0.11 mm and 0.70 mm, respectively. Further, comparing the stress plateaus for tension and compression with the austenite-martensite phase transformation model 8.2.1, it is apparent that RM_2 transformation continues up to larger strains before the phase transformation completes and martensite starts to load elastically.

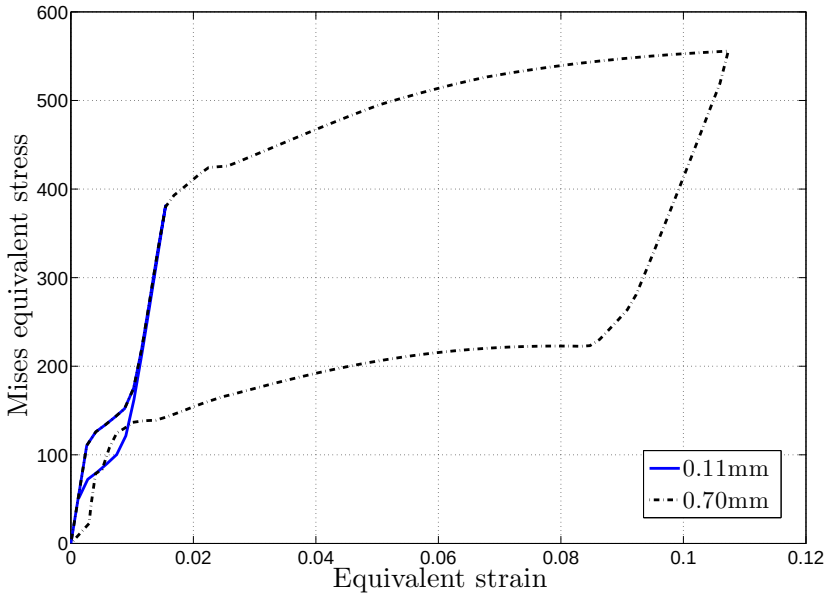

Figure 8.10: *Equivalent stress-strain of cubic block in tension undergoing AR and RM_2 transformations*

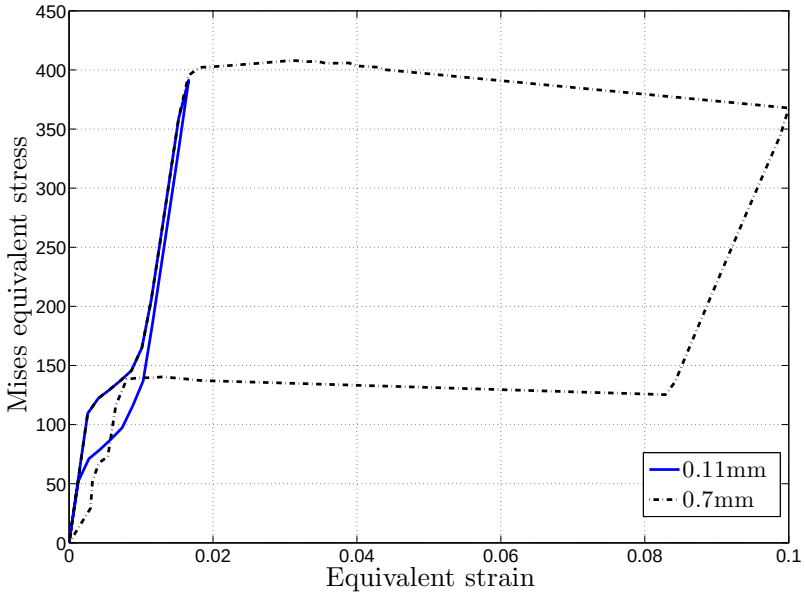

Figure 8.11: *Equivalent stress-strain of cubic block in compression undergoing AR and RM_2 transformations*

8.3.2 Thin-walled tube under longitudinal tension

The B2-R-B19′ phase transformation model is applied in a multiscale setting, to simulate the quasistatic tensile loading of thin-walled tube discussed in Section 8.2.3.

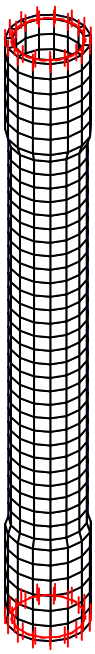

Figure 8.12: *Finite element mesh and boundary conditions for a thin-walled tube in tension*

Initially, a single-scale solution is obtained by assuming that each finite element represents a single crystal and that all crystals have the same orientation according to the sheet-texture, as described in Section 8.2.3. Here too, such a simulation is carried out first with the B2-R-B19′ phase transformation model. The tube mesh is constructed with 630 eight-node brick elements see Figure 8.12. The predicted stress response shown in Figure 8.13 includes a flat plateau when the tube undergoes R-B19′ transformation that matches the experimental measurements. However, the single-scale model over-accentuates the deviation from the linearly elastic response due to B2-R transformation. Also, the predicted transition from the B2 (or R) to martensite phase is smoother than that measured in the experiments along with much lower stress plateau during unloading. Figure 8.14 shows the normal stress in the axial direction of the tube.

Subsequently, a multi-scale formulation of the proposed model is implemented to resolve the experimental texture. Here the macroscale mesh has 220 eight-node brick elements, while the microscale cubic RVE had 4^3 elements and is subjected to periodic boundary conditions, as in Section 8.2.3. Also, similar to the B2-B19′ model, the critical driving force during nucleation of martensite is chosen as $\mathcal{F}^{c,M} = 9.0$ MPa, while the same during propagation

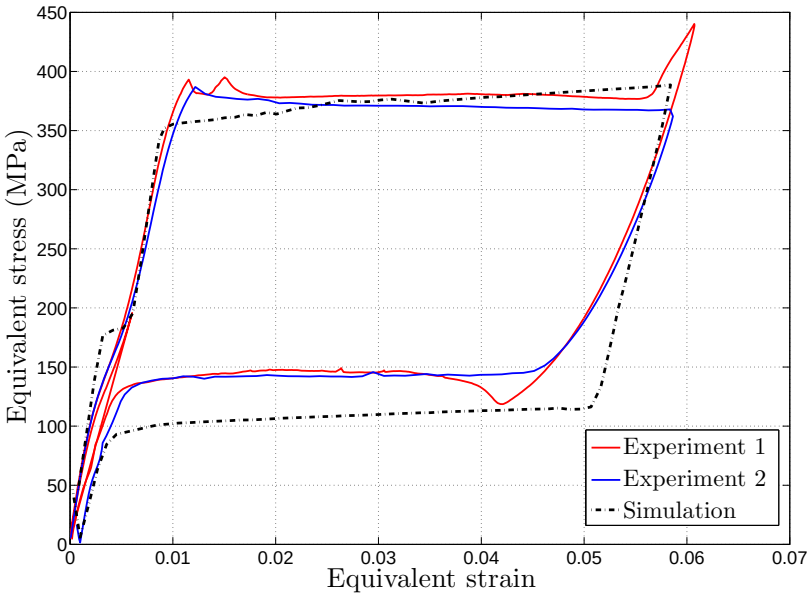

Figure 8.13: *Equivalent stress vs. strain from experiments and sheet-texture simulation for the tube in tension*

of the martensite phase boundary is taken to be $\mathcal{F}^{c,M} = 6.2$ MPa. This differentiation is not needed for R-phase nucleation, since the R-phase effects only a minor distortion to the austenite lattice and its initial accommodation does not have a high energy barrier. This choice is also supported by experiments, where no increase in the stress during R-phase transformation is observed. All other parameters are chosen as in Section 8.3.1.

The numerical predictions for stress response are compared in Figure 8.15 to the experimental measurements. Both the deviation from linearity due to the R-phase and the jump in the stress due to the initiation of the martensite transition are well represented by the model. The normal stress along the longitudinal axis of the tube at the onset and completion of martensitic transformation are shown in Figure 8.16. In Figure 8.17, the R-phase volume fractions are shown at the onset and completion of martensitic transformation. This illustrates how the R-phase volume fraction in the gauge section is decreased as the R-phase is annihilated in favor of martensite phase with increased loading. The martensite volume fraction at these two stages is displayed in Figure 8.18.

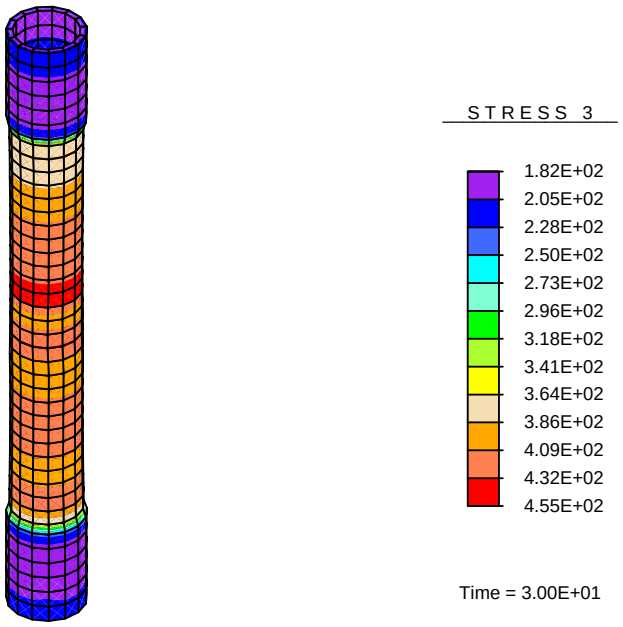

Figure 8.14: *Normal stress distribution along longitudinal axis at 6% tensile strain from the sheet-texture simulation*

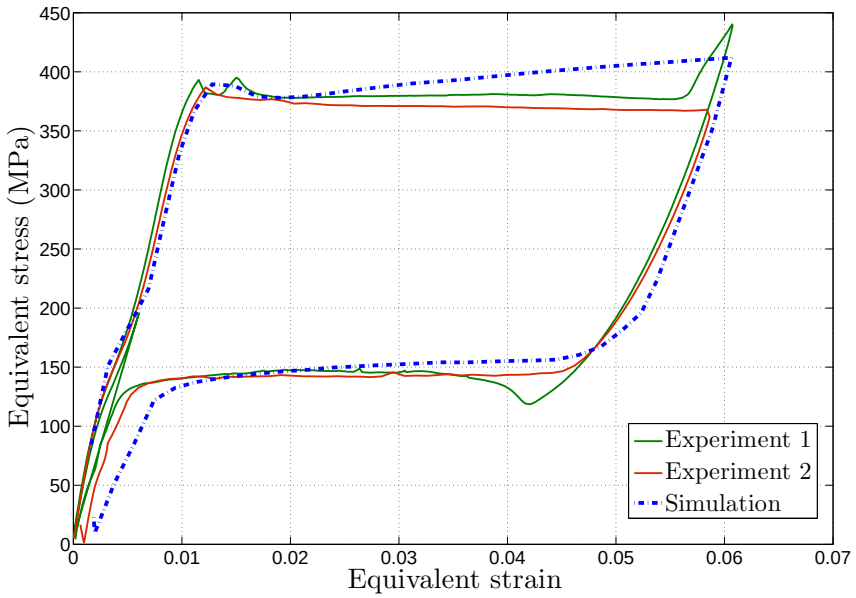

Figure 8.15: *Equivalent stress vs. strain from experiments and multiscale simulation for the tube in tension*

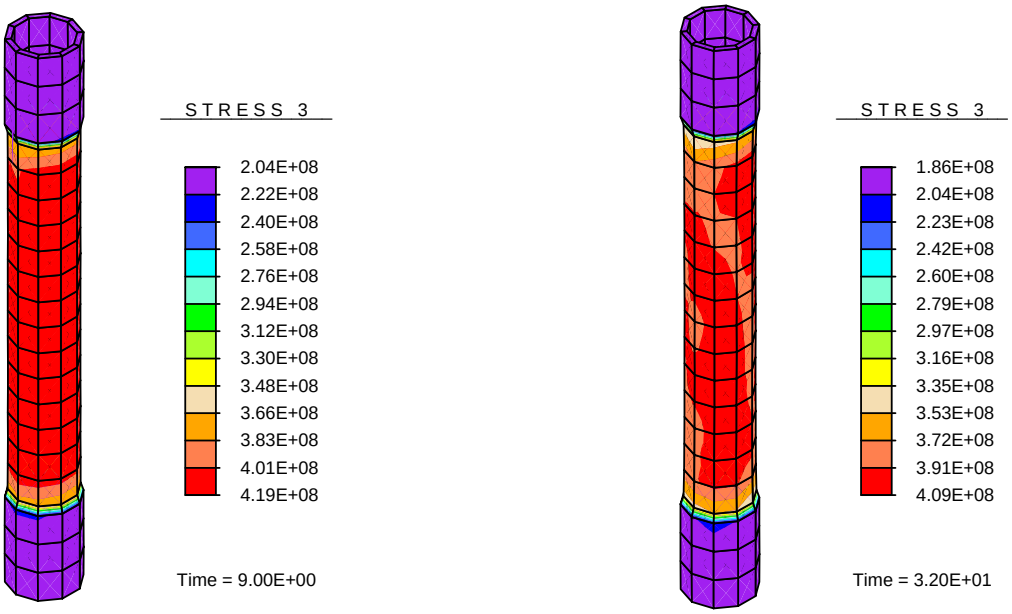

Figure 8.16: *Normal stress distribution along the longitudinal direction at 1% and 6% tensile strains from the multiscale simulation*

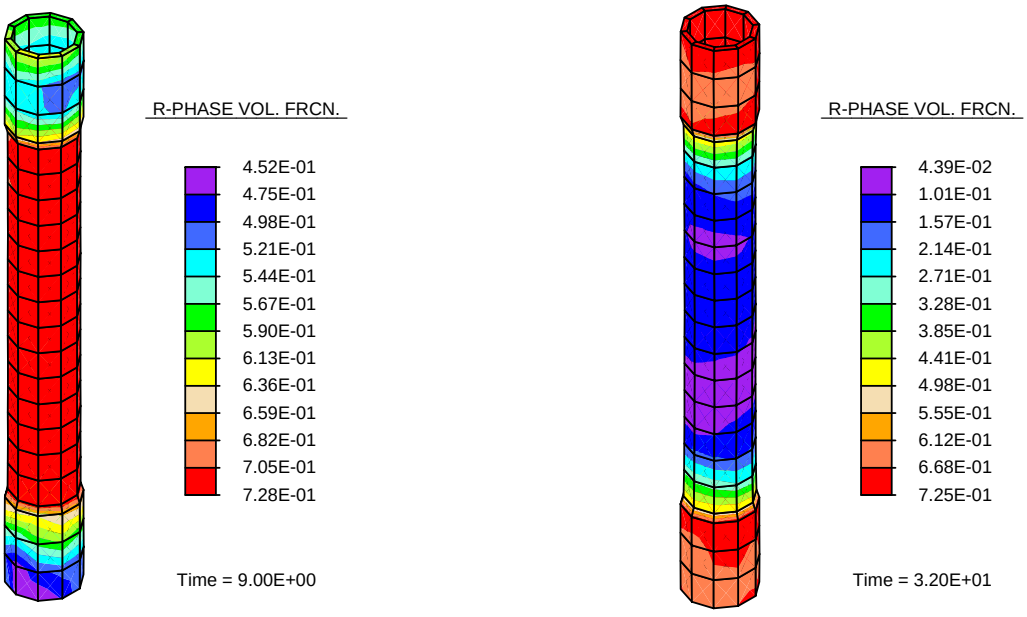

Figure 8.17: *R-phase volume fractions at 1% and 6% tensile strains from the multiscale simulation*

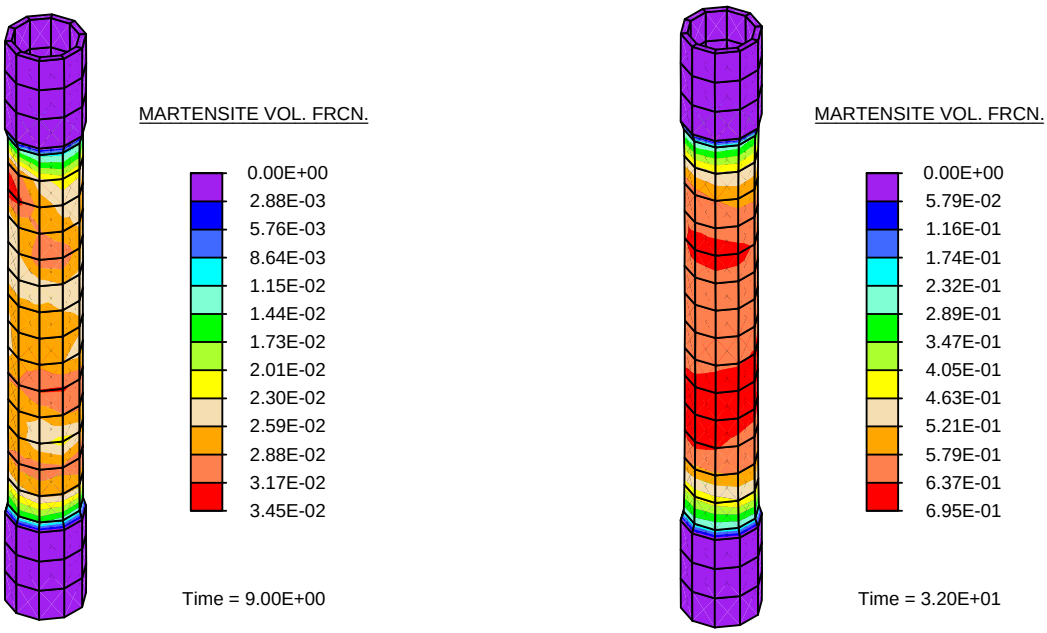

Figure 8.18: *Thin-walled tube in tension: Martensite volume fractions at 1% and 6% tensile strains from the multiscale simulation*

8.3.3 Thin-walled tube under simultaneous tension-torsion

The same tube discussed in Section 8.3.2 is also subjected to simultaneous tension-torsion loading. The grips at the ends of the tube applied up to 6% longitudinal strain under tension and 2% shear strain due to torsion. The material properties used in the simulation are given in the Section 8.3.2. Also, the mesh size is kept the same as in Section 8.2.3. The stress response is compared in Figure 8.19 to the experiments. The figure shows that the austenite-R-phase transformation yields a significant plateau during loading compared to the tension loading case.

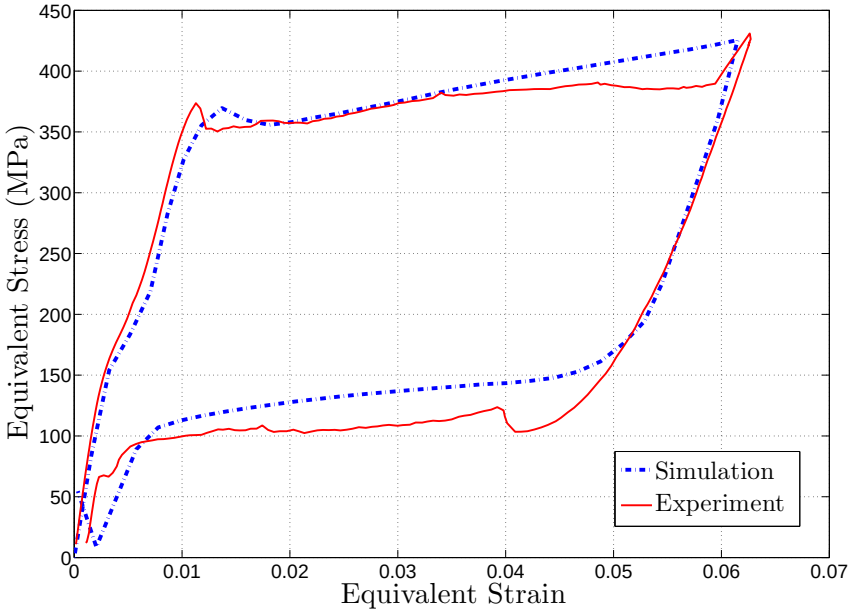

Figure 8.19: *Equivalent stress vs. strain from experiments and multiscale simulation for tube in simultaneous tension-torsion*

8.4 B2-B19′ phase transformation under dynamic loading

In earlier sections, comparisons are made between experiments on a thin-walled tube and simulations at quasistatic loading, rates where essentially isothermal conditions existed. In this section the thermomechanical models developed in Chapter 4, are tested through simulations for tube experiments at different strain rates [49]. In particular, the simulation results for strain rates of 10^{-4}/s and 10^{-3}/s are presented in this work. Since the higher

strain rates involve more substantial temperature changes of the specimen, both temperature and stress response are monitored in these experiments.

The tube used in this set of experiments has an inner diameter of 3.47 mm and thickness of 0.45 mm throughout its length of 76.2 mm. The uniaxial stress is estimated as applied load divided by the undeformed area and the strain is measured by a strain gage in the middle section of the tube. The temperature is recorded through a sensor attached to the middle of the tube. In simulations, the tube is taken to be entirely fixed at both ends, to reproduce the effect of the much stiffer grips. However, it is difficult to account for the effects of all the heat transfer mechanisms present in these experiments. In this work, conduction and convection heat transfer have been accounted for. The ends of the test section of the tube are assumed to be at the ambient temperature due to the large grips acting as heat sinks, thus resulting in conduction of heat between the tube and the grips. In addition, the lateral surface of the tube are also exposed to ambient conditions which resulted in convection heat transfer between the tube and the surrounding air. Convection coefficients depend on the placement of the specimen (here, vertical) and are affected by its temperature, owing to the different air flow patterns generated in the vicinity of the tube. A standard assumption is that the normal heat flux can be adequately approximated as $q_n = h(\theta - \theta_0)^n$, see [40]. Here, $\theta_0 = 295$ K, while the value of the exponent is chosen to be $n = 1.25$ based on the geometry and expected temperature of the tube [40, Chapter 7]. The coefficient h also varies with temperature since it affects the properties of the air film surrounding of the tube. By way of simplification, the value of h is assumed constant and equal to 10 for $\theta > \theta_0$ and 80 for $\theta \leq \theta_0$. These values are chose to match the history of tube temperature for the strain rate of 10^{-3}/s. The same parameters are used for the strain rate of 10^{-4}/s and the resulting temperature response appeared to match well the experiments.

The material parameters used for Nitinol are taken as follows: The austenite and martensite phases are assumed to be isotropic with respective Young's moduli $E_a = 60.0$ GPa and $E_m = 20.0$ GPa, while the Poisson ratio is $\nu = 0.3$ for both phases. Likewise, the thermal conductivity and the thermal expansion are taken to be isotropic and equal to $K = 18$ W/(m K) and $A = 11 \times 10^{-6}$ /K, respectively, while the volumetric heat capacity is $c = 5.8$ MJ/(m^3 K).

8.4.1 Sheet-textured tube under longitudinal tension

Initially, the experimental results are compared with single-scale simulations where the crystals are assumed oriented according to sheet-texture, as in Section 8.2.3. The thermodynamic constants for the martensite variants in the "FT" model are chosen as follows: B = 0.75 MPa/K, $\theta_T = 268$ K and $\mathcal{F}_c = 3.5$ MPa. On the other hand, for the "ET" model they are chosen as: B = 0.775 MPa/K, $\theta_T = 268$ K and $\mathcal{F}_c = 5.0$ MPa. The thermodynamic constants B and $\mathcal{F}_c$ are chosen to match the experimental results, while θ_T is estimated from differential scanning calorimetry data.

The tube mesh is constructed with 420 eight-node brick elements, see Figure 8.20. The

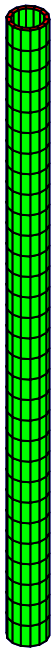

Figure 8.20: *Tube mesh comprising eight-node brick elements.*

effect of convection is incorporated by superposing 4-node quadrilateral elements with a temperature degree-of-freedom to the outer and inner surfaces of the tube. In Figure 8.21 and Figure 8.22, the uniaxial stress-strain response of the tube under tension at strain rates 10^{-4}/sec and 10^{-3}/sec respectively are compared. As expected, both experiments and theory predict that the transformation plateau hardens with increasing strain rates due to the higher temperatures attained in the specimen. However, for the higher strain rate both models predict stiffer response than the experiments during the phase transformation. This is possibly due to the temperature-dependence of the material properties, which is unaccounted for in the models. Figure 8.23 and Figure 8.24 show the temperature history at the middle of the tube for the 10^{-4} and 10^{-3} strain-rates, respectively. It is seen that both models are quite close to experiments and can predict the maximum and minimum temperatures quite accurately. The only deviation of the models from the experiment is in some part of the loading where the formation of R-phase and subsequent transformation to martensite may take place that has not been modeled here. An explicit account of R-phase in the model entails significant added complexity due to the dependence of the rhombohedral angle on temperature as discussed in Chapter 5. Further, Figure 8.25 shows the temperature distribution over the tube at end of loading for the two strain rates. As expected, the temperatures are generally lower for the lower strain rate. Also, the effect of conduction is more pronounced in the lower strain-rate case due to ambient-temperature boundary condition at the ends of the tube, and leads to a more heterogeneous distribution of

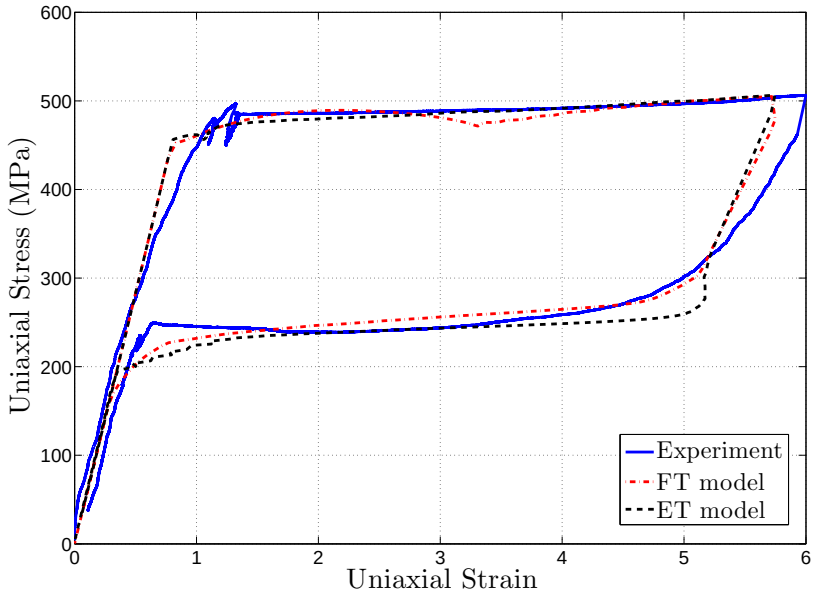

Figure 8.21: *Comparison of stress response under longitudinal tension at* 10^{-4}*/sec strain rate*

temperature. In contrast, the temperature is affected more significantly by convection in the higher strain rate case, and as a result, the temperature distribution is more homogeneous at the end of loading. Figure 8.26 illustrates the comparison of longitudinal stress distributions at the end of loading for the two strain rates. It is noted that the stresses are quite uniform for both rates, although their values are clearly different. Both temperature and stress results are obtained using the "FT" model, although they are not appreciably different for the "ET" model. Lastly, Figure 8.27 shows the martensitic volume fractions at the end of loading using the "FT" model. It is observed that the martensite transformation is more near the grips than in the middle section of the tube due to the lower temperature levels near its ends. Also, the volume fractions for the strain rate of 10^{-4}/sec are overall higher than those at the strain rate of 10^{-3}/sec, since the lower temperature attained for slower loading is more conducive to transformation, as can be readily concluded from (4.34) and (4.35).

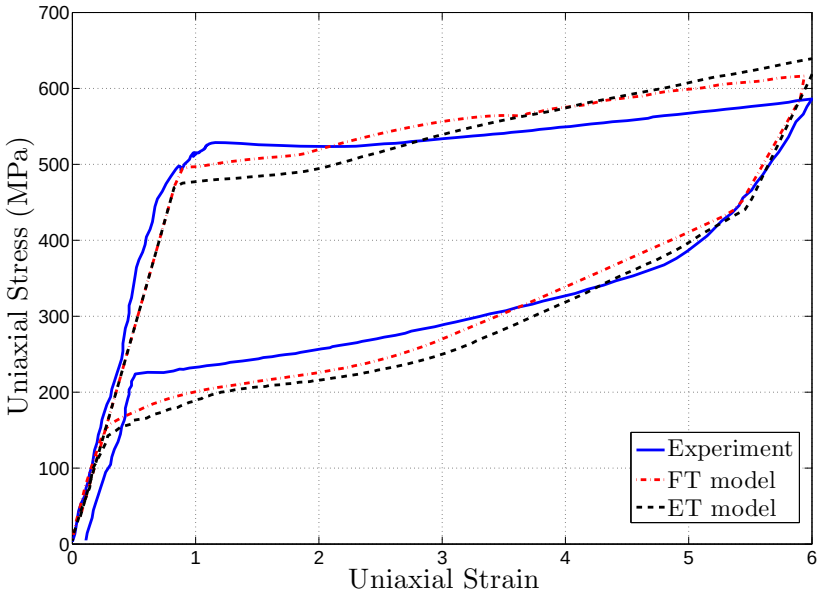

Figure 8.22: *Comparison of stress response under longitudinal tension at* 10^{-3}*/sec strain rate*

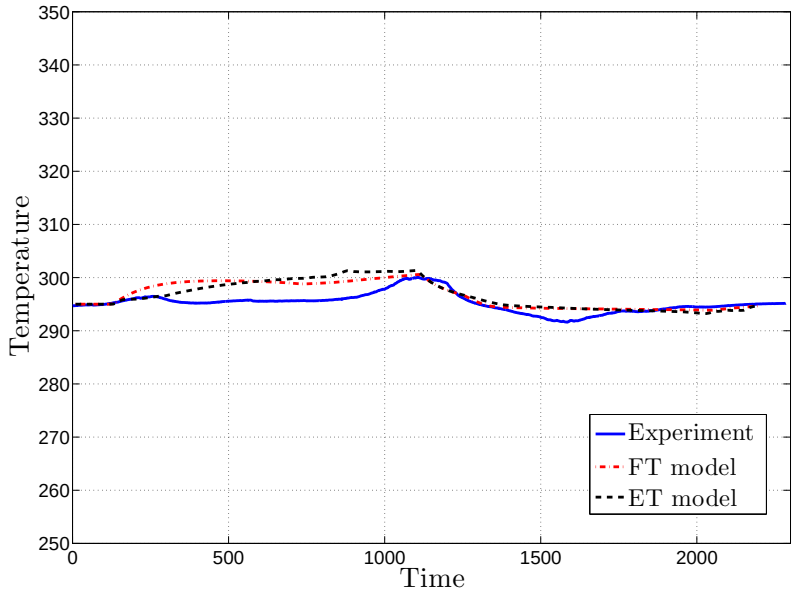

Figure 8.23: *Comparison of temperature history at middle of tube at* 10^{-4}*/sec strain rate*

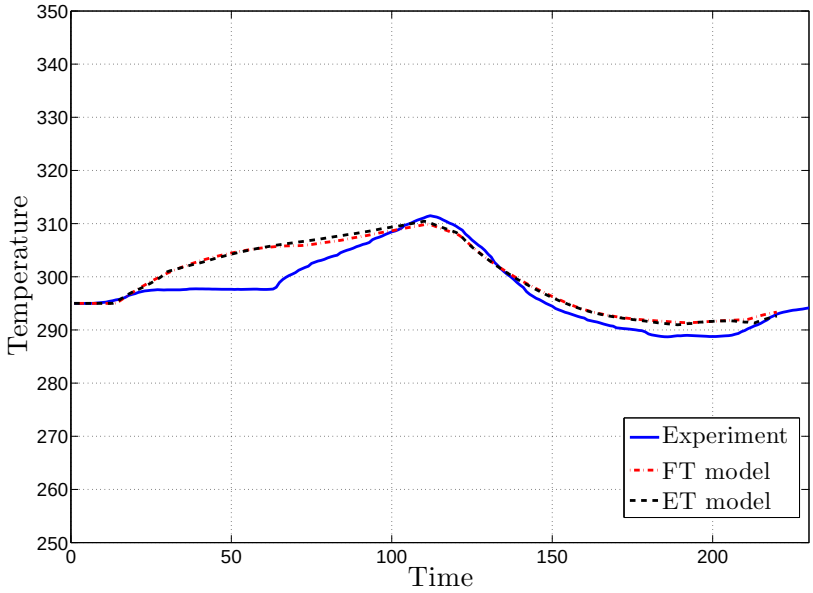

Figure 8.24: *Comparison of temperature history at middle of tube at* $10^{-3}/sec$ *strain rate*

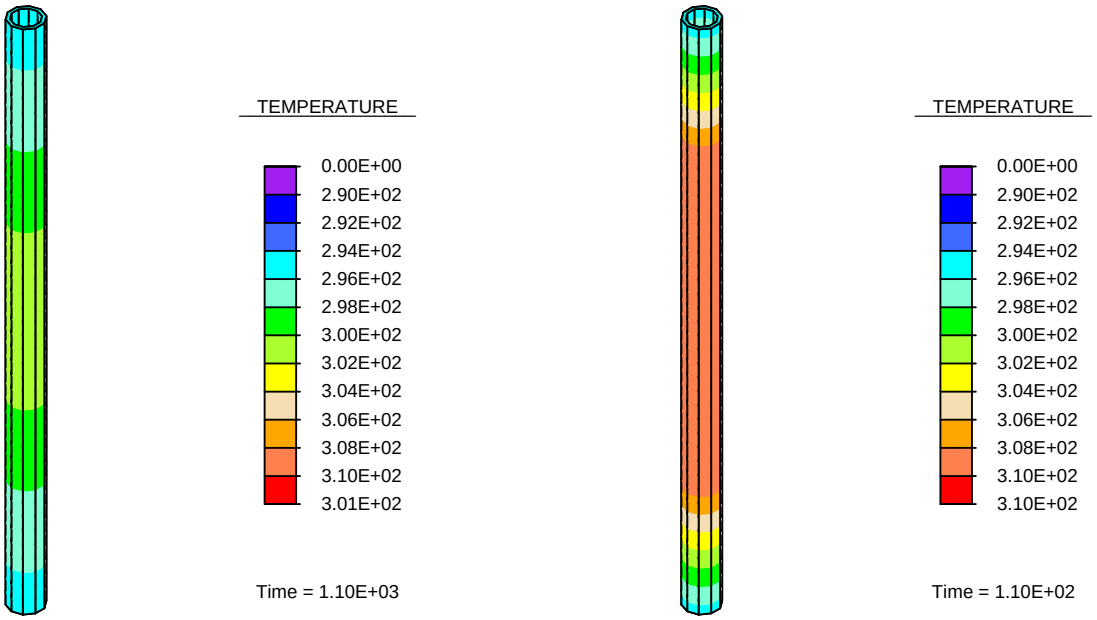

Figure 8.25: *Temperature distributions for* $10^{-4}/sec$ *and* $10^{-3}/sec$ *strain rates*

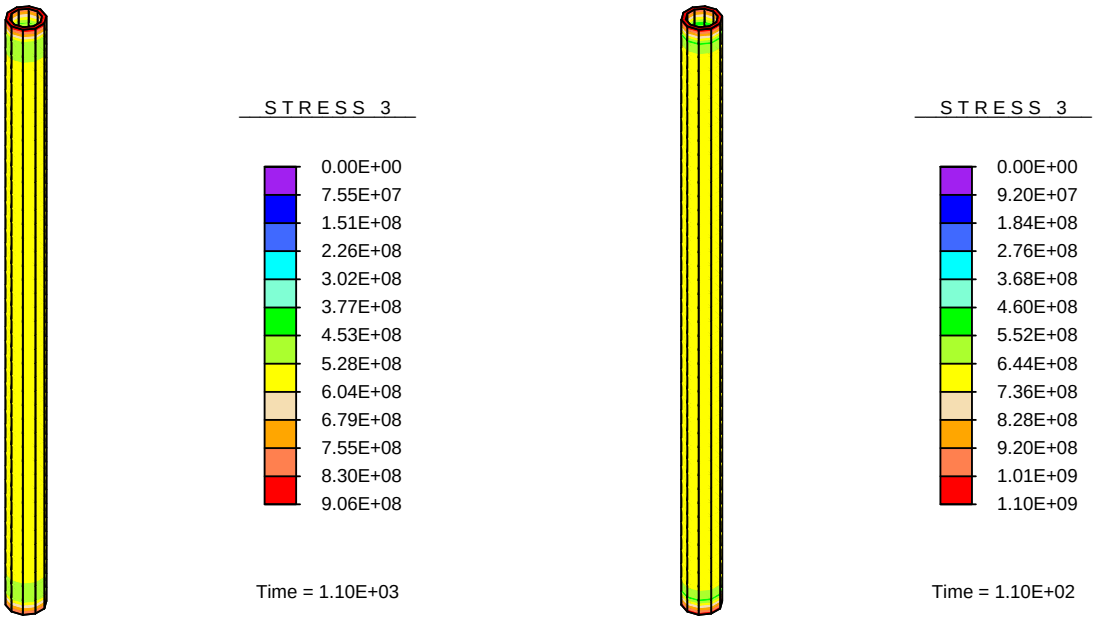

Figure 8.26: *Longitudinal stress distributions for* $10^{-4}/sec$ *and* $10^{-3}/sec$ *strain rates*

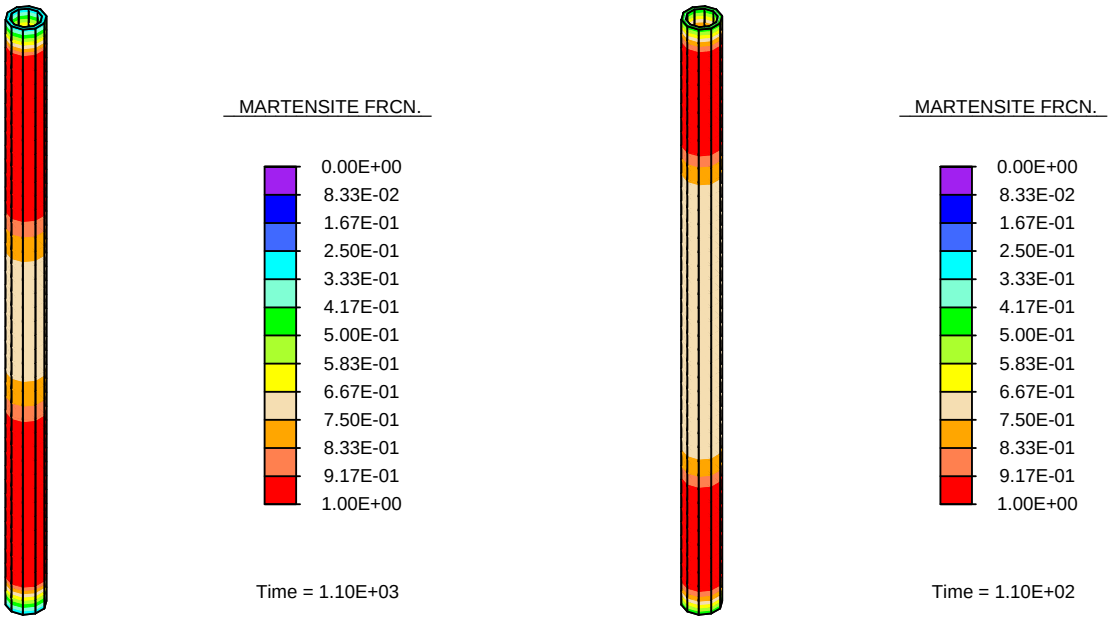

Figure 8.27: *Martensite volume fractions for* $10^{-4}/sec$ *and* $10^{-3}/sec$ *strain rates*

8.4.2 Textured tube under longitudinal tension

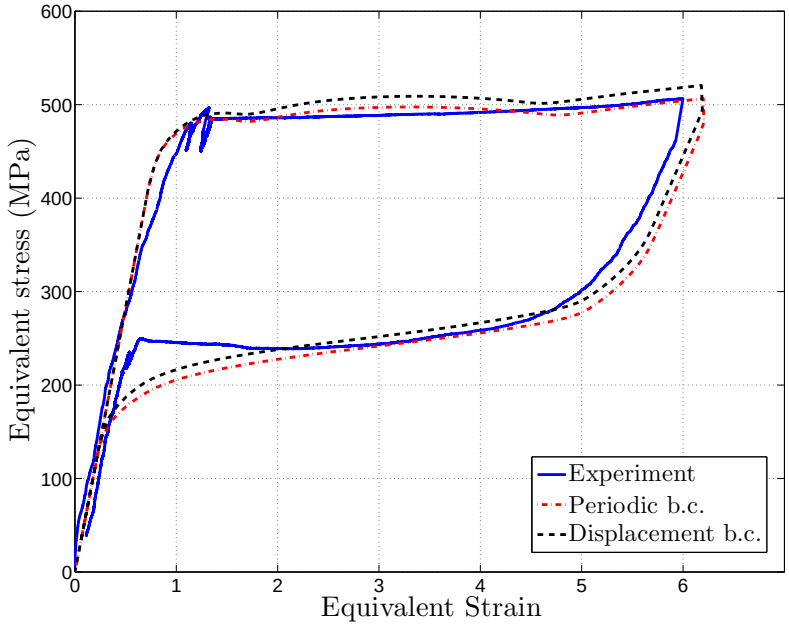

Figure 8.28: *Comparison of stress response under longitudinal tension at* 10^{-4}*/sec strain rate*

The multiscale approach for thermomechanical problems discussed in Section 7.3 is now employed to simulate the response of the polycrystalline Nitinol tube. The texture of polycrystalline Nitinol is modeled as discussed in Section 8.1. The "FT" model is used to obtain the constitutive response at single-crystal level in these simulations. The thermodynamic constants for the martensite variants in this case are chosen to be B = 0.75 MPa/K, $\theta_T = 271$ K and $\mathcal{F}_c = 3.5$ MPa. Further, here the critical driving force for the nucleation regime, when the martensite volume fraction is less or equal to 0.10, in chosen as $\mathcal{F}_n^c$ =6.0 MPa. Since the proposed multiscale approaches are computationally intensive, a relatively small mesh with 180 eight-node brick elements is employed to model the tube in the coarse scale which features $2 \times 2 \times 2$ integration at the two scales. Each Gauss point at macroscale is comprised of an RVE containing 4^3 crystals for displacement boundary condition. In contrast, the RVE for periodic boundary condition is chosen to have 3^3 crystals.

In Figure 8.28 and Figure 8.29, the uniaxial stress-strain response of the tube under tension at strain rates 10^{-4}/sec and 10^{-3}/sec, respectively, are compared. Both the displacement and periodic boundary conditions gives results that match the experiments quite well, but it can be seen that the displacement boundary condition stresses are higher compared to those of the periodic boundary condition. Figure 8.30 and Figure 8.31 show the

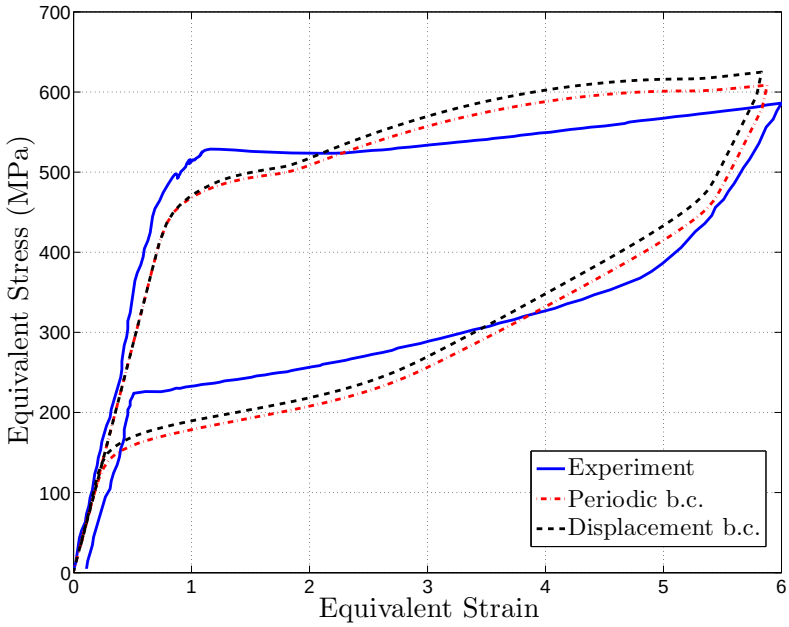

Figure 8.29: *Comparison of stress response under longitudinal tension at* 10^{-3}*/sec strain rate*

temperature history at the middle of the tube for the 10^{-4} and 10^{-3} strain-rates, respectively. It is seen that both models are quite close to experiments and can predict the maximum and minimum temperatures quite accurately. For the periodic boundary condition, Figure 8.32 shows a comparison of the longitudinal stress distribution for the two strain rates. It is observed that, although the stresses are mostly uniform over the tube, there is a region near the end of the tube where stresses are lower than that in the remaining parts. This is possibly due to the combined effects of the total deformation being constrained by the grips, and the transformation deformation being higher as a result of more martensite transformation near the grips. Figure 8.33 compares the martensitic volume fractions at the end of loading and the conclusions are similar to the sheet texture case.

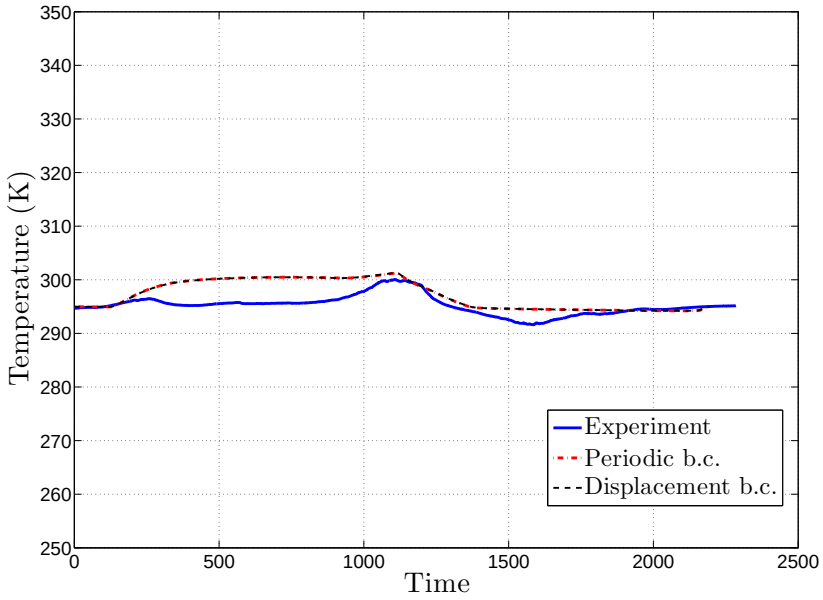

Figure 8.30: *Comparison of temperature history at middle of tube at* 10^{-4}*/sec strain rate*

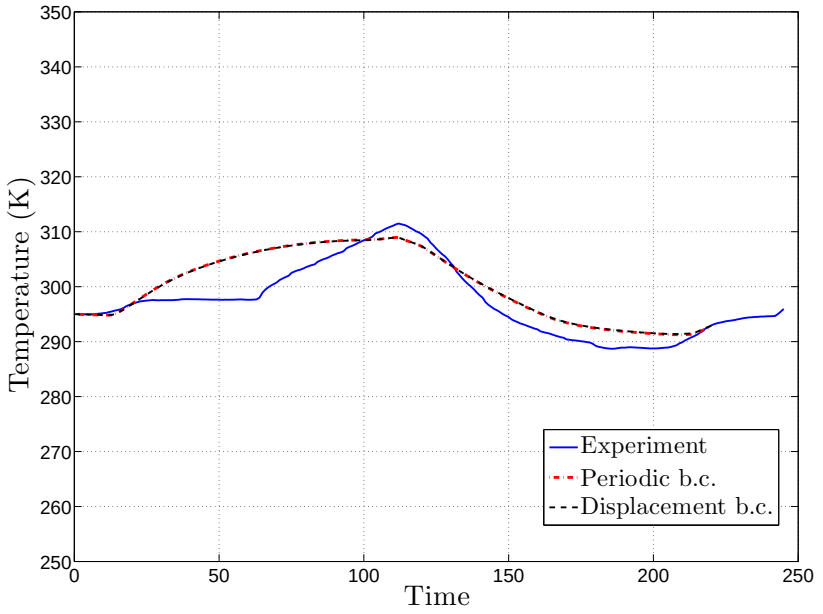

Figure 8.31: *Comparison of temperature history at middle of tube at* 10^{-3}*/sec strain rate*

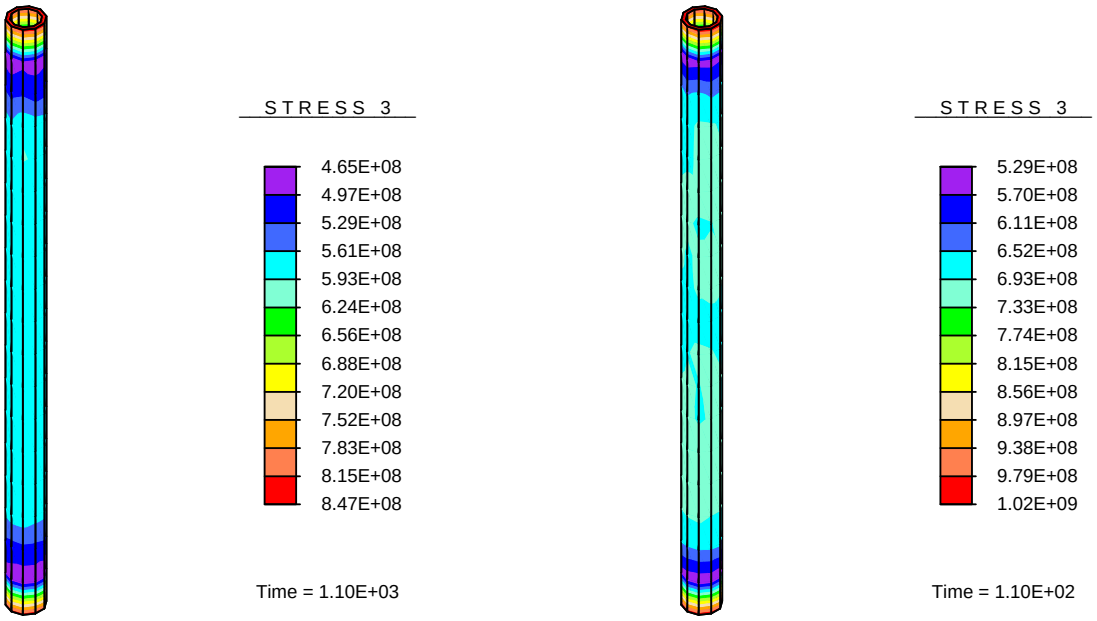

Figure 8.32: *Longitudinal stress distributions for* $10^{-4}/sec$ *and* $10^{-3}/sec$ *strain rates*

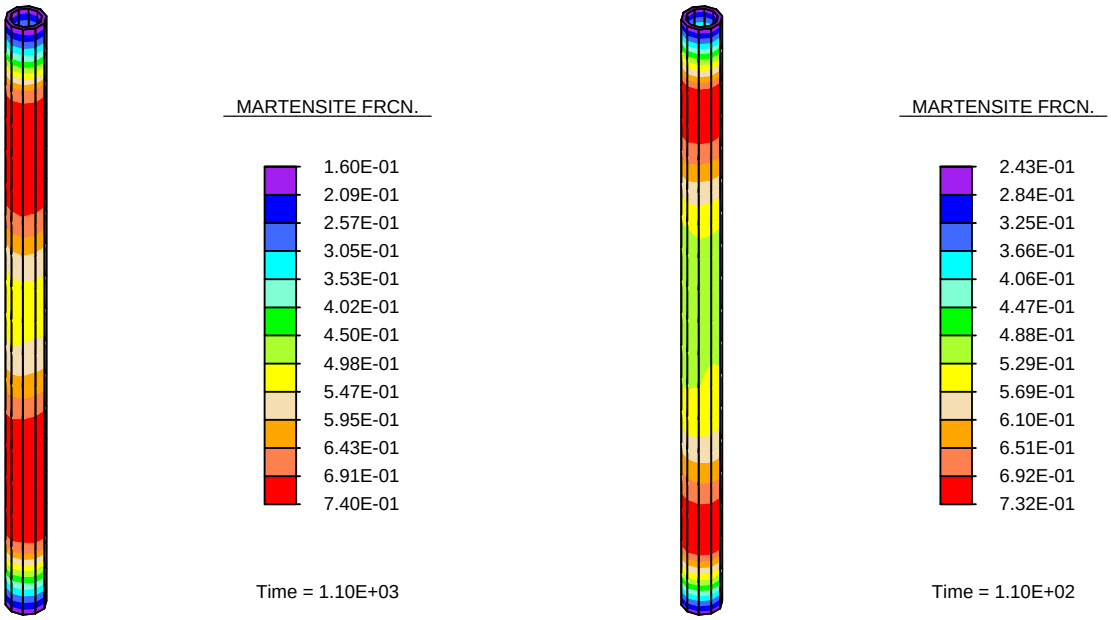

Figure 8.33: *Martensite volume fractions for* $10^{-4}/sec$ *and* $10^{-3}/sec$ *strain rates*

8.4.3 Sheet-textured vs. random-textured tube response under bending

The simulations presented in this section compare bending response for two types of tubes: one with all crystals aligned according to sheet-texture discussed in Section 8.1, and another in which the RVE comprises 4^3 crystals with random orientations and subjected to displacement boundary condition. The tube has an inner diameter of 3.47 *mm* and thickness of 0.45 *mm* as in Section 8.4, but its length is 25.4 *mm* in this case. One end of the tube is fixed, while the other end is subjected to lateral displacement of 10 *mm* in 30 *secs*. The goal of these simulations is to highlight the differences between single-crystal and polycrystal response, which are obtained through single-scale and multiscale modeling, respectively, for a case of non-uniform loading. The material parameters are taken to be the same as in Section 8.4.2 for both the models and adiabatic conditions are applied. The stress response for the two simulations is compared in Figure 8.34, where the average shear stresses at the end are plotted against the lateral displacement. The longitudinal stresses at maximum loading are compared in Figure 8.36, wherein it is observed that the asymmetry in tension and compression regions is more pronounced for the sheet-texture response. However, the temperature history at the end of the tube Figure 8.35 suggests that the temperature changes are quite close in the two cases.

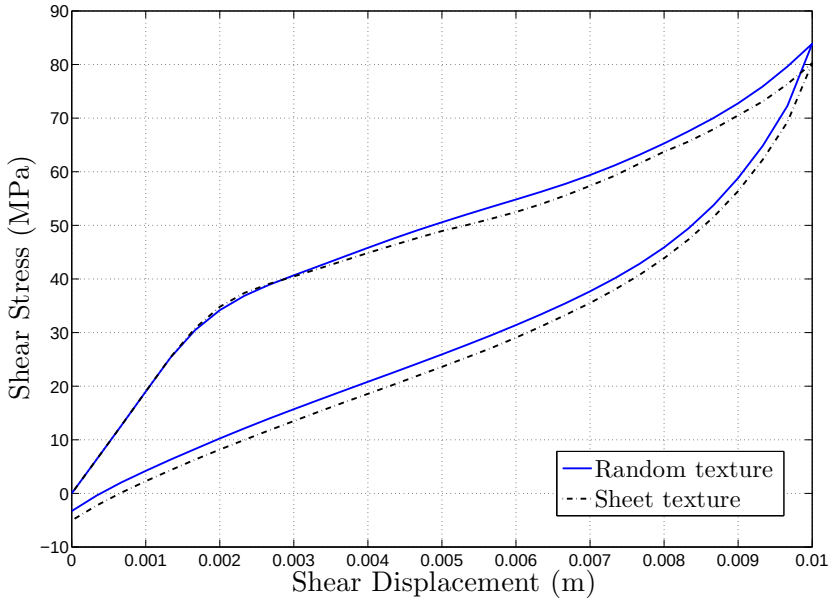

Figure 8.34: *Comparison of stress responses for tube under bending*

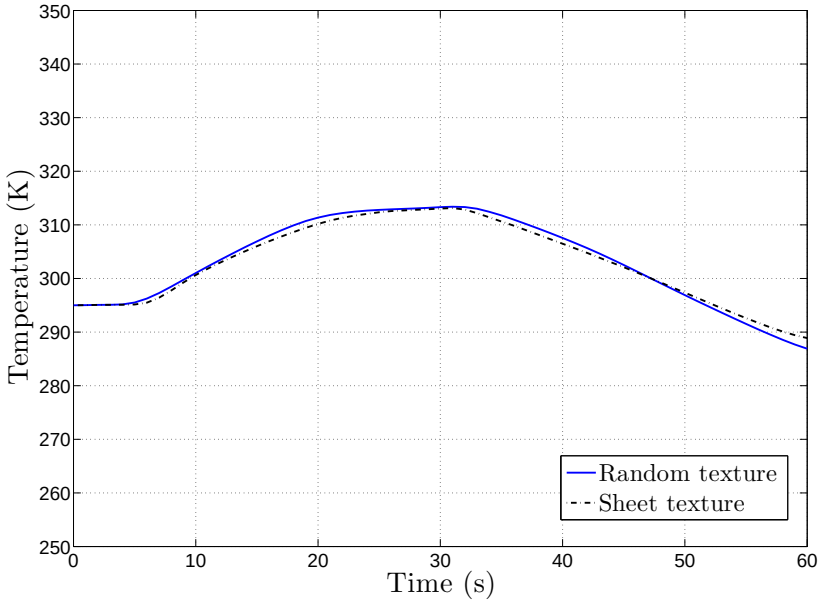

Figure 8.35: *Comparison of temperature histories near fixed end of tube under bending*

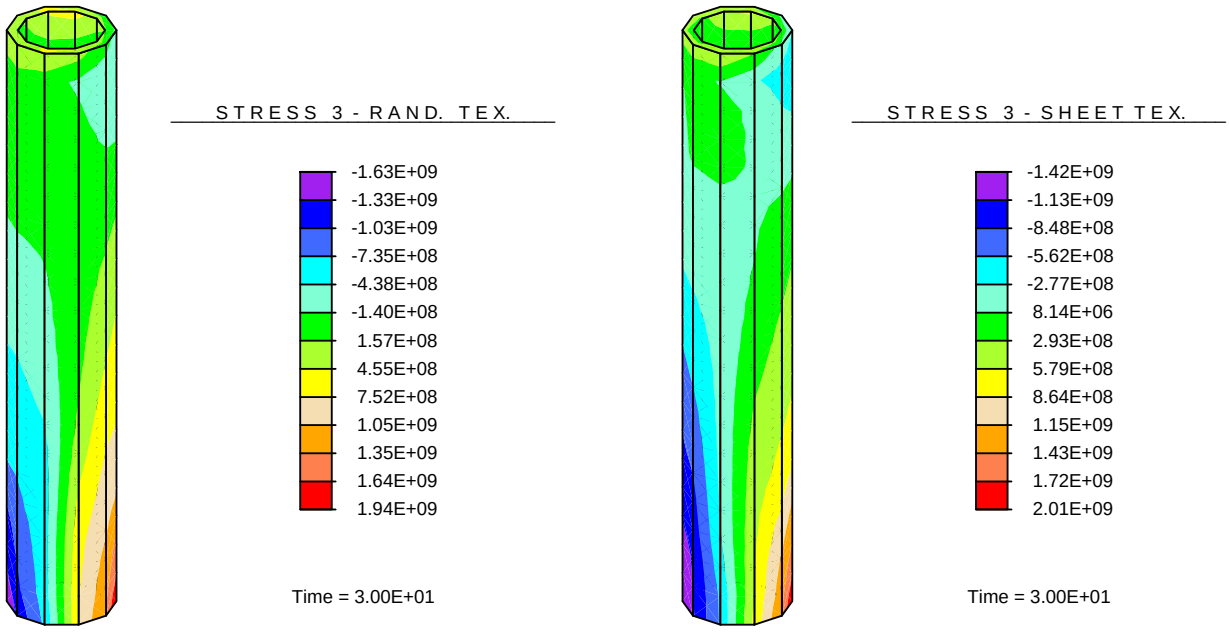

Figure 8.36: *Longitudinal stress distributions for tube with random texture and sheet-texture under bending*

Chapter 9

Conclusions

This dissertation proposes several approaches for modeling the superelastic behavior of Nitinol in both monocrystalline and polycrystalline state. In Chapter 3, the phenomenon of phase transformation is explained and a method of quantifying the continuum transformation deformation through habit-plane calculations is elaborated. The transformation deformation gradients of the habit-plane variants are subsequently homogenized to obtain the mesoscale transformation deformation gradient. A new thermomechanical model is proposed for phase transformation in crystal grains and is compared with other models in Chapter 4. This model is developed in a finite deformation setting and can quantify temperature changes due to dynamic mechanical loading of Nitinol specimens. The response under quasistatic mechanical loading can be easily obtained by restricting the model to isothermal conditions. Also, an earlier model for isothermal conditions is extended to obtain the quasistatic response of Nitinol polycrystals in the presence of R-phase in Chapter 5. The extension involves an incremental solution of the transformation equations, in order to obtain the state of R-phase-martensite transformation.

A multiscale approach is also developed to obtain the macroscopic response of polycrystalline Nitinol in Chapter 7. It is based on solving boundary-value problems at the fine-scale on a suitably chosen polycrystalline RVE and homogenizing its behavior. Finite elements are used to discretize the problem at both scales. The RVE is subjected to different boundary conditions, and it is shown that the solution with periodic boundary condition captures the overall response best, in terms of the superelastic response of Nitinol. This two-scale finite element, or the FE^2 approach, is then extended to obtain the thermomechanically coupled response of Nitinol. A general approach for solving the problem monolithically, for displacement and temperature unknowns, at both scales is presented. It is believed that this framework can be readily extended to other multi-physics problems where the mechanical and other physical quantities are strongly coupled. The resulting algorithm is used to obtain the superelastic of polycrystalline Nitinol subjected to different loading conditions at different strain-rates. Several representative numerical simulations presented in Chapter 8 demonstrate that this approach does well in capturing Nitinol's behavior, when subjected to

various test conditions.

In the future, more emphasis will be afforded to the precise characterization of the microstructure. Even though the results from the multiscale approach correlated well with the experiments, features such as an apparent hardening in the simulated response compared to experiments, need to be investigated further. A probable cause for this apparent hardening is that in the microscale RVE mesh, a single finite element was used to represent a crystal grain, and the orientations of neighboring crystals were not correlated as usually found in physical texture. This can be investigated further with more detailed modeling of the microscale, where not only the size and shape of grains but also the correlations between neighboring grain orientations are taken into account.

When nucleation of martensite takes place in the austenite lattice, the macroscopic stresses are found to rise during the accommodation process. This has been incorporated in the models phenomenologically so far by choosing a higher value of the critical driving force for martensite variants during nucleation, in contrast to that during propagation. This might be modeled in a better way by considering the surface energy of martensite nuclei in the model. Finally, an extension of the multiscale approach for thermomechanical problems could be attempted towards solving the transient coupled equations in both scales, which would be necessary in shock loading scenarios.

Bibliography

[1] R. Abeyaratne and J.K. Knowles. *Evolution of Phase Transitions - A Continuum Theory*. Cambridge University Press, New York, 2006.

[2] R. Abeyaratne and S. Vedantam. A lattice-based model of the kinetics of twin boundary motion. *J. Mech. Phys. Solids*, 51:1675–1700, 2003.

[3] L. Anand and M.E. Gurtin. Thermal effects in the superelasticity of crystalline shape-memory materials. *J. Mech. Phys. Solids*, 51:1015–1058, 2003.

[4] R.J. Asaro. Micromechanics of crystals and polycrystals. *Adv. Appl. Mech.*, 23:1–115, 1983.

[5] J.L. Auriault. Effective macroscopic description for heat conduction in periodic composites. *Int. J. Heat Mass Trans.*, 26(6):861–869, 1983.

[6] F. Auricchio, R.L. Taylor, and J. Lubliner. Shape-memory alloys: Macromodeling and numerical simulations of the superelastic behavior. *Comp. Meth. Appl. Mech. Engg.*, 146:281, 1997.

[7] J.M. Ball and R.D. James. Fine phase mixtures as minimizers of energy. *Arch. Rat. Mech. Anal.*, 100:13–52, 1987.

[8] K.J. Bathe, E. Ramm, and E.L. Wilson. Finite element formulations for large deformation dynamic analysis. *Int. J. Num. Meth. Engg.*, 9:353–386, 1975.

[9] K. Bhattacharya. Self-accommodation in martensite. *Arch. Rat. Mech. Anal.*, 120:201–244, 1992.

[10] K. Bhattacharya. *Microstructure of Martensite*. Oxford University Press, Oxford, 2003.

[11] J. Bonet and P. Bhargava. A uniform deformation gradient hexahedron element with artificial hourglass control. *Int. J. Num. Meth. Engg.*, 48:2809–2828, 1995.

[12] J.G. Boyd and D.C. Lagoudas. A thermodynamical constitutive model for shape memory materials. I. The monolithic shape memory alloy. *Int. J. Plast.*, 12:805–842, 1996.

[13] J. Burke. *The Kinetics of Phase Transformations in Metals*. Pergamon Press, London, 1965.

[14] J. Casey. On elastic-thermo-plastic materials at finite deformations. *Int. J. Plast.*, 14:173–191, 1998.

[15] J. Casey and P.M. Naghdi. A prescription for the identification of finite plastic strain. *Int. J. Engg. Sci.*, 30:1257–1278, 1992.

[16] D. Christ and S. Reese. A finite element model for shape memory alloys considering thermomechanical couplings at large strains. *Int. J. Solids Struct.*, 46:3694–3709, 2009.

[17] W.J. Drugan and J.R. Willis. A micromechanics-based nonlocal constitutive equations and estimates of the representative volume element size for elastic composites. *J. Mech. Phys. Solids*, 44:497–524, 1996.

[18] T.W. Duerig. Some unsolved aspects of Nitinol. *Mater. Sci. Engg. A*, 438-440:69–74, 2006.

[19] D. Entemeyer, E. Patoor, E. Eberhardt, and A. Berveiller. Strain rate sensitivity in superelasticity. *Int. J. Plast.*, 16:1269–1288, 2000.

[20] J.L. Ericksen. The Cauchy and Born hypothesis for crystals. In M.E. Gurtin, editor, *Phase Transformations and Material Instabilities in Solids*, pages 61–78. Academic Press, 1984.

[21] J.L. Ericksen. On the Cauchy-Born rule. *Math. Mech. Solids*, 13:199–220, 2008.

[22] J. D. Eshelby. The determination of the field of an ellipsoidal inclusion and related problems. *Proc. Royal Soc. Lond. A*, 241:376–396, 1957.

[23] F. Feyel and J.L. Chaboche. FE^2 multiscale approach for modelling the elastoviscoplastic behaviour of long fiber SiC/Ti composite materials. *Comp. Meth. Appl. Mech. Engg.*, 183:309–330, 2000.

[24] J. Fish and R. Fan. Mathematical homogenization of nonperiodic heterogeneous media subjected to large deformation transient loading. *Int. J. Num. Meth. Engg.*, 76:1044–1064, 2008.

[25] K. Gall and H. Sehitoglu. The role of texture in tension-compression asymmetry in polycrystalline NiTi. *Int. J. Plast.*, 15:69–92, 1999.

[26] K. Gall, H. Sehitoglu, Y.I. Chumlyakov, and I.V. Kireeva. Tension-compression asymmetry of the stress-strain response in aged single crystal and polycrystalline NiTi. *Acta Mater.*, 47(4):1203–1217, 1999.

[27] X. Gao and M. Huang and. L.C. Brinson. A multivariant micromechanical model for smas part 1. crystallographic issues for the single crystal model. *Int. J. Plast.*, 16:1345–1369, 2000.

[28] I.M. Gitman, H. Askes, and L.J. Sluys. Representative volume: Existence and size determination. *Engg. Fract. Mech.*, 74:2518–2534, 2007.

[29] S. Govindjee and G.J. Hall. A computational model for shape memory alloys. *Int. J. Solids. Struct.*, 37:735–760, 2000.

[30] S. Govindjee and C. Miehe. A multi-variant martensitic phase transformation model: Formulation and numerical implementation. *Comp. Meth. Appl. Mech. Engg.*, 191:215–238, 2001.

[31] C. Grabe and O.T. Bruhns. On the viscous and strain rate dependent behavior of polycrystalline NiTi. *Int. J. Solids Struct.*, 45:18761895, 2008.

[32] A.E. Green and P.M. Naghdi. Some remarks on elastic-plastic deformation at finite strain. *Int. J. Engg. Sci.*, 9:1219–1229, 1971.

[33] K.F. Hane and T.W. Shield. Microstructure in the cubic to monoclinic transition in titanium-nickel shape memory alloys. *Acta Mater.*, 47:2603–2617, 1999.

[34] K.F. Hane and T.W. Shield. Microstructure in the cubic to trigonal transition. *Mater. Sci. Engg. A*, A291:147–159, 2000.

[35] D. Helm and P. Haupt. Shape memory behaviour: modelling within continuum thermomechanics. *Int. J. Solids Struct.*, 40:827–849, 2003.

[36] F.E. Hildebrand and R. Abeyaratne. An atomistic investigation of the kinetics of detwinning. *J. Mech. Phys. Solids*, 56:1296–1319, 2008.

[37] R. Hill. Elastic properties of reinforced solids: Some theoretical principles. *J. Mech. Phys. Solids*, 11:357–372, 1963.

[38] R. Hill. A self-consistent mechanics of composite materials. *J. Mech. Phys. Solids*, 13:213–222, 1965.

[39] R. Hill and J.F.W. Bishop. A theory of the plastic distortion of a polycrystalline aggregate under combined stresses. *Phil. Mag.*, 42:414–427, 1951.

[40] J.P. Holman. *Heat Transfer*. McGraw-Hill, Inc., New York, 1990.

[41] M.S. Huang, X. Gao, and L.C. Brinson. A multivariant micromechanical model for SMAs: Part 2: Polycrystal model. *Int. J. Plast.*, 16:1371–1399, 2000.

[42] T.J.R. Hughes. *The Finite Element Method: Linear Static and Dynamic Finite Element Analysis*. Dover, New York, 2000.

[43] Y. Jung, P. Papadopoulos, and R.O. Ritchie. Constitutive modelling and numerical simulation of multivariant phase transformation in superelastic shape-memory alloys. *Intl. J. Num. Meth. Engg.*, 60:429–460, 2004.

[44] K. Terada K, M. Hori, T. Kyoya, and N. Kikuchi. Simulation of the multi-scale convergence in computational homogenization approach. *Int. J. Solids Struct.*, 37:2285–2311, 2000.

[45] T. Kanit, S. Forest, I. Galliet, V. Mounoury, and D. Jeulin. Determination of the size of the representative volume element for random composites: Statistical and numerical approach. *Int. J. Solids Struct.*, 40:3647–3679, 2003.

[46] U.F. Kocks, C.N. Tome, and H.R. Wenk. *Texture and Anisotropy: Preferred Orientations in Polycrystals and their Effect on Materials Properties*. Cambridge University Press, Cambridge, 1998.

[47] V.G. Kouznetsova. *Computational homogenization for the multi-scale analysis of multi-phase materials*. PhD thesis, Netherlands Institute of Metals Research, 2002.

[48] E. Kröner. Allgemeine Kontinuumstheorie der Versetzungen und Eigenspannungen. *Arch. Rat. Mech. Anal.*, 4:273–334, 1960.

[49] A. Kueck and A. Pelton, 2010. Personal communication.

[50] D. C. Lagoudas, P. B. Entchev, P. Popov, E. Patoor, L. C. Brinson, and X. Gao. Shape memory alloys, part ii: Modeling of polycrystals. *Mech. Mater.*, 38:430–462, 2006.

[51] E. H. Lee and D. T. Liu. Finite-strain elastic-plastic theory with application to plane wave analysis. *J. Appl. Phys.*, 38(1):19–27, 1967.

[52] E.H. Lee. Elastic-plastic deformation at finite strains. *J. Appl. Mech.*, 36:1–6, 1969.

[53] C. Lexcellent, B. Raniecki, and K. Tanaka. Thermodynamic models of pseudoelastic behavior of shape memory alloys. *Arch. Mech.*, 44:261–284, 1992.

[54] C. Liang and C.A. Rogers. A multi-dimensional constitutive model for shape memory alloys. *J. Engr. Math.*, 26:429–443, 1992.

[55] J. Lubliner. *Plasticity Theory*. Macmillan Publishing Co., New York, 1990.

[56] J. Mandel. *Plasticité Classique et Viscoplasticité (CISM, Udine, 1971)*. Springer-Verlag, New York, 1972.

[57] J. Mandel. Thermodynamics and plasticity. In *Foundations of Continuum Thermodynamics*, pages 283–304. Macmillan, 1973.

[58] O. Matsumoto, S. Miyazaki, K. Otsuka, and H. Tamura. Crystallography of martensitic transformation in Ti-Ni single crystals. *Acta Metall.*, 35(8):2137–2144, 1987.

[59] A.L. McKelvey and R.O. Ritchie. Fatigue-crack propagation in Nitinol, a shape-memory and superelastic endovascular stent material. *J. Biomed. Mater. Res.*, 47:301–308, 1999.

[60] J.M. McNaney, V. Imbeni, Y. Jung, P. Papadopoulos, and R.O. Ritchie. An experimental study of the superelastic effect in a shape-memory Nitinol alloy under biaxial loading. *Mech. Mater.*, 35:969–986, 2003.

[61] C. Miehe, J. Schotte, and M. Lambrecht. Homogenization of inelastic solid materials at finite strains based on incremental minimization principles. Application to the texture analysis of polycrystals. *J. Mech. Phys. Solids*, 50:2123–2167, 2002.

[62] S. Miyazaki, S. Kimura, and S. Otsuka. Shape-memory effect and pseudoelasticity associated with the R-phase transition in Ti-50.5 at.% Ni single crystals. *Phil. Mag. A*, 57(3):467–478, 1988.

[63] S. Miyazaki and K. Otsuka. Deformation and transition behavior associated with the R-phase in Ti-Ni alloys. *Metall. Trans. A*, 17A:53–63, 1986.

[64] S. Miyazaki and C.M. Wayman. The R-phase transition and associated shape memory mechanism in Ti-Ni single crystals. *Acta Metall.*, 36(1):181–192, 1988.

[65] N.B. Morgan. Medical shape memory alloy applications - the market and its products. *Mater. Sci. Engg. A*, 378:16–23, 2004.

[66] P.M. Naghdi. A critical review of the state of finite plasticity. *J. Appl. Math. Phys. (ZAMP)*, 41:316–394, 1990.

[67] S. Nemat-Nasser, J.Y. Choi, W.G. Guo, J.B. Isaacs, and M. Taya. High strain-rate, small strain response of a NiTi shape-memory alloy. *J. Engg. Mater. Tech.*, 127:83–89, 2005.

[68] M. Ortiz and E.A. Repetto. Nonconvex energy minimization and dislocation structures in ductile single crystals. *J. Mech. Phys. Solids*, 47:397–462, 1999.

[69] M. Ostoja-Starzewski. Towards stochastic continuum thermodynamics. *J. Non-Equil. Therm.*, 27:335–348, 2002.

[70] K. Otsuka and X. Ren. Physical metallurgy of Ti-Ni-based shape memory alloys. *Prog. Mater. Sci.*, 50:511–678, 2005.

[71] I. Özdemir and W.A.M. Brekelman and. M.G.D. Geers. Computational homogenization for heat conduction in heterogeneous solids. *Int. J. Num. Meth. Engg.*, 73:185–204, 2008.

[72] I. Özdemir and W.A.M. Brekelman and. M.G.D. Geers. FE^2 computational homogenization for the thermo-mechanical analysis of heterogeneous solids. *Comp. Meth. Appl. Mech. Engg.*, 198:602–613, 2008.

[73] E. Patoor, D.C. Lagoudas, P.B. Entchev, L.C. Brinson, and X. Gao. Shape memory alloys, Part I: General properties and modeling of single crystals. *Mech. Mater.*, 38:391–429, 2006.

[74] J.A. Rice. *Mathematical Statistics and Data Analysis*. Duxbury Press, Belmont, 1995.

[75] R.S. Rivlin. Comments on some recent researches in thermodynamics. *Recent Adv. in Engg. Sci.*, 48:1, 1973.

[76] B.W. Rosen and Z. Hashin. Effective thermal expansion coefficients and specific heats of composite materials. *Int. J. Engg. Sci.*, 8:157–173, 1970.

[77] A. Sengupta and P. Papadopoulos. Constitutive modeling and finite element approximation of B2-R-B19′ phase transformations in Nitinol polycrystals. *Comp. Meth. Appl. Mech. Engg.*, 198:3214–3227, 2009.

[78] A. Sengupta and P. Papadopoulos. A note on the use of multiplicative decomposition for displacive phase transformations. *Submitted to Int. J. Engg. Sci.*, 2010.

[79] A. Sengupta, P. Papadopoulos, and R.L. Taylor. Multiscale finite element modeling of superelasticity in Nitinol polycrystals. *Comp. Mech.*, 43:573–584, 2009.

[80] D. Shindo, Y. Murakami, and T. Ohba. Understanding precursor phenomena for the R-phase transformation in Ti-Ni-Based alloys. *MRS Bull.*, 27(2):121–127, 2002.

[81] Y.C. Shu and K. Bhattacharya. The influence of texture on the shape-memory effect in polycrystals. *Acta Mater.*, 46:5457–5473, 1998.

[82] N. Siredey, E. Patoor, M. Berveiller, and A. Eberhardt. Constitutive equations for polycrystalline thermoelastic shape memory alloys. Part I. Intragranular interactions and behavior of the grain. *Int. J. Solids Struct.*, 36:4289–4315, 1999.

[83] P. Sittner, M. Landa, P. Lukas, and V. Novak. R-phase transformation phenomena in thermomechanically loaded NiTi polycrystals. *Mech. Mater.*, 38:475–492, 2006.

[84] P. Sittner, V. Novak, P. Lukas, and M. Landa. Stress-strain-temperature behaviour due to B2-R-B19' transformation in NiTi polycrystals. *J. Engg. Mater. Tech.*, 128:268–278, 2006.

[85] E. Stein and G. Sagar. Theory and finite element computation of cyclic martensitic phase transformation at finite strain. *Int. J. Num. Meth. Engg.*, 74:1–31, 2008.

[86] Q.P. Sun and K.C. Hwang. Micromechanics modelling for the constitutive behavior of polycrystalline shape memory alloys. I. Derivation of general relations. *J. Mech. Phys. Solids*, 41:1–17, 1993.

[87] R.L. Taylor. *FEAP - A Finite Element Analysis Program: Users Manual*. University of California, Berkeley, 2008. http://www.ce.berkeley.edu/rlt.

[88] K. Terada, M. Kurumatani, T. Ushida, and N. Kikuchi. A method of two-scale thermo-mechanical analysis for porous solids with micro-scale heat transfer. *Comp. Mech.*, 46(2):269–285, 2010.

[89] P. Thamburaja. Constitutive equations for martensitic reorientation and detwinning of shape memory alloys. *J. Mech. Phys. Solids*, 53:825–856, 2005.

[90] P. Thamburaja and L. Anand. Polycrystalline shape-memory materials: Effect of crystallographic texture. *J. Mech. Phys. Solids*, 49:709–737, 2001.

[91] S. Turtletaub and A.S.J. Suiker. A multiscale thermomechanical model for cubic to tetragonal martensitic phase transformations. *Int. J. Sol. Struct.*, 43:4509–4545, 2006.

[92] H.-R. Wenk, S. Matthies, J. Donovan, and D. Chateigner. BEARTEX : A Windows-based program system for quantitative texture analysis. *J. Appl. Cryst.*, 31:262–269, 1998.

[93] H.W. Zhang, S. Zhang, J.Y. Biyi, and B.A. Schrefler. Thermo-mechanical analysis of periodic multiphase materials by a multiscale asymptotic homogenization approach. *Int. J. Num. Meth. Engg.*, 69:87–113, 2007.

[94] X. Zhang and H. Sehitoglu. Crystallography of the B2-R-B19' phase transformations in NiTi. *Mater. Sci. Engg. A*, 374:292–302, 2004.

Appendix A

Derivations and algorithms for phase transformation models

A.1 Derivation of thermodynamic driving force and its differential for phase transformation model

The free energy for the phase transformation model adopted in this work is given in (4.29). It follows that

$$f_\alpha \;=\; -\frac{\partial \hat{\Psi}}{\partial \xi_\alpha} = -\left[\mathbb{C}\left(\mathbf{E}^e - \mathbf{A}(\theta-\theta_0)\right)\cdot\frac{\partial \mathbf{E}^e}{\partial \xi_\alpha}\right] - B(\theta-\theta_T) = -\mathbf{S}^e\cdot\frac{\partial \mathbf{E}^e}{\partial \xi_\alpha} - B(\theta-\theta_T)\;. \tag{A.1}$$

Now, using (4.6) one has

$$\frac{\partial \mathbf{E}^e}{\partial \xi_\alpha} = \left[\mathbf{F}^{t-T}\mathbf{C}\frac{\partial \mathbf{F}^{t-1}}{\partial \xi_\alpha}\right]^s = \mathbf{G}_\alpha\;. \tag{A.2}$$

Using the definition of the transformation deformation gradient in (4.4), one arrives at

$$\frac{\partial \mathbf{F}^{t-1}}{\partial \xi_\alpha} = -\mathbf{F}^{t-1}\mathbf{H}^t_\alpha\mathbf{F}^{t-1}\;, \tag{A.3}$$

which leads to

$$\frac{\partial \mathbf{E}^e}{\partial \xi_\alpha} = -\left[\mathbf{F}^{t-T}\mathbf{C}\mathbf{F}^{t-1}\mathbf{H}^t_\alpha\mathbf{F}^{t-1}\right]^s = -\left[\mathbf{C}^e\mathbf{H}^t_\alpha\mathbf{F}^{t-1}\right]^s\;. \tag{A.4}$$

Substituting (A.4) in (A.1) leads to an expression for the thermodynamic force as

$$f_\alpha = \mathbf{S}^e\cdot\left[\mathbf{C}^e\mathbf{H}^t_\alpha\mathbf{F}^{t-1}\right]^s - B(\theta-\theta_T) = (\mathbf{C}^e\mathbf{S}^e)\cdot\left(\mathbf{H}^t_\alpha\mathbf{F}^{t-1}\right) - B(\theta-\theta_T)\;. \tag{A.5}$$

To solve the transformation equations (4.47) incrementally for the potential active variants $\alpha \in \mathcal{PA}$, these equations need to be linearized with respect to the corresponding volume

fractions. This, in turn, requires the linearization of the thermodynamic force in (A.5). The differential of this force can be written as

$$\Delta f_\alpha = -\sum_{\beta\in\mathcal{PA}}\Big[\big(\mathbf{C}^e\mathbb{C}\mathbf{G}_\beta\big)\cdot\Big(\mathbf{H}^t_\alpha\mathbf{F}^{t-1}\Big)+2\big(\mathbf{G}_\beta\mathbf{S}^e\big)\cdot\Big(\mathbf{H}^t_\alpha\mathbf{F}^{t-1}\Big)+ \big(\mathbf{C}^e\mathbf{S}^e\big)\cdot\Big(\mathbf{H}^t_\alpha\mathbf{F}^{t-1}\mathbf{H}^t_\beta\mathbf{F}^{t-1}\Big)\Big]\Delta\xi_\beta\ , \quad \text{(A.6)}$$

where (A.3) and (A.4) are used. Hence the transformation equations can be written as

$$\sum_{\beta\in\mathcal{PA}} A_{\alpha\beta}(\Delta\xi_\beta) = b_\alpha \qquad , \qquad \alpha\in\mathcal{PA}\ , \quad \text{(A.7)}$$

where

$$A_{\alpha\beta} \;=\; \big(\mathbf{C}^e\mathbb{C}\mathbf{G}_\beta\big)\cdot\Big(\mathbf{H}^t_\alpha\mathbf{F}^{t-1}\Big)+2\big(\mathbf{G}_\beta\mathbf{S}^e\big)\cdot\Big(\mathbf{H}^t_\alpha\mathbf{F}^{t-1}\Big)+ \big(\mathbf{C}^e\mathbf{S}^e\big)\cdot\Big(\mathbf{H}^t_\alpha\mathbf{F}^{t-1}\mathbf{H}^t_\beta\mathbf{F}^{t-1}\Big)\ , \quad \text{(A.8)}$$

and

$$\begin{aligned} b_\alpha &= f_\alpha - \mathcal{F}_c \qquad \text{(forward)} \\ b_\alpha &= f_\alpha + \mathcal{F}_c \qquad \text{(reverse)}\ . \end{aligned} \quad \text{(A.9)}$$

A.2 Algorithm for Solution of the Transformation Equations

The algorithm used at each integration point to define the set $\mathcal{PA}$ of active variants and compute the corresponding volume fractions is described below:

1. Data: $\mathbf{E}_{n+1}$, θ_{n+1} and the phase transformation state at t_n
2. Calculate $f^{(0)}_{\alpha,n+1}$ and initialize $\mathcal{PA}$ by checking the condition $\mid f^{(0)}_{\alpha,n+1}\mid \geq F_c$.
3. Initialize $i=1$ and set $\xi^{(0)}_{\alpha,n+1}=\xi_{\alpha,n}, \forall\alpha\in\mathcal{PA}$.
4. Determine $A^{(i-1)}_{\alpha\beta}$ and $b^{(i-1)}_\alpha$ and solve (4.48) for $\Delta\xi^{(i-1)}_{\alpha,n+1}$ and set $\xi^{(i)TR}_{\alpha,n+1}=\xi^{(i-1)}_{\alpha,n+1}+\Delta\xi^{(i-1)}_{\alpha,n+1}$.
5. If $\exists\gamma\in\mathcal{PA}$ for which $f^{(i-1)}_{\gamma,n+1}\Delta\xi^{(i-1)}_{\gamma,n+1}<0$, then

   5a. Remove γ from $\mathcal{PA}$ and go to 4.

6. End if
7. Set $k_1 = k_2 = 1$.
8. If $\sum_{\alpha \in \mathcal{PA}} \xi_{\alpha,n+1}^{(i)\,TR} > 1$, then

   8a. Compute $k_1 = \frac{1 - \sum_{\alpha \in \mathcal{PA}} \xi_{\alpha,n+1}^{(i-1)}}{\sum_{\alpha \in \mathcal{PA}} \Delta\xi_{\alpha,n+1}^{(i-1)}}$.
9. End if
10. Compute $\xi_{min} = \min_{\alpha \in \mathcal{PA}} \left\{0, \xi_{\alpha,n+1}^{(i)\,TR}\right\}$ and $\alpha_{min} = \operatorname{argmin}_{\alpha \in \mathcal{PA}} \left\{0, \xi_{\alpha,n+1}^{(i)\,TR}\right\}$.
11. If $\xi_{min} < 0$, then

    11a. Compute $k_2 = \frac{-\xi_{\alpha,n+1}^{(i-1)}}{\xi_{min} - \xi_{\alpha_{min},n+1}^{(i-1)}}$.
12. End if
13. If $k_1 = k_2 = 1$, then

    13a. Set $\xi_{\alpha,n+1}^{(i)} = \xi_{\alpha,n+1}^{(i)\,TR}$ and exit.
14. Else if $k_1 \leq k_2 \leq 1$, then

    14a. Set $\xi_{\alpha,n+1}^{(i)} = \xi_{\alpha,n+1}^{(i-1)} + k_1 \Delta\xi_{\alpha,n+1}^{(i-1)}$ and exit.
15. Else

    15a. Set $\xi_{\alpha,n+1}^{(i)} = \xi_{\alpha,n+1}^{(i-1)} + k_2 \Delta\xi_{\alpha,n+1}^{(i-1)}$.

    15b. Drop the variant α_{min} from the set $\mathcal{PA}$, set $i = i + 1$, compute $f_{\alpha,n+1}^{(i-1)}$ and go to step 4.
16. End if

Appendix B

Derivation of the rotation matrix based on Euler angles for texture

Three angles are generally necessary to completely describe the texture of a sample, *i.e.*, to determine the orientation of a (cubic) crystal relative to the sample coordinate system. Following the Roe-Matthies convention in Figure 3.6, these angles are defined as follows: The first angle, α, transforms the orthonormal system $\{\mathbf{p}, \mathbf{q}, \mathbf{r}\}$ into $\{\mathbf{p}', \mathbf{q}', \mathbf{r}' = \mathbf{r}\}$. The second angle, β, transforms $\{\mathbf{p}', \mathbf{q}', \mathbf{r}'\}$ into $\{\mathbf{p}'', \mathbf{q}'' = \mathbf{q}', \mathbf{r}''\}$. Finally, the third angle, γ, transforms $\{\mathbf{p}'', \mathbf{q}'', \mathbf{r}''\}$ into $\{\mathbf{p}''', \mathbf{q}''', \mathbf{r}''' = \mathbf{r}''\}$.

Using the classical Euler-Rodrigues formula, the rotation tensor $\mathbf{Q}_1$ which takes $\{\mathbf{p}, \mathbf{q}, \mathbf{r}\}$ into $\{\mathbf{p}', \mathbf{q}', \mathbf{r}' = \mathbf{r}\}$ is given by

$$\mathbf{Q}_1 \;=\; \cos\alpha(\mathbf{p}\otimes\mathbf{p} + \mathbf{q}\otimes\mathbf{q}) - \sin\alpha(\mathbf{p}\otimes\mathbf{q} - \mathbf{q}\otimes\mathbf{p}) + \mathbf{r}\otimes\mathbf{r}\ . \tag{B.1}$$

Similarly, the angle β, which takes $\{\mathbf{p}', \mathbf{q}', \mathbf{r}'\}$ into $\{\mathbf{p}'', \mathbf{q}'' = \mathbf{q}', \mathbf{r}''\}$ corresponds to

$$\mathbf{Q}_2 \;=\; \cos\beta(\mathbf{p}'\otimes\mathbf{p}' + \mathbf{r}'\otimes\mathbf{r}') - \sin\beta(\mathbf{r}'\otimes\mathbf{p}' - \mathbf{p}'\otimes\mathbf{r}') + \mathbf{q}'\otimes\mathbf{q}'\ , \tag{B.2}$$

or, taking into account equations (B.1) and (B.2),

$$\mathbf{Q}_2 \;=\; \mathbf{Q}_1[\mathbf{q}\otimes\mathbf{q} + \cos\beta(\mathbf{p}\otimes\mathbf{p} + \mathbf{r}\otimes\mathbf{r}) - \sin\beta(\mathbf{r}\otimes\mathbf{p} - \mathbf{p}\otimes\mathbf{r})]\mathbf{Q}_1^T\ . \tag{B.3}$$

Likewise the angle γ, which takes $\{\mathbf{p}'', \mathbf{q}'', \mathbf{r}''\}$ into $\{\mathbf{p}''', \mathbf{q}''', \mathbf{r}''' = \mathbf{r}''\}$ can be represented by

$$\mathbf{Q}_3 \;=\; \cos\gamma(\mathbf{p}''\otimes\mathbf{p}'' + \mathbf{q}''\otimes\mathbf{q}'') - \sin\gamma(\mathbf{p}''\otimes\mathbf{q}'' - \mathbf{q}''\otimes\mathbf{p}'') + \mathbf{r}''\otimes\mathbf{r}''\ . \tag{B.4}$$

Using (B.3), it follows that

$$\mathbf{Q}_3 \;=\; \mathbf{Q}_2\mathbf{Q}_1[\mathbf{r}\otimes\mathbf{r} + \cos\gamma(\mathbf{p}\otimes\mathbf{p} + \mathbf{q}\otimes\mathbf{q}) - \sin\gamma(\mathbf{p}\otimes\mathbf{q} - \mathbf{q}\otimes\mathbf{p})]\mathbf{Q}_1^T\mathbf{Q}_2^T\ . \tag{B.5}$$

Combining (B.1), (B.3) and (B.5), one obtains an expression for the total rotation $\mathbf{Q}$ in the form

$$\begin{aligned}\mathbf{Q} &= \mathbf{Q}_3\mathbf{Q}_2\mathbf{Q}_1 \\ &= [\mathbf{r}\otimes\mathbf{r} + \cos\alpha(\mathbf{p}\otimes\mathbf{p} + \mathbf{q}\otimes\mathbf{q}) - \sin\alpha(\mathbf{p}\otimes\mathbf{q} - \mathbf{q}\otimes\mathbf{p})] \\ &\quad [\mathbf{q}\otimes\mathbf{q} + \cos\beta(\mathbf{p}\otimes\mathbf{p} + \mathbf{r}\otimes\mathbf{r}) - \sin\beta(\mathbf{r}\otimes\mathbf{p} - \mathbf{p}\otimes\mathbf{r})] \\ &\quad [\mathbf{r}\otimes\mathbf{r} + \cos\gamma(\mathbf{p}\otimes\mathbf{p} + \mathbf{q}\otimes\mathbf{q}) - \sin\gamma(\mathbf{p}\otimes\mathbf{q} - \mathbf{q}\otimes\mathbf{p})] \ .\end{aligned} \tag{B.6}$$

After a straightforward calculation, the components $[Q_{ij}]$ of the rotation tensor $\mathbf{Q}$ relative to $\{\mathbf{p},\mathbf{q},\mathbf{r}\}$ can be expressed as

$$\begin{aligned}Q_{11} &= \cos\gamma\cos\beta\cos\alpha + \sin\gamma\cos\alpha \ , \\ Q_{12} &= -\sin\gamma\cos\beta\cos\alpha - \cos\gamma\ \sin\alpha \ , \\ Q_{13} &= \sin\beta\cos\alpha \ , \\ Q_{21} &= \cos\gamma\cos\beta\sin\alpha + \sin\gamma\cos\alpha \ , \\ Q_{22} &= -\sin\gamma\cos\beta\sin\alpha + \cos\gamma\cos\alpha \ , \\ Q_{23} &= -\sin\beta\sin\alpha \ , \\ Q_{31} &= -\cos\gamma\sin\beta \ , \\ Q_{32} &= \sin\gamma\sin\beta \ , \\ Q_{33} &= \cos\beta \ .\end{aligned} \tag{B.7}$$

Up to an additional three position-dependent angles may be needed to rotate the fixed global coordinate system to the sample coordinate system at a given point.